

Measurement of elastic properties of silicates at realistic mantle pressures

Dissertation

Zur Erlangung des Grades eines
Doktors der Naturwissenschaften

---Dr. Rer. Nat.---

an der Fakultät für Biologie, Chemie und Geowissenschaften
der Universität Bayreuth

Vorgelegt von

Julien Chantel

Int. M.Sc. (Magmas and Volcanoes)

Aus

Clermont-Ferrand (Frankreich)

2012

Prüfungsausschuß:

Prof. Daniel Frost, Universität Bayreuth

Prof. David Rubie, Universität Bayreuth

Prof. Tomo Katsura, Universität Bayreuth

Prof. Leonid Dubrovinsky, Universität Bayreuth

Prof. Uwe Glatzel, Universität Bayreuth

Acknowledgements

I feel immense pleasure in availing this opportunity for expressing my deepest sense of gratitude and regards to my supervisors, Prof. Daniel Frost and Dr. Wilson Crichton for their continuous support, invaluable suggestions and untiring effort extended during my entire doctoral research work at the Bayerisches Geoinstitut, Universität Bayreuth, Germany, and ESRF, Grenoble, France.

I am acknowledging my obligations to the Marie Curie Research Training Network c2c (Crust to Core); Prof. Daniel Frost with his ERC advanced Grant “DEEP”, and the ESRF for funding my research projects and the administrations of the Bayerisches Geoinstitut and ESRF for providing me necessary facilities to pursue my work.

More so I am indebted to Dr. Geeth Manthilake and Dr. Mainak Mookherjee for their substantial help and invaluable suggestions. I am greatly appreciative of Sven Linhardt, Hubert Schulze, Heinz Fischer and all the technical staff at Bayerisches Geoinstitut and ESRF for their crucial support. I also take this opportunity to express my gratitude to Prof. Hans Keppler for providing me an opportunity to work at BGI. Prof. Robert Liebermann and Dr. Baosheng Li from MPI Stony Brook provided useful training and insights into ultrasonic measurements.

Last but not least I thank my family, friends and all who directly or indirectly sympathized with me in completing my entire dissertation.

Sincerely,

Julien Chantel

Bayreuth, October 2012

Abstract

Measurements of seismic wave travel times through the Earth's interior provide one of the few sources of information on the properties of deep mantle rocks. These travel times can be interpreted in terms of their implications for the mineralogy, chemistry and temperature of the mantle if they can be compared with models determined from laboratory measurements for the elastic properties of mantle minerals at high pressures and temperatures. In this study MHz ultrasonic measurements have been used to determine the velocities of P and S acoustic waves in mantle minerals at mantle conditions. These results are used to constrain the properties of the mantle through comparison with seismic data.

Subduction zones exhibit faster seismic wave velocities compared to the surrounding mantle due to the recycling of relatively cold oceanic lithosphere. In certain subduction zones, however, a 5-10 km thick low velocity layer (LVL) has been inferred to exist along the top surface of the subducting slab at depths of up to 250 km. Shear-wave velocities, in particular, within these layers have been estimated as up to 10% slower than in the surrounding mantle. High-pressure ultrasonic interferometric measurements were performed to gain insight into the elastic properties of lawsonite $[\text{CaAl}_2(\text{Si}_2\text{O}_7)(\text{OH})_2 \cdot \text{H}_2\text{O}]$, a hydrous mineral phase stabilized under cold subduction zone conditions. It was found that lawsonite has an unusually low shear modulus at high pressure and its formation in subducted oceanic crust can explain some seismic evidence for LVL at depths exceeding 100 km. To approach estimated LVL velocities requires lawsonite to form in the subducting crust as a result of a fluid influx due to the breakdown of other hydrous minerals such as serpentine. The formation of lawsonite additionally lowers seismic velocities because it forms at the expense of garnet, a mineral with relatively fast seismic velocities. LVL observations may therefore be used to place constraints on the amount of H_2O subducted into the deep mantle.

Chemical heterogeneities in the transition zone are potentially developed through the subduction of basaltic oceanic crust and lithospheric ultramafic mantle. The mineralogy of these lithologies in the transition zone will mainly differ in terms of the proportion and chemistry of garnet. Garnets formed from originally basaltic and ultramafic compositions will

differ in the proportions of Ca, Fe and majoritic component, with the former being richer in all components except majorite. Most models use partial derivatives of elastic properties with respect to composition to determine the elastic properties of complex garnet compositions in the mantle. In this study the effect of chemical variations on seismic wave velocities of garnets up to transition zone conditions have been intensively studied by examining the effects of Ca, Fe and majoritic substitutions on the elasticity of pyrope. In addition, complex multicomponent garnet compositions, expected to form from both subducted basaltic material and typical ultramafic mantle at transition zone conditions, have been studied. The results indicate that elastic properties of multicomponent garnets can be quite reliably interpolated from the end member properties, with an accuracy that is generally within the experimental uncertainties. No evidence was found that large excess properties exist that cause non-linear contributions to multicomponent elastic properties for the mineral garnet. Deviation between the two calculated mantle models, pyrolitic and MORB, is about 3% for both V_P and V_S , with the modelled slab composition being slower. Within the uncertainties of the seismic data therefore a pyrolite mantle composition is quite consistent with velocities at the base of the transition zone. Relatively low temperatures and olivine-rich nature of the stagnant slab support that there would be few grounds to argue that significant accumulation of MORB composition material may occur at the base of the transition zone.

Ultrasonic interferometry measurements in conjunction with in situ X-ray techniques have been used to measure compressional and shear wave velocities and densities of $MgSiO_3$ perovskite (Mg-Pv) and $Mg_{0.95}Fe_{0.04}^{2+}Fe_{0.01}^{3+}SiO_3$ perovskite ((Mg, Fe)-Pv) in the multianvil at pressures up to 25 GPa and temperatures to 1200 K. Data for Mg-Pv are consistent with previous studies and the (Mg, Fe)-Pv sample has almost identical shear properties to Mg-Pv. The adiabatic bulk modulus, K_S , for (Mg, Fe)-Pv, however, is found to be substantially lower than Mg-Pv, with a refined value of 236 GPa and a pressure derivative of 4.7. It is proposed that this low K_S value results from a change in the elasticity of Fe-bearing perovskite at low pressures <30 GPa.

High temperatures measurements of V_P and V_S of $(Mg_{0.962}Fe_{0.026}^{2+}Fe_{0.014}^{3+})(Al_{0.025}Si_{0.98})O_3$ and $(Mg_{0.94}Fe_{0.037}^{2+}Fe_{0.039}^{3+})(Al_{0.055}Si_{0.954})O_3$ perovskite samples lead to the conclusion that the substitution of Mg by Fe seems to have a consistent effect on K_S , strongly lowering it in both Al and Al-free perovskites while it does not have any noticeable effect on the shear elastic

properties. By substituting Al into the Si octahedral site, the rigidity of this framework is being reduced which clearly has an influence on the shear modulus G . G of the Al-bearing perovskites is obviously controlled by the Al content in the structure. Seismic observations indicate low visibility of underside PP reflections from the 660 km discontinuity. Seismologists have used this in the past to argue that the P velocity contrast at the discontinuity is much lower than would be expected from seismic reference models. The data collected on Fe-Al perovskite in this study provide excellent support for this argument as model calculations based on these data show very little contrast in V_p at 660 km depth. Instead, the model derived in this study indicates that much of the change in P velocity between the transition zone and lower mantle occurs over a much broader depth, 200km, interval and is mainly attributed to the transformation of garnet to perovskite. A major conclusion therefore is that a sharp 660 km discontinuity reflection should be visible in S but not P wave seismic data. The model calculation for V_S is in a good agreement with the seismic reference models up to depths as great as 1071 km, while V_P remains 3 to 4% lower at lower mantle conditions. The extrapolations of pressure and temperature dependences significantly out of the ranges over that they were measured may well explain this discrepancy however.

Zusammenfassung

Das Messen der Ausbreitungsgeschwindigkeit von seismischen Wellen durch das Erdinnere ist eine der wenigen Möglichkeiten Information über Gesteine des unteren Erdmantels zu erhalten. Diese Ausbreitungsgeschwindigkeit hat einen direkten Bezug auf die Mineralogie, Chemismus und Temperatur des Erdmantels und kann mit Modellen, die auf experimentellen Messungen der elastischen Eigenschaften von Mantelmineralien bei hohem Druck und Temperatur beruhen, verglichen werden.

Während dieser Studie wurde mit Hilfe von MHz-Ultraschallmessungen die akustische Ausbreitungsgeschwindigkeit von Primär- (P-) und Sekundär- (S-) Wellen in Mantelmineralien unter Mantelbedingungen untersucht. Die gewonnenen Daten wurden mit seismischen Daten verglichen, um Aussagen über die Eigenschaften des Erdmantels treffen zu können.

Subduktionszonen weisen schnellere Ausbreitungsgeschwindigkeiten seismischer Wellen im Vergleich zum umgebenden Mantel auf. Dies ist auf die Anwesenheit von relativ kalter ozeanischer Kruste zurückzuführen. In bestimmten Subduktionszonen sind 5 – 10 km mächtige *low velocity layer* (LVL) entlang des oberen Teils der subduzierenden Kruste in Tiefen bis zu 250 km zu beobachten. Scherwellengeschwindigkeiten innerhalb dieser LVL sind in etwa 10 % geringer als im umgebenden Mantel. Hochdruck Ultraschallinterferometrie wurde angewendet um Information über elastische Eigenschaften von Lawsonit $[\text{CaAl}_2(\text{Si}_2\text{O}_7)(\text{OH})_2 \cdot \text{H}_2\text{O}]$ zu gewinnen, welches ein wasserführendes Mineral ist, das in den kalten Bereichen von Subduktionszonen stabil ist. Es war möglich nachzuweisen, dass Lawsonit ein ungewöhnlich geringes Schermodul G bei hohen Drücken besitzt und dass die Bildung von Lawsonit eine Erklärung für diese LVL ab Tiefen von 100 km sein kann. Um die angenommenen LVL-Geschwindigkeiten zu beobachten, muss Lawsonit innerhalb der subduzierten Kruste als ein Resultat von Fluiden gebildet werden, die aufgrund des instabil Werdens von anderen hydratisierten Mineralien (z.B. Serpentin) auftreten. Die Bildung von Lawsonit erniedrigt zusätzlich die seismische Geschwindigkeit, weil Lawsonit auf Kosten von Granat entsteht, welcher ein Mineral mit relative hoher seismischer

Wellengeschwindigkeit ist. Die Beobachtung von LVL kann daher Rückschlüsse auf die in den unteren Mantel subduzierende Menge an H_2O geben.

Chemische Heterogenitäten in der Übergangszone (*transition zone*) sind vermutlich auf subduzierte basaltische, ozeanische Kruste und lithosphärischen, ultrabasischen Mantel zurückzuführen. Die Mineralogie in der Übergangszone ist vor Allem vom Gehalt und Chemismus von Granat abhängig. Granat, welcher sich aus basaltischen oder ultramafischen Protolithen gebildet hat, unterscheidet sich im Gehalt von Ca, Fe und der Majoritkomponente, wobei jener mit basaltischem Ursprung reicher an Ca und Fe und ärmer an der Majoritkomponente ist. Die meisten Modelle basieren auf partiellen Ableitungen der elastischen Eigenschaften abhängig vom Chemismus, um die elastischen Eigenschaften von komplexen Granatzusammensetzungen im Mantel zu bestimmen. In dieser Arbeit wurde der Einfluss von verschiedenen chemischen Zusammensetzung auf seismische Wellengeschwindigkeiten von Granat bis zu Bedingungen der Übergangszone untersucht. Hierzu wurde der Einfluss von Ca, Fe und Majoritsubstitution auf die Elastizität von Pyrop beobachtet. Zusätzlich wurden komplexe Granatmischkristalle untersucht, von welchen angenommen wird, dass sie sich sowohl aus basaltischen sowie aus ultramafischen Material unter Bedingungen der Übergangszone bilden können.

Die Ergebnisse lassen annehmen, dass sich die elastischen Eigenschaften von Granatmischkristallen ausgehend von den Eigenschaften der Endglieder interpolieren lassen. Die damit verbundenen Abweichungen liegen innerhalb der Unsicherheiten der Experimente. Des Weiteren konnte kein Anzeichen gefunden werden, dass ein Einfluss der Exzessenergie besteht, welche einen nicht-linearen Einfluss auf die elastischen Eigenschaften von Granatmischkristallen hat. Abweichungen zwischen den beiden berechneten Mantelmodellen, pyrolitisch und MORB, ist ca. 3 % für jeweils V_P und V_S , wobei die Ausbreitungsgeschwindigkeit des Mantel-slabs als langsamer angenommen wurde. Innerhalb der Fehler von seismischen Daten ist eine pyrolitische Mantelzusammensetzung übereinstimmend mit Geschwindigkeiten im unteren Bereich der Übergangszone. Die relativ geringe Temperatur und der hohe Anteil an Olivin des absinkenden slab lässt ein gewisses Argumentationspotential bezüglich einer bedeutenden Akkumulation von Material mit MORB-Zusammensetzung an der Basis der Übergangszone zu.

Ultraschallinferometrie in Verbindung mit in situ Röntgenmethoden wurden bei 25 GPa und 1200 K in einer Multianvilpresse für die Messung von Dichte und Kompressions- und Scherwellengeschwindigkeiten von $MgSiO_3$ Perovskit und $Mg_{0.95}Fe_{0.04}^{2+}Fe_{0.01}^{3+}SiO_3$ Perovskit benutzt. Die Daten für Mg-Pv stimmen mit früheren Studien überein und (Mg, Fe)-Pv hat nahezu identische Schereigenschaften wie Mg-Pv. Allerdings ist das adiabatische Kompressionsmodul, K_s , von (Mg, Fe)-Pv deutlich geringer als von (Mg)-Pv, mit einem verfeinerten Wert von 236 GPa und einer Druckableitung von 4,7. Es wird vorgeschlagen, dass dieser geringe K_s Wert durch eine Veränderung der Elastizität von Fe-haltigem Perovskit bei kleineren Drücken <30 GPa zustande kommt.

Hochtemperaturmessungen von V_p und V_s an $(Mg_{0.962}Fe_{0.026}^{2+}Fe_{0.014}^{3+})(Al_{0.025}Si_{0.98})O_3$ und $(Mg_{0.94}Fe_{0.037}^{2+}Fe_{0.039}^{3+})(Al_{0.055}Si_{0.954})O_3$ Perovskitproben legen den Schluss nahe, dass die Substitution von Mg durch Fe einen systematischen Effekt auf K_s hat, der dadurch sowohl in Al-haltigen als auch in Al-freien Perovskiten stark verringert wird, während kein Effekt auf die Schereigenschaften festzustellen ist. Durch die Substitution von Al auf den Si-Oktaederplatz wird die Steifheit des Gitters verändert, was einen deutlichen Einfluss auf das Schermodul G hat. Wir beobachten, dass das G der Al-haltigen Perovskite offensichtlich durch den Al Gehalt der Struktur kontrolliert wird. Seismische Beobachtungen ergaben eine geringe Sichtbarkeit von unterseitigen PP Reflektionen an der 660 km Diskontinuität. Seismologen argumentieren in der Vergangenheit aufgrund dieser Beobachtung, dass der P-Wellenkontrast der Diskontinuität viel geringer ist als in seismischen Referenzmodellen angenommen wird.

Die im Rahmen dieser Studie an Fe-Al Perovskit gesammelten Daten bieten eine exzellente Unterstützung für dieses Argument, da Modellrechnungen mit den Ergebnissen nur einen sehr geringen V_p Kontrast in 660 km Tiefe ergeben. Stattdessen ergibt das Modell dieser Studie, dass ein großer Teil der Veränderung der P-Wellen Geschwindigkeit zwischen der Übergangszone und dem unteren Mantel über ein breiteres Intervall von 200 km stattfindet und hauptsächlich durch den Übergang von Granat zu Perovskit zustande kommt. Eine Hauptfolgerung ist somit, dass nur in den seismischen S-Wellen Daten eine scharfe 660 km Diskontinuität sichtbar sein sollte und nicht in den Daten der P-Wellen. Die V_s Modellrechnungen stimmen bis zu Tiefen von 1071 km gut mit den seismischen

Referenzmodellen überein, während V_p unter Bedingungen des unteren Mantels 3-4% geringer bleibt. Eine Extrapolation der Druck- und Temperaturabhängigkeiten deutlich außerhalb der Messbedingungen könnte diese Diskrepanz allerdings sehr gut erklären.

Table of Contents

1. Introduction	2
1.1 Aims and objectives.....	2
1.2 Background and motivation	3
1.2.1 Petrologic perspective	3
1.2.2 Geophysical perspective.....	6
1.3 Laboratory measurements of elastic properties	12
2. In situ ultrasonic velocity measurement in multianvil apparatus	16
2.1 Experimental setup	16
2.1.1 Multianvil apparatus.....	16
2.1.2 Assembly.....	18
2.1.3 Fabrication of monomineralic, polycrystalline aggregates for ultrasonic wave propagation measurements at high pressures	21
2.1.4 Pressure calibration	22
2.1.5 Temperature calibration	25
2.1.6 Transducer	26
2.1.7 Synchrotron X-Ray Studies using the Multianvil	27
2.2 Data acquisition and processing.....	30
2.2.1 Phase comparison method	30
2.2.1.1 Principles.....	30
2.2.1.2 Instrumentation.....	31
2.2.2 Pulse echo overlap.....	33
2.2.2.1 Principle.....	33
2.2.2.2 Acquisition of the transfer function.....	34
2.2.2.3 Travel time measurements	36
2.2.3 Length of the sample	37
2.2.3.1 Cook Method.....	37
2.2.3.2 X-ray radiography	38

3. The elasticity of lawsonite at high pressure and the origin of low velocity layers in subduction zones.....	40
3.1 Introduction	40
3.2 Experimental Methods.....	42
3.2.1 Lawsonite synthesis and hot pressing	42
3.2.2 Specimen characterization.....	43
3.2.3 Velocity measurements at high pressure	44
3.3 Results	47
3.4 Discussion	49
3.4.1 High temperature and pressure model.....	49
3.4.2 Low velocity layers and the presence of lawsonite.....	51
4. Sound velocities of garnets with MORB and pyrolite compositions in the transition zone.	58
4.1 Introduction	58
4.2 Experimental procedures	61
4.2.1 Garnets synthesis, hot pressing and characterization	61
4.2.2 Velocity measurements at high pressure	62
4.3 Results	64
4.3.1 Ultrasonic measurements	64
4.3.2 Data fitting.....	68
4.3.3 Refinement of elastic properties for the garnet end members almandine, grossular and majorite.....	69
4.4 Discussion	72
4.4.1 The calculation of elastic properties for multi component garnets from end members	72
4.4.2 A comparison with mantle velocity models.....	73
5. Sound velocities of aluminum-bearing iron-magnesium silicate perovskite of 25 GPa and 1500K	80
5.1 Introduction	80

5.2 Methods	82
5.3 Results and discussion	88
5.3.1 Effect of the Fe substitution	88
5.3.2 Effect of the combined Fe and Al substitutions	98
5.3.2.1 Implications for the velocity jump at the 660 km discontinuity.....	108
5.3.2.2 Implications for the lower mantle.....	115
6. Conclusion and perspectives	120
References	124
Appendix 1	134
Elastic properties of minerals	134
<i>P-V-T</i> equation of state calculations	137
Appendix 2	140
Data collection	140
Data reduction	144
Appendix 3	147
Data collection	147
Data treatment.....	150

1. Introduction

1.1 Aims and objectives

This thesis essentially comprises an experimental study to determine ultrasonic wave velocities and elastic properties of three systems: lawsonite, garnet solid solutions and magnesium silicate perovskite. Lawsonite is proposed to potentially explain the presence, in certain subduction zones, of a 5-10 km thick low velocity layer (LVL) along the top surface of the subducting slab at depths of up to 250 km. The understanding of its elastic properties at the condition prevailing in subduction zones will place constraints on the amount of H₂O subducted into the deep mantle. On the other hand, chemical heterogeneities in the transition zone and the lower mantle are potentially developed through the subduction of basaltic oceanic crust and lithospheric ultramafic mantle. The mineralogy of these lithologies will mainly differ in terms of the proportion and chemistry of garnet in the transition zone and magnesium silicate perovskite in the lower mantle. Reliable velocity measurements of these minerals at high pressures and high temperature will provide constraints to quantify the chemical, thermal, and phase-change effects.

Specifically there are four objectives of this study:

1. To set up a suitable experimental method that allows accurate measurement of physical properties of samples under high pressure and high temperature conditions.
2. To produce high quality specimens those are stable under high pressure and temperature conditions and are suitable for ultrasonic wave propagation experiments.
3. To measure the ultrasonic velocities and estimate elastic properties of lawsonite, garnet solid solutions and magnesium silicate perovskite at variable pressures and temperatures conditions encompassing their stability fields.
4. To evaluate the effect of these phases on the overall seismic velocities of subduction zones, transition zone and lower mantle to answer the question whether their presence or chemical variations might explain the seismic observations.

1.2 Background and motivation

The following sections provide background information on the thermochemical and physical properties of lawsonite, garnet solid solutions and magnesium silicate perovskite from different perspectives to rationalize why these phases are in the focus of this study.

1.2.1 Petrologic perspective

Over the past decades, the development of seismic tomography succeeded in mapping of lateral variability in seismic wave velocities throughout the globe. Slabs are cold when they enter the mantle but they warm up toward ambient temperature; they get warmed up from both sides. The cold portions of the slabs have high seismic velocities, compared with mantle of the same composition because it is denser than the normal mantle (**Figure 1.2.1**). Slabs are composed of oceanic crust, depleted harzburgite and serpentinized peridotite; CO₂ and H₂O occur in the upper part. These fluids lower the melting point and seismic velocities of slabs compared with dry refractory peridotite. After the conversion of basalt to eclogite the melting point is still high. Cold eclogite itself has low shear velocities and high density compared with warm peridotite. Eclogites are the high-pressure forms of basalts. The term “eclogite” refers to rocks mainly composed of omphacite (diopside plus jadeite) and garnet. Eclogites are simply subducted oceanic crust or basaltic melts that have crystallized at high pressure.

The time scale for heating the slab to above the dehydration and melting points is a small fraction of the age of the plate upon subduction since the basalt and volatiles are near the top of the slab. Recycled slabs can be fertile and can have low seismic velocities. Seismic velocity is controlled by composition, mineralogy and volatiles content as well as by temperature. If the melts and volatiles completely leave the slab then it can become a high seismic velocity anomaly.

The material entering subduction zones have a large range of ages, crustal thickness and buoyancies. They therefore equilibrate at different depths. Some slabs penetrate 660 km into the lower mantle and sink slowly (**Figure 1.2.1BB'**) when some

others are deviated at 660 km, recirculate in the transition zone or sink later to lower mantle (**Figure 1.2.1CC'**). The inference that some thick slabs, representing old oceanic plates, break through the 660 km mantle discontinuity does not require that they all do; slabs have a variety of fates. Eclogites comes in a large range of compositions, densities and seismic velocities. These can settle to various levels, depending on composition; the eclogite bodies can sink to greater depths, because of their density, have low-velocity compared to similar-density rocks. Some eclogites have densities intermediate to the low- and high- pressure assemblages at the various peridotite phase boundaries (410 km, 500 km, 660 km); they will be trapped at these boundaries, affecting the seismic properties.

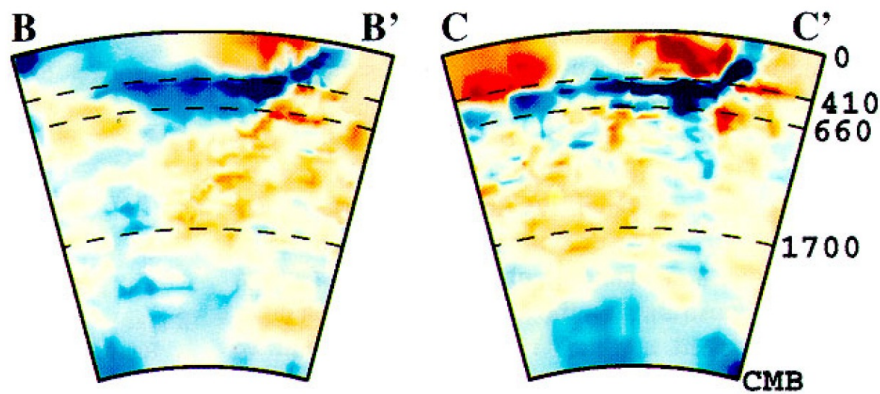


Figure 1.2.1: Slab structure illustrated by vertical mantle sections across (b) southern Kurile, (c) Izu Bonin. From Karason and van der Hilst (2001). In blue are represented the lower seismic velocities and in red the fastest.

Recycled oceanic crust, eclogite, will have a particularly high density when it can sink below about 720 km because the high silica content of MORB gives a large stishovite content to MORB-eclogite. On the other hand, cumulate gabbros, the average composition of the oceanic crust have much lower silica contents and this reduces their high-pressure densities. The densities of peridotites vary from about 3.3 to 3.47 g.cm⁻³ while measured and theoretical eclogite densities range from 3.45 to 3.75 g.cm⁻³. The latter is comparable to the inferred standard temperature and pressure density near 660 km and about 10% less dense than the lower mantle. The lower density eclogites (high-

MgO, low-SiO₂) have densities less than the mantle below 410 km and will therefore be trapped at that boundary, even when cold.

Slabs sink into the mantle because they are cold and dense. Their properties depend on more than the thermal expansion ($\alpha\Delta T$). When phase changes are included, the average density contrast of slabs is about three times greater than would be calculated from thermal expansion alone. There are several phase changes in cold subducting material that contribute to the increase in the relative density of the slab. The basalt-eclogite transition is elevated, contributing a 15% density increase for the basaltic portion of the slab in the upper 50-60 km. The absence of melt in the slab relative to the surrounding asthenosphere increases the density and velocity anomaly of the slab in the upper 300 km of the mantle. If the slab contains volatiles, or low-melting point components, it can be both dense and low-velocity. A CO₂-rich eclogite layer will show up as a low-velocity zone, in spite of being cold. The olivine-spinel and pyroxene-majorite phase changes in cold slabs are elevated by some 100 km above the 410 km discontinuity, contributing about 10% to the density contrast in the slab. The ilmenite form of pyroxene is 5% denser than garnetite, increasing the density contrast of the cold slab between 500 and 670 km, relative to normal mantle, by about a factor of 2 or 3 over that computed from thermal expansion.

The magnitude of horizontal temperature gradients in the mantle are unknown, but in slabs and thermal boundary layers the temperature changes about 800 °C over about 50 km. The upper mantle has a lower viscosity and higher strain rates than the lower mantle. The deformation of heterogeneities in the upper mantle is rapid and results in the formation of small scale (<15 km) heterogeneities. On the other hand, the deformation of the heterogeneities in the lower mantle is slower. In addition, when the slabs penetrate the lower mantle it often fold and results in creating a thicker structure. Model predicts that the upper mantle sampled five times more rapidly the heterogeneities than the lower mantle (Kellogg *et al.*, 1999).

Because the subduction of slabs, which is depleted lithosphere, creates chemical, mineralogical and thermal heterogeneities, it has been proposed to be a perfect candidate to explain the seismic heterogeneities at many scales throughout mantle.

1.2.2 Geophysical perspective

The structure of the Earth's interior is fairly well known from seismology, and knowledge of the fine structure is improving continuously. Seismology not only provides the structure, it also provides information about the composition, crystal structure or mineralogy and physical state. One-dimensional models, such as the Preliminary Earth Model Reference Model (PREM) (Dziewonski and Anderson, 1981) or AK135 (Kennett *et al.*, 1995), have been generated by compiling thousands of seismic records (**Figure 1.2.2**). In these models, the observed variations of seismic waves, V_P and V_S , and densities, reflect radial and lateral variations of chemical composition, mineralogy, pressure, and temperature. In these models, velocities are described by a set of polynomial functions between depths defined by seismic discontinuities.

The propagation characteristics (travel times, reflections amplitudes, dispersion characteristics) of seismic waves of the main elements in Earth's interior, the core, the mantle and the crust, have provided details about the nature of the Earth's interior. The most part Earth's interior is relatively simple, divided into a solid sphere (the inner core) surrounded by roughly uniform shells of liquid iron (the outer core) and rock (mantle and crust). But each of these has subdivisions that are almost as fundamental. Phase changes dominate the radial variations in density and seismic velocity. Some of the isobaric phase changes, their approximate depth extent in "normal" mantle and the density contrasts are as follows:

50-60 km	basalt → eclogite (15%)
50-60 km	spinel peridotite → garnet peridotite (3%)
400-420 km	olivine → wadsleyite (7%)
300-400 km	orthopyroxene → majorite (10%)
500-580 km	wadsleyite + st (4.5%) → ringwoodite + st (1.6%)
400-500 km	clinopyroxene → garnet (10%)
500 km	garnet-majorite s.s. (5%)
700 km	ilmenite → perovskite (5%)

Figure 1.2.2.1 is a plot of V_P , V_S and density as a function of depth into the Earth with the main regions of Earth and important boundaries labeled in **Figure 1.2.2.1**. In several large regions such as the lower mantle, the outer core and the inner core, the velocities smoothly increase with depth. The increase is a result of the effect of pressure on the seismic wave velocities. Although temperature also increases with depth, the pressure increase resulting from the weight of the rocks above has a greater impact and the seismic wave velocities increase smoothly in these regions of uniform composition.

Seismic models of both global and regional nature are used to test petrological models, i.e. potential mineral assemblages, as a function of depth. One can compare the seismic reference models with velocities calculated for mineral assemblages, through use of well-established elastic behavior. The most commonly used petrological model was proposed by Ringwood (1975) and is based on a pyrolitic composition of mantle peridotites and oceanic basalts. However, the seismic reference models are representing the Earth's internal composition, which can be further described by how P and S waves travel in the form of a expression polynomial. A better procedure, proposed by Cammarano *et al.* (2005), consists of fitting the mineral assemblages to seismic data. Assuming a particular bulk composition, Cammarano *et al.* (2005) fitted the seismic data using the elastic properties of the minerals. The obtained velocities and density profile in function of depth are consistent with the pyrolite model for the upper mantle and the transition zone (**Figure 1.2.2.2**).

Pyrolite (pyroxene-olivine-rock) is a hypothetical primitive mantle material that on fractional melting yields a typical basaltic magma and leaves behind a residual refractory dunite-peridotite. It is approximately one part basalt and 3-4 parts dunite. Pyrolite compositions are arbitrary and are based entirely on major elements and on several assumptions regarding allowable amounts of basalt and melting in the source region. They do not satisfy trace element or isotopic data and they violate chondritic abundances and evidence for mantle heterogeneity. On the other hand, mantle compositions based on isotopic constraints alone are equally arbitrary and do not satisfy elementary petrological considerations.

The PREM model is a useful reference for understanding the main features of Earth. More recent efforts have focused on estimating the lateral variations in wave

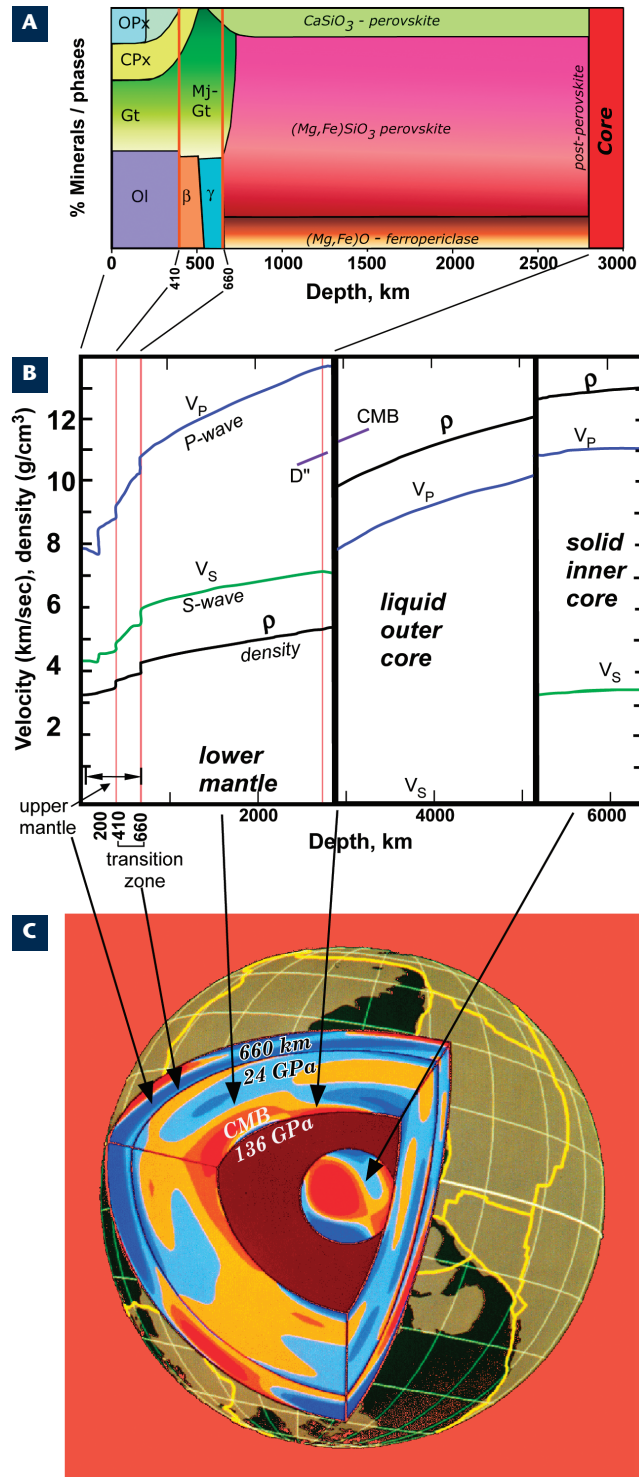


Figure 1.2.2.1: (A) Major phases present in the mantle at all depths, and their approximate proportions. (B) One-dimensional seismic preliminary reference Earth model (PREM) of Dziewonski and Anderson (1981). (C) Interior of the Earth. From Bass and Parise (2008).

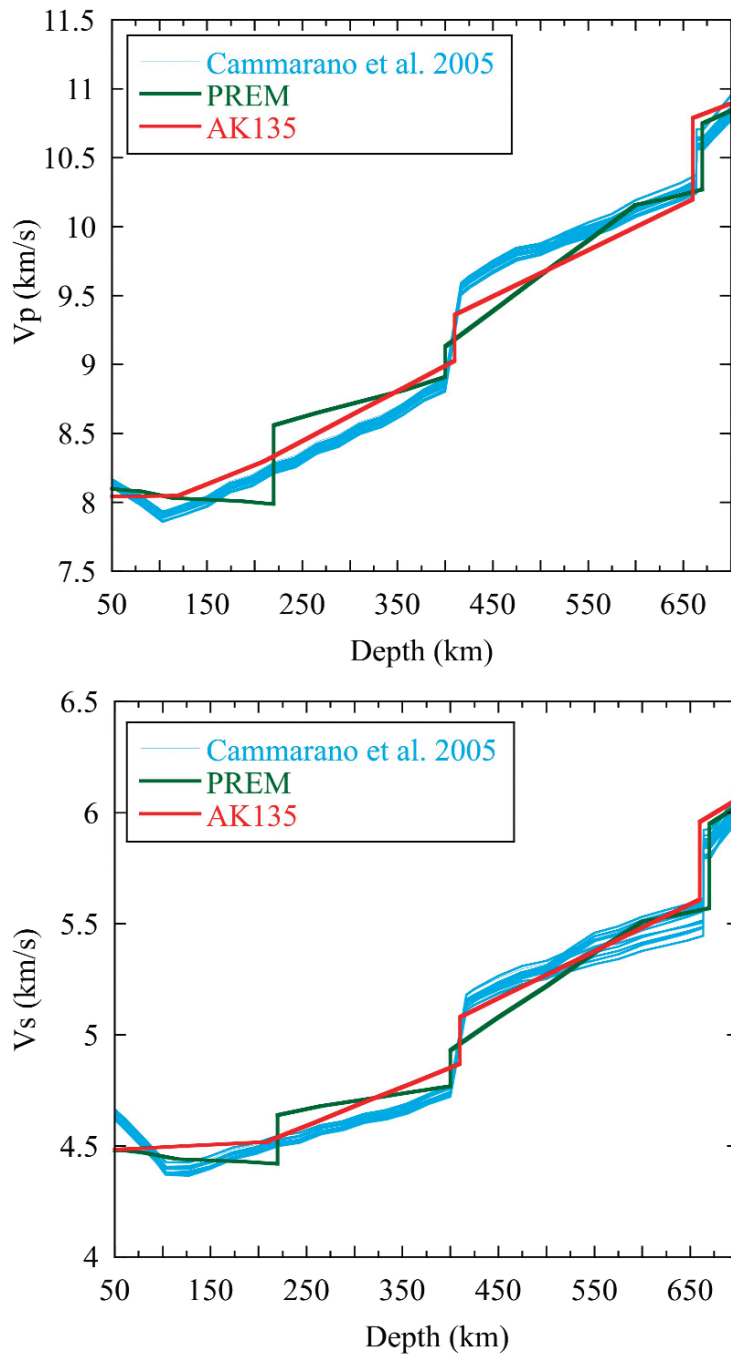


Figure 1.2.2.2: *P- and S- wave velocities in the upper mantle and transition zone from the PREM, AK135 and Cammarano et al. (2005). The various models by Cammarano et al. (2005) were obtained by fitting global seismic data for a pyrolitic mineral assemblage by using different sets of mineral elastic properties.*

velocities within the shells that make up the reference model. These approaches are often based on seismic tomography, which is a way of mapping out the variations in structure using observations from large numbers of seismograms. The basic idea is to use observed delayed (or early) arrival times (delayed with respect to the reference model) to locate regions of relatively fast and relatively slow seismic wave velocities.

It is increasingly clear that the upper mantle is heterogeneous in all parameters at all scales. The parameters include seismic scattering potential, anisotropy, mineralogy, major and trace element chemistry, isotopes, melting point and temperature. There is now evidence for major element, mineralogical, trace element and isotopic heterogeneities, on various scales (grain size to hemispheric) and for lateral variations in temperature and melting point. The large-scale features of the upper mantle are well known from global tomographic studies. The mantle above 200-300 km depth correlates very well with known tectonic features. There are large differences between continents and oceans, and between cratons, tectonic regions, back-arc basins and different age ocean basins. Low-velocity zones occur beneath ridges and tectonic regions at depths less than 200 km. At depth greater than 200 km there are high-velocity anomalies associated with subducting slabs.

It is important to understand the factors that influence lateral heterogeneity in density and seismic velocities. Much of the radial structure of the Earth is due to changes in mineralogy resulting from pressure-induced equilibrium phase changes or changes in composition. The phase fields depend on temperature as well as pressure so that a given mineral assemblage will occur at a different depth in colder parts of the mantle. Variations in temperature, at constant pressure, can cause larger changes in the physical properties than are caused by the effect of temperature alone. There are also some mineral assemblages that do not exist under normal conditions of pressure and temperature but occur only under the extremes of temperature found in cold slabs. Generally the cold assemblages are characterized by high density and high elastic moduli.

The upper mantle scatters seismic energy indicating that it is heterogeneous on the scale of seismic waves, ~10 km. At depth between 800 and 1000 km there is good correlation of seismic velocities with inferred regions of past subduction. It is now well established that seismic heterogeneity exists throughout the whole mantle (**Figures**

1.2.2.3 and 1.2.2.4). That is, the velocities at a given depth are different in different parts of the globe. It was thought at first that these differences in velocity were due to differences in temperature only, by analogy with assumptions about upper-mantle heterogeneity. It was enticing to think of seismically slow material as being hot and buoyant, thus driving mantle flow. However, mineral-physics data have shown that the temperatures required explaining lower mantle seismic heterogeneity may be unreasonably high. It is more likely that this heterogeneity is due to a combination of chemical, thermal, and phase-change effects (Trampert *et al.*, 2004). The quantification of chemical, thermal, and phase-change effects illustrates how the results of laboratory high-pressure experiments are needed to interpret the available seismic information.

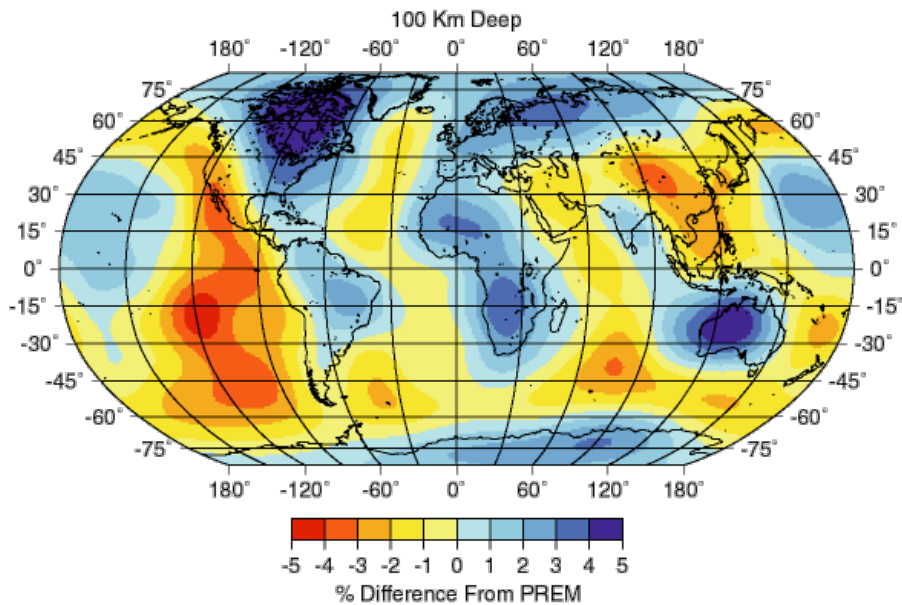


Figure 1.2.2.3: Map of the variations in V_s with respect to the value in PREM at 100 km depth. The warm colors (red, orange, and yellow) show regions with slower than normal velocities, the darker regions are faster than normal. From Su *et al.* (1994).

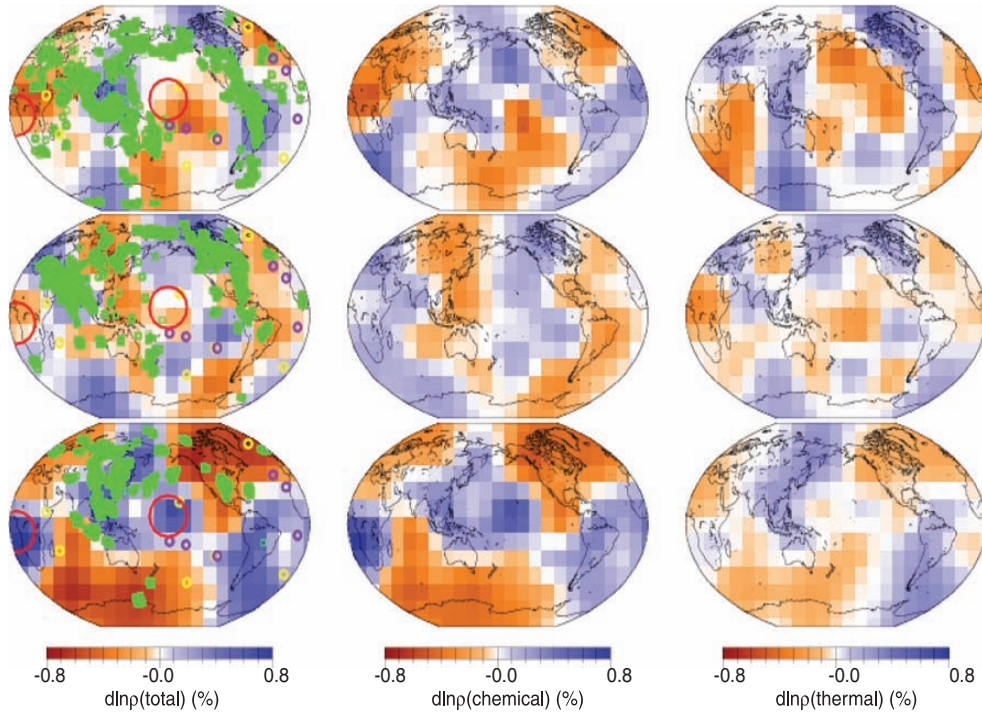


Figure 1.2.2.4: Total, chemical, and thermal contributions to relative density variations with respect to the average in the lower mantle. From the top, layers are between 670 and 1200, 1200 and 2000, and 2000 and 2891 km depth. From Trampert et al. (2004).

1.3 Laboratory measurements of elastic properties

Various techniques, based on physical acoustics, have been used to study the elastic behavior of materials by measuring directly V_P and V_S under ambient and elevated conditions; these include ultrasonic interferometry (MHz and GHz), impulsive stimulated light scattering (ISLS), resonant ultrasound spectroscopy (RUS) and Brillouin spectroscopy is also used to access to the elastic properties of materials.

Resonant Ultrasound Spectroscopy (RUS) is a method of measuring the complete elastic tensor of a material. It utilizes the fact that the mechanical vibration resonance spectrum depends on the geometry, mass density, and elastic tensor of the sample. Samples (generally parallelepipeds) are polished to a mirror finish on all six sides, and

accurate dimensions are obtained. The sample is then lightly sandwiched between transducers so that a resonance spectrum can be obtained. The spectrum (center frequencies of the resonance peaks) is then used as input data for a program, which adjusts the initially guessed elastic tensor until the calculated spectrum most closely matches the measured spectrum. Thus one must have a reliable method of computing the spectrum of 3D elastic solid. With resonant ultrasound spectroscopy (RUS), it is possible to determine the elastic constants of minerals at low pressures (max 0.2 GPa) with high precision and to temperatures in excess of 1800 K (Goto *et al.*, 1989; Isaak *et al.*, 1989).

The first Brillouin measurements of geological importance were carried out by Weidner *et al.* (1975). In combination with the diamond anvil cell, phases that are stable at high pressure and high temperature can be investigated. The first experiments at very high pressure were performed by Bassett and Brody (1977). If in addition combined with synchrotron radiation sound velocities and a material's volume (density) can be studied simultaneously. The relationship of acoustic velocity (v), phonon wave vector (q) and phonon frequency (ω_q) is given by:

$$\omega_q = v q$$

Acoustic velocities are related to elastic moduli and density of the sample, $v^2 = c / \rho$. Brillouin spectroscopy measurements in a diamond anvil cell have been carried out on single-crystal mineral samples at high temperature and to pressures over 1 Mbar (Murakami *et al.*, 2012) and to 2500 K at room pressure by laser heating (Sinogeikin *et al.*, 2004).

Impulsive stimulated light scattering (ISLS) is an experimental technique in which light is used to both produce and investigate the behavior of dynamic material gratings. Depending on the time scale of the experiment and the dominant interaction, the excited gratings may be acoustical or thermal in nature, or combinations thereof. The gratings are obtained by combining in the sample two laser pulses at a known angle of convergence. The diffracted intensity as a function of time after this event, of a frequency-doubled probe pulse is then recorded. ISLS has been used to measure the elastic constants of minerals to 20 GPa (Chai *et al.*, 1997; Abramson *et al.*, 1999).

Ultrasonic interferometry methods are explained in the **chapter 2.2**. Gigahertz-ultrasonic interferometry has been used to determine the elastic tensor of some minerals

to ± 10 GPa (Jacobsen *et al.*, 2004; Reichmann and Jacobsen, 2004; Kantor *et al.*, 2004). However, the diamond anvil cell permits only single-crystal studies on samples as thin as a few 10's of μm in length. The acoustic wavelengths in those minerals are reduced to a few micrometers (μm) and required to carry ultrasonic measurements to GHz frequencies.

Using solid pressure-transmitting media, MHz-frequency ultrasonic interferometry has been carried out in multi-anvil presses, enabling sound velocity measurements to be conducted up to simultaneous high pressures of 10 GPa and temperatures of 1,500 K (Li *et al.*, 1998). By combining the ultrasonic measurements with the x-ray diffraction and x-radiography techniques that now available at synchrotron facilities, simultaneous measurements of travel times, sample length and volume, temperature, and pressure can be obtained up to mantle conditions, 25 GPa and simultaneous temperatures 1200 K (Chantel *et al.*, 2012b).

2. In situ ultrasonic velocity measurement in multianvil apparatus

2.1 Experimental setup

2.1.1 Multianvil apparatus

The in-situ elastic wave velocity measurements reported here have been carried out in several multi anvil presses. A multi-anvil apparatus is one of a class of devices used to generate high pressure in the laboratory. In particular, they are part of a class of high pressure devices called Large Volume Presses (LVP) because the pressurized volume is on the order of millimeters or larger as opposed to the Diamond Anvil Cell (DAC) for which the pressurized volume is on the order of tens of microns. The name multi-anvil refers to the fact that the pressure is achieved by compressing the sample volume with a number of hard anvils. Nearly all high pressure devices utilize the principle that pressure (P) is equal to an applied force (F) divided by the area (A) over which it is applied: $P=F/A$; therefore, pressure can be increased by reducing the area over which force is applied. The anvils used in the multi anvil are composed of very strong materials (such as tungsten carbide (WC) or sintered polycrystalline diamond or boron nitride (BN)) and are designed so that they have a large surface area on one side and a small surface area on the side that contacts the pressurized volume. A multi-anvil apparatus can be thought of as having three main components: a hydraulic press that provides the force, a high-pressure module that contains the anvils and a sample assembly.

The multi-anvil apparatus requires a hydraulic press to generate force that drives the anvils together. Some presses are quite large and some are more modest in their dimensions. All of the presses rely on the pressurization of hydraulic fluid to drive a ram towards a stationary platen. The frame of the press keeps the hydraulic ram from

displacing the platen. In other words, the frame reacts the force generated by the ram and must therefore be very strong and very stiff. Common designs include thick tie rods with platens bolted onto them or an oval hole in a series of thick steel plates.

The module is a clever mechanical device that takes the simple forward motion of the hydraulic jack and converts it into the inward motion of the anvils. The exact geometry depends on the type of multi-anvil, but generally strong metal parts with angled faces that slide against each other accomplish this. During this thesis were used a Hymag split sphere Kawai- type multi-anvil compressed with a 1000-ton press (BGI, Bayreuth), a Sumitomo split sphere Kawai- type multi-anvil compressed with a 1200-ton press (BGI, Bayreuth), a Voggenreiter split sphere Kawai- type multi-anvil compressed with a 5000-ton press (BGI, Bayreuth), a T-10 Kawai-type module using 10 mm second-stage anvils (APS, Chicago) and a Voggenreiter DIA- type multi-anvil compressed with a 2400-ton press (ESRF, Grenoble) (**Figures 2.1.1**).

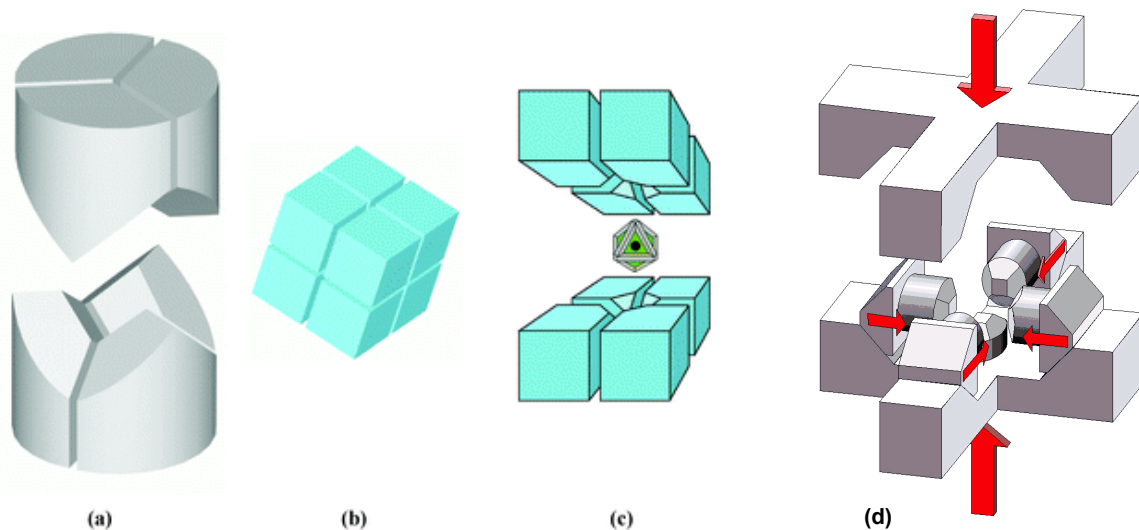


Figure 2.1.1: (a) 6 primary hard steel anvils in the Kawai geometry, (b) 8 tungsten carbide secondary anvils, (c) 8 tungsten carbide secondary anvils with pressure medium in green and gaskets in grey, (d) 6 primary hard steel anvils in the DIA geometry with the motion direction indicated by the red arrows. The assembly presented in (b) and (c) goes in the cavity in the center of (a) and (d)

2.1.2 Assembly

For all multi-anvils the compressed volume is called the "sample assembly". Sample assemblies vary widely in design and size depending on the pressure (P) temperature (T) conditions desired and what type of experiment is being conducted. Common elements of sample assemblies include a soft pressure medium in the shape of the compressed volume, a furnace that converts either AC or DC current into heat, a very soft confining media immediately adjacent to the sample and a sample jacket that protects the sample from chemical reactions with other parts of the sample assembly. Other components may also be part of the sample assembly, including thermocouples to measure temperature, hard pistons to either deform the sample or conduct ultrasound in and out of the sample assembly, or wires to measure the electrical properties of the sample.

The pressure media plays a very important role in the generation of high pressure in the multi-anvil. The pressure media (either in the shape of a cube or octahedral) is larger than the space between the anvils when the anvils are touching. During pressurization, the pressure media squeezes out into the spaces between the anvils until the friction between the pressure media and the anvils balances the pressure generated inside the sample assembly. Thus the pressure media must be soft enough to flow at room temperature but not so soft that it completely squeezes out between the anvils. Another function of the pressure media is to provide electrical insulation between the furnace, anvils, sample and any thermocouple or other sensor wires. The most commonly used materials are polycrystalline magnesium oxide, boron epoxy, mullite and pyrophyllite.

Furnaces use electrical resistance to heat the sample. A common geometry for the furnace is a tube that either contacts two of the anvils or is connected to two of the anvils by a conductive material. In order to ensure that the electrical current runs through the furnace, the two anvils that are touching the furnace must be electrically insulated from each other. Either AC or DC current may be used with the furnace. The choice of furnace material depends on the P-T conditions desired and whether or not the experiment requires diffraction from multiple directions or radiographic images. Common materials include graphite, which is x-ray transparent but converts to diamond at higher pressures

or lanthanum chromite (LaCrO_3), which is stable to higher temperatures and pressure but absorbs x-rays and is more difficult to use below 1000 C. In some cases metal foils, like rhenium in this thesis are also used as furnace materials.

The gaskets sit immediately adjacent to the sample. Their role is to protect the sample from the furnace, to distribute pressure evenly along the sides of the sample, and in some cases also functions as a sample jacket. In synchrotron experiments the confining media may also be used as a pressure standard. Common confining media include pyrophyllite and boron epoxy, which are soft, have a high melting temperature and are chemically inert.

The role of the sample capsule is to contain the sample and protect it from chemical reactions with other parts of the sample assembly. In some cases the confining media may serve as the sample jacket. Generally, if a separate jacket is used, it consists of a metal tube or foil, commonly platinum (Pt), gold (Au), or rhenium (Re). The choice of material depends on whether the experiment will be conducted in a synchrotron that requires an x-ray "transparent" material (e.g. Ni foil) or if the experimenter wishes to seal water into the sample (in which case they may choose a crimped Pt or Au tube that has been arc welded shut).

For the ultrasonic measurements, the all assembly required some modifications. Diagonally opposite corners of the uppermost cube are truncated and polished to mirror quality, yielding perfectly flat and parallel surfaces on which the transducer and assembly are mounted (**Figure 2.1.2**). This cube thus serves as a buffer rod to transmit the acoustic signals to and from the dense alumina buffer rod. **Figure 2.1.2** is a cross-section of the octahedral cell assembly and the buffer rod cube designed to perform acoustic velocity measurements.

The acoustic signals are generated and received using disk-shaped dual mode LiNbO_3 transducers (36° Y-cut for compressional wave and 41° X-cut for shear waves). A transducer with a gold-plated electrode diameter of 2 mm is mounted onto the exposed corner of the buffer rod cube using Aremco Crystalbond. A high temperature epoxy resin is used to mount the transducer onto the truncature for the high temperature experiments. A coaxial cable is used to connect the interferometer and the transducer. The copper core of a coaxial cable is directly welded to the transducer and the woven copper shield is

connected to the same anvil, used as ground. A 50 Ω resistor connected in parallel with the transducer provides appropriate electrical termination. At elevated pressure, the transducer remains stress-free since it is located in the gap between the first-stage anvils and the second-stage cubes, allowing precise travel-time measurements over a wide frequency range (10 to 70 MHz). However, during high temperature experiments, the temperature on the back of the cube, where is mounted the transducer, should be checked. The temperature should not exceed 70 °C, otherwise the crystal of LiNbO₃ undergoes a phase transition and the signal is lost.

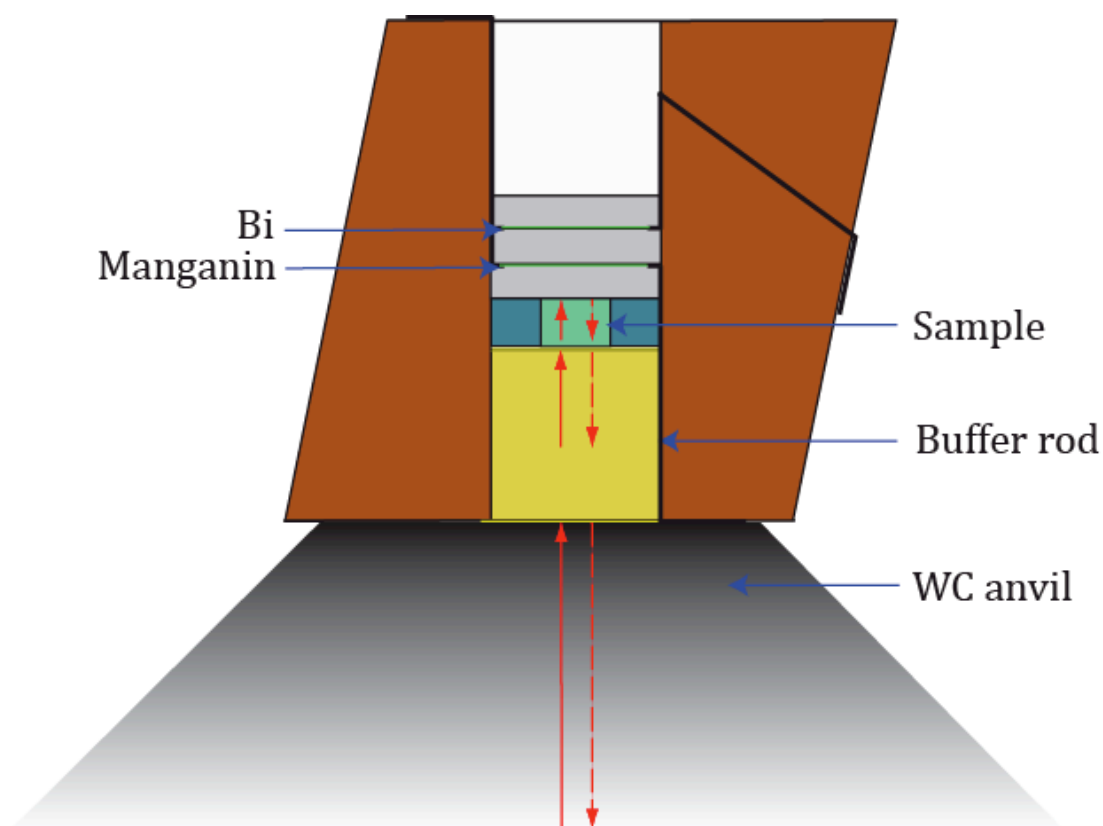


Figure 2.1.2: A cross-section of the WC buffer rod and the Cr-doped MgO octahedral cell assembly. A BN sleeve surrounds the sample to provide a pseudohydrostatic pressure environment. The pressure calibrants are enclosed between AgCl disks.

2.1.3 Fabrication of monomineralic, polycrystalline aggregates for ultrasonic wave propagation measurements at high pressures

Synthetic samples for ultrasonic wave propagation velocity measurement have to satisfy the following conditions in order to produce strong signal reflections with high signal to noise ratio (SNR) during ultrasonic wave propagation measurements.

According to Mason and McSkimin (1947), the attenuation A of a propagated wave depends on grain sizes a and wavelength l . Therefore, for a given wavelength, the grain size is the principal factor that controls the sample quality in terms of signal attenuation. Mason and McSkimin (1947) found that the bigger the grain size the higher the attenuation, i.e. $A=f(a)^2$. In addition, if the sample exhibits large grain sizes, the crystals will tend to form preferred orientation and the sample will become anisotropic. According to Liebermann et al. (1974), the ratio l/a must exceed three and it is recommended that $l/a > 10$. Anisotropy caused by even a small degree of preferred orientation within the polycrystalline specimen can produce directional dependence as well as pressure dependence of the measured wave propagation velocities, and should, therefore, be avoided.

The required specimen density is about 99% of the theoretical value and should be devoid of any micro-cracks. Lower density could result in reduced wave velocities in the solid phases. In addition, the received signal becomes weaker due to high inelastic absorption in the specimen.

The aspect ratio (l/f) must be less than 4 to 5 in order to avoid boundary effects during the measurements. General observations by Love (1927) indicate that in an isotropic elastic medium the first motion resulting from an arbitrary disturbance in an unbounded medium is propagated with the compression velocity V_p given by the equation:

$$V_p = [(\lambda + 2\mu)/\rho]^{1/2}$$

where λ = first Lamé parameter, μ = shear modulus, ρ = density. In laboratory experiments, for many practical reasons, the most convenient specimen shape is a cylinder, which is not really an unbounded medium. According to Birch (1960), the aspect ratio l/f of the specimen should not exceed four or five for successful P-wave

measurements. Larger values of l/f seriously affect the recorded signals by boundary reflections and only a small portion of the energy will arrive with velocity V_P and tends to fade to the noise level, while large portions of the energy will travel with the ‘rod/bar velocity’ $V_{PR} = (E/\rho)^{1/2}$, (with E = Young’s modulus) that is lower than V_P .

Studies by Tu et al. (1955) and Silaeva and Shamina (1958) show that, depending on the relationship between sample diameter and wavelength of the elastic wave propagating through the sample, the measured velocity could be the velocity of longitudinal waves in an infinite medium V_{PM} , in a plate V_{PPL} in a thin rod V_{PR} . To warrant that the measured velocity in our sound velocity propagation studies is indeed V_{PM} , the ratio between sample diameter and wavelength (f/l) must not fall below 2.4.

Dispersion of travel time (velocity) depends on the quality of the contact between the transducer, the buffer rod and the sample; therefore, both sides of the sample need to be polished flat and parallel. In addition, the insertion of thin gold foils (2 μm thickness) between the interfaces can be utilized to optimize elastic energy propagation by enhancing the mechanic coupling. Both ends of each cylindrical specimen need to be ground and polished. Their flatness and parallelism is ensued by using diamond paste of 6, 3 and 1 μm in succession, with the final finish being accomplished using 1/4 μm diamond paste. The dense Al_2O_3 buffer rod is also polished using the same procedure.

2.1.4 Pressure calibration

The simplest way to think about the pressure inside a multi-anvil cell is to use relationship between pressure and force over area. From this simple equation, in theory, one should be able to calculate the pressure inside the cell by knowing how hard one is pushing on the outside surfaces of the anvils and knowing the surface area of the anvil faces. However, it turns out that it is not that simple. In the section about pressure media, we discussed how the pressure media squeezes out between the anvils until the friction between the media and the sides of the anvils balances the pressure inside. This friction adds significantly to the force that one must apply to the anvils to move them inwards and because the degree to which the pressure media squeezes out and the room temperature

shear strength of the pressure media are not well known or even entirely knowable, the frictional force is also unknown. Therefore, the pressure inside the cell must be measured in some other fashion. Prior to the use of synchrotron x-rays, the only way to determine the pressure in the cell was to develop a calibration curve for each sample assembly design that allowed one to determine the pressure inside the cell from the pressure in the hydraulic fluid that drives the hydraulic rams. Phase transformations that occur at well-known PT conditions are used to determine the calibration curves. For *ex situ* experiments, the cell assembly includes the two pressure calibrants Bi, (or ZnS, for higher pressures) and Manganin wire (**Figure 2.1.2**). The electrical resistance of Manganin was measured under pressure up to 9 GPa and calibrated against well-known fixed points; the Bi phase transitions (Bi I-Bi II at 2.55 GPa and Bi III-Bi IV at 7.70 GPa) and the ZnS phase transition at 15.5 GPa. Obtained results show a linear relationship between the resistance of the Manganin and the pressure up to 9 GPa and can therefore be used to estimate any intermediate pressure. With the advent of multi-anvil designs that can accommodate synchrotron x-rays, in-situ measurements of pressure inside the multi cell became possible. In this case a pressure standard is used. Good pressure standards need to have several features. First it must have low shear strength so that the pressure within is fairly hydrostatic. Second it must be fairly compliant; in other words, there needs to be a relatively large change in its unit cell dimensions as pressure increases. Third, the equation of state (EOS) for the material must be well known. The EOS is the relationship between unit cell volume and pressure and temperature (**Appendix 1**). The calibration of pressure of the multi-anvil press (**Figure 2.1.4.1**) installed at ID06, ESRF, was performed for a 10/4 assembly (10 mm: the length of the edge of the MgO octahedra and 4 mm: the length of the truncation of the WC anvils) up to 14 GPa. X-ray diffraction data were collected on a NaCl pressure marker placed in the centre of the assembly. From those data and using the well established equation-of-state of NaCl (which is a thermodynamic equations describing the state of matter under a given set of physical conditions.) (Decker, 1971), the pressure was determined (**Figure 2.1.4.2**). Several runs have been conducted following this procedure and the pressure generated for a given oil pressure is very reliable.

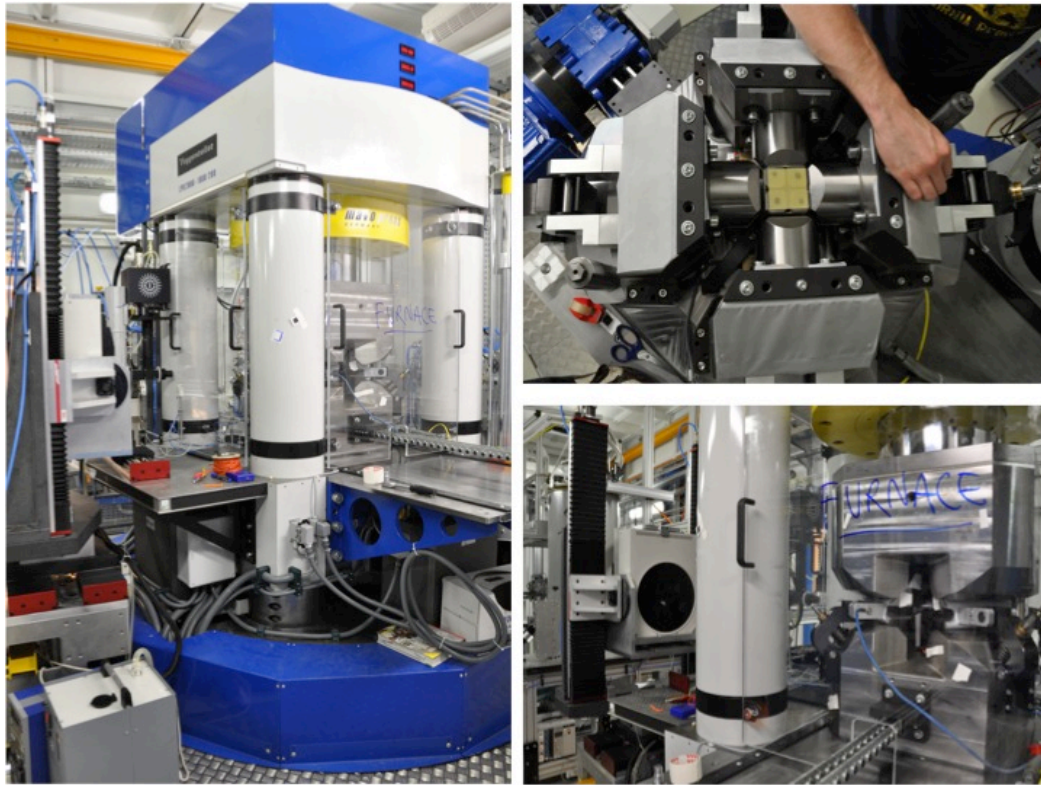


Figure 2.1.4.1: Pictures of the 2000ton D-DIA-type multi-anvil press in the EH2 at ID06.

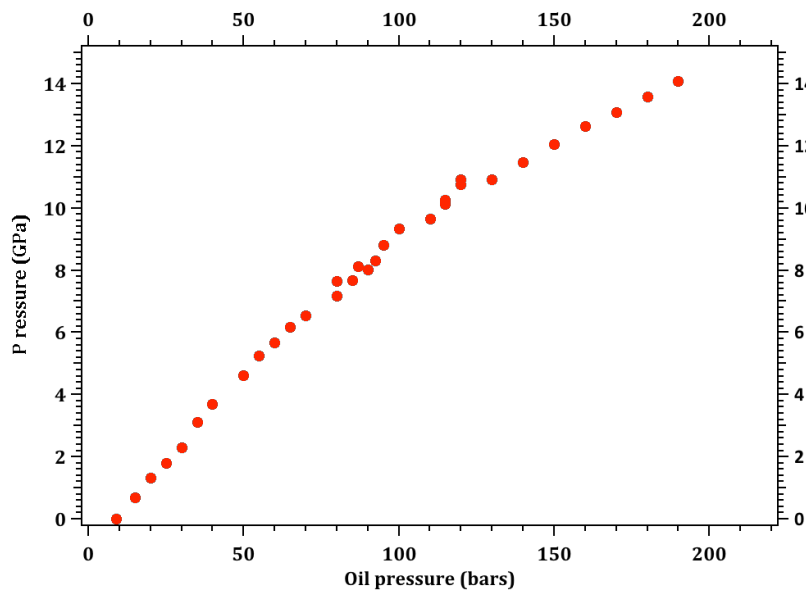


Figure 2.1.4.2: Calibration curve for the 10/4 assembly at room temperature. The red points represent the pressure obtained from the in situ X-ray diffraction of NaCl.

Pressure is generally envisioned to be "hydrostatic" within the multi-anvil cell, but the confining media are quite strong relative to fluids (which produce genuinely hydrostatic conditions) so there is some level of nonhydrostatic stress within the sample. The level of nonhydrostatic stress depends on the temperature of the confining media and the design of the sample cell and is usually not well known. The uncertainty in pressure and temperature is compounded by the fact that all high-pressure methods suffer from some degree of uncertainty, so even the "well calibrated geothermometer" and the material with a "well known equation of state" are not known with absolute certainty. Therefore, as with all science, one must keep in the back of one's mind that future technological advances may force us to revisit results that are considered state of the art today. Perhaps the greatest comfort to multi-anvil users is that the seismic discontinuities at 410, 520 and 670 km show up at the right depths to match the laboratory determined pressures for the phase transformations from olivine to wadselyite to ringwoodite and then to perovskite and magnesiowustite.

2.1.5 Temperature calibration

Temperature inside the multi-anvil cell can be determined in two ways; with a thermocouple or by a calibration curve that relates temperature to the power dissipated by the furnace. Because the thermocouple wires must emerge from the cell between the gaps in the anvils, where the pressure medium is squeezing out, they must be very strong. The most common wires used are a W-Re alloys. Thermocouples often do not survive for the duration of the experiment and can be difficult to fabricate. Therefore some experimentalists choose to make a series of experiments with a given sample assembly where the sample consists of a pair of minerals that participate in a well-calibrated geothermometer. Each experiment is conducted at a different furnace power. After the experiment is over the sample are analyzed to determine the temperature and a power versus temperature calibration curve is constructed. The temperature in subsequent experiments can then be derived from the record of the power applied to the furnace.

Uncertainty in pressure and temperature are related in that one generally feeds into the other. The pressure in the cell changes during heating and cooling due to thermal expansion and contraction of the cell parts. Pressure standards are usually temperature dependent and even the voltage produced by thermocouples is affected by pressure. Since the temperature at the interface between the pressure media and the anvil is relatively low (<50 C), there will be substantial temperature gradient between the hot spot of the furnace and the outside of the cell. Cell designs attempt to produce relatively small temperature gradients within the sample, but there are always some variations in temperature across the sample.

2.1.6 Transducer

Piezoelectricity is a physical property only occurring in crystals having a crystallographic polar axis. When an external force is applied and deforms the crystal an electrical voltage can be measured between opposite faces of the crystal. On the other hand, if an external electrical field is applied to a piezoelectric crystal, it will deform (converse piezoelectric effect; **Figure 2.1.6**).

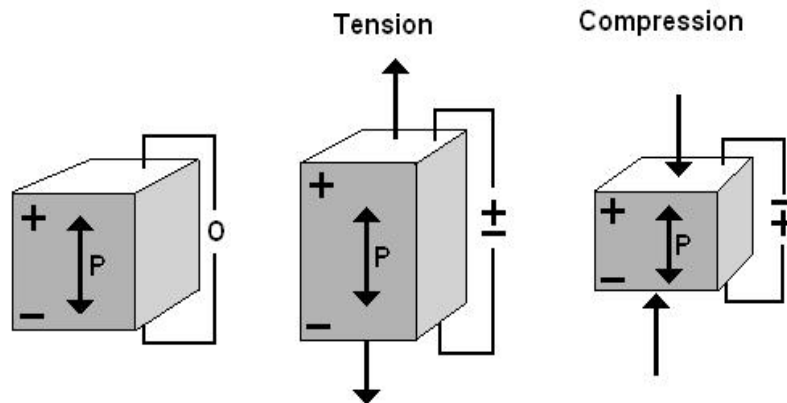


Figure 2.1.6: *The converse piezoelectric effect of a piezoelectric crystal.*

A piezoelectric transducer is a chip cut from a polar crystal in such a way that it produces compressional waves; shear waves or both simultaneously when an electrical AC-potential is applied. The strongest amplitude of vibration is obtained when the crystal vibrates at its resonance frequency. In this study, 10 degree rotated Y-cut lithium niobate

is used to generate both compressional and shear wave simultaneously. The resonance frequency for compressional waves is ≈ 16.7 MHz and for shear waves it is ≈ 10 MHz. Therefore, applying a 50 MHz AC field a compressional wave is excited at the resonant frequency through its 3rd harmonic. Simultaneously, a shear wave is generated at resonant condition by excitation of its 5th harmonic.

2.1.7 Synchrotron X-Ray Studies using the Multianvil

Synchrotrons are particle accelerators that can be used to produce high fluxes of energetic x-rays that will penetrate substantial quantities of low Z materials (Z stands for atomic number). WC is not x-ray transparent but materials like magnesium oxide, pyrophyllite and Boron epoxy are. Multianvil devices are particularly well suited for use with synchrotron x-rays because the x-rays can pass through the gaps between the anvils where the pressure media is squeezing out and enter the high-pressure region. There are both DIA designs and 6/8 designs that can be used with synchrotron x-rays. Synchrotrons that produce the type of x-rays required for these experiments are very expensive and very large; there are only a small number of such facilities worldwide. Since multianvil presses are not very portable, one generally takes the sample assembly to a synchrotron that has the type of multianvil press that one wants to use. Synchrotron beam lines with multianvil presses include for this thesis ID06 (ESRF, Grenoble) and 13 ID-D (Gsecars, APS, Chicago).

By combining ultrasonic measurements with the x-ray diffraction and x-radiography techniques now available at synchrotron facilities (APS and recently on ID06, ESRF), simultaneous measurements of travel times, sample length and unit-cell volume, temperature, and pressure can be obtained. Additional technical details about each element of such integrated experiments follow.

- With synchrotron x-ray diffraction one can determine the unit-cell volumes of the sample and pressure standard and then obtain the density of the sample and the absolute pressure derivate from the equation of state.
- Using x-ray radiography techniques, it is possible to monitor changes of sample length directly under high pressures and temperatures during the ultrasonic

measurements. The exact length of the sample at each ultrasonic measurement is required to calculate the proper velocities.

- The setup used with the pulse echo overlap method allows much faster data collection of acoustic data and subsequent analysis offline than the one scanning of the frequency range. It permits to reduce the duration the experiment that is crucial during synchrotron experiments.
- Simultaneous measurement of both V_P and V_S on the same specimen under the same high pressure and temperature conditions by using dual-mode lithium niobate transducers.

By using these techniques, it is now possible to perform high-frequency (10- to 70-MHz) measurements of both P and S wave velocities on millimeter-sized polycrystalline or single- crystal samples to pressures of 25 GPa and simultaneous temperatures 1200 K (Chantel *et al.*, 2012b). Angle dispersive (ESRF) or energy dispersive (APS) X-ray diffraction pattern of the sample were collected (**Figure 2.1.7.2**) at each pressure, while the ultrasonic measurements were conducted, using an image plate detector MAR 345 (**Figure 2.1.7.1**), or cyberstar scintillation detector.

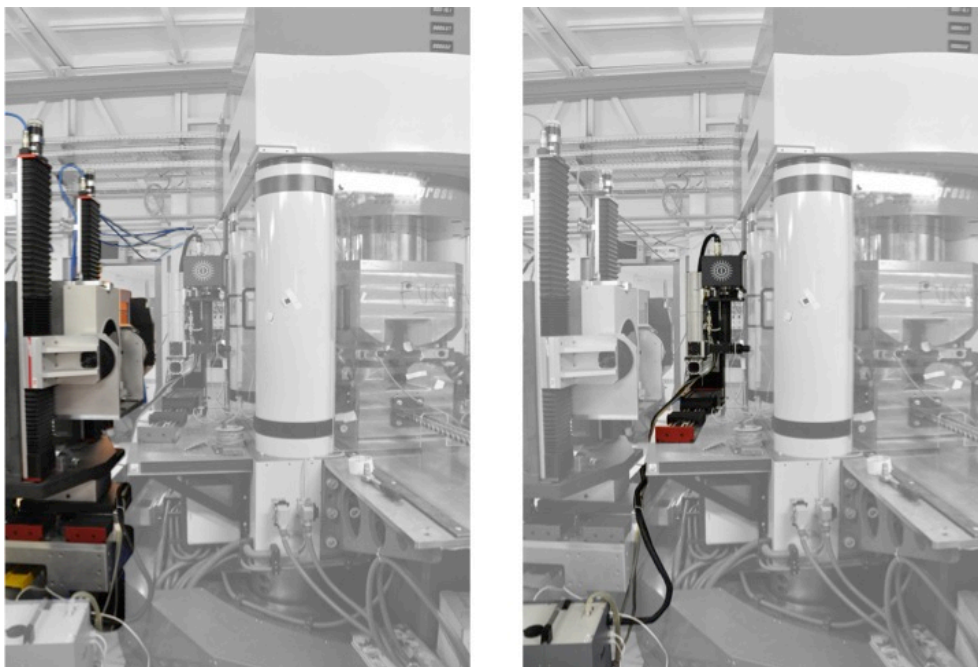


Figure 2.1.7.1: The picture on the left shows the image plate MAR 345, the right one shows the Frelon CCD camera.

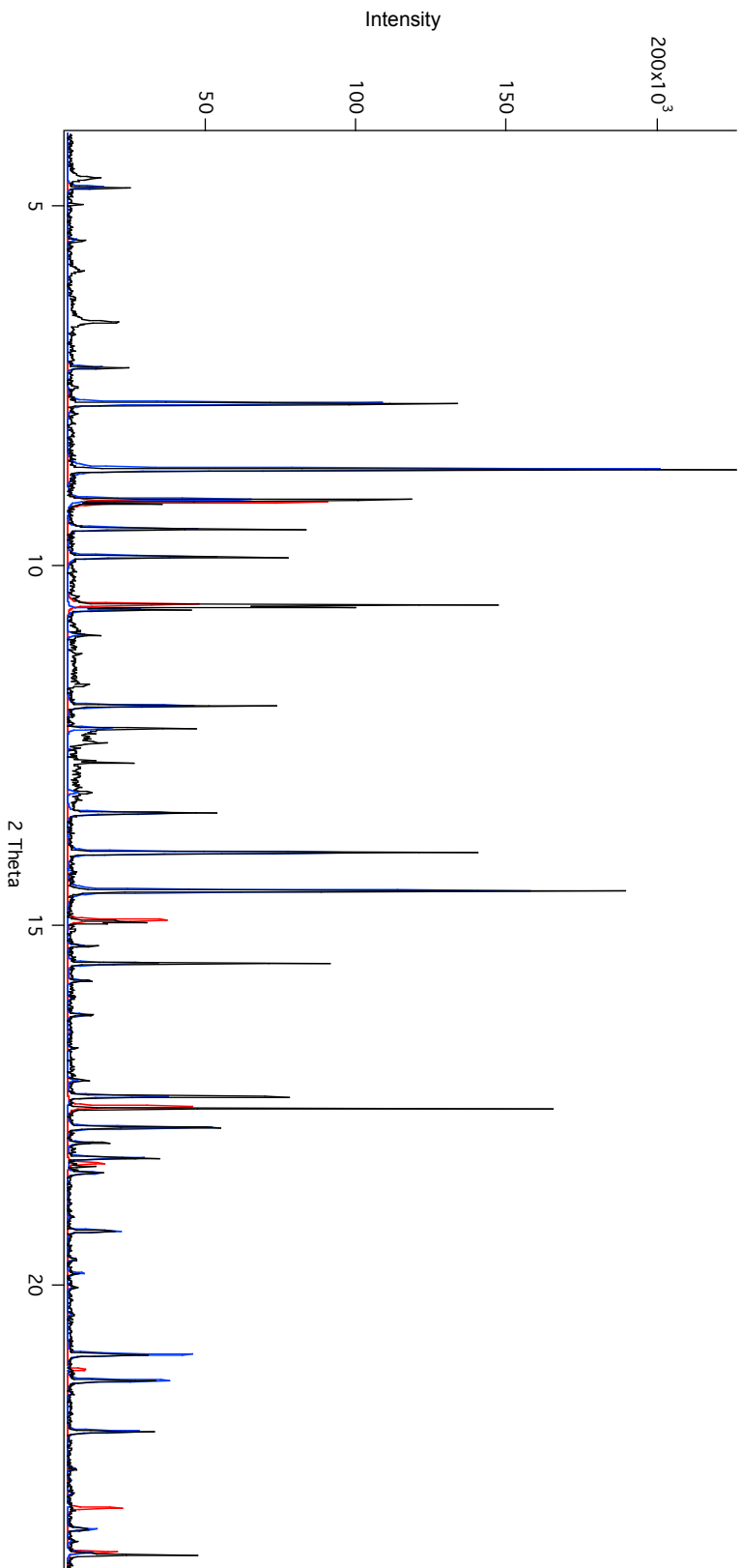


Figure 2.1.7.2: X-ray diffraction pattern of Py50Mf50 at 9.4 Gpa and room temperature (blue: pyrope, red: gold)

2.2 Data acquisition and processing

A MHz ultrasonic interferometer with both compressional and shear-waves capabilities has been adapted for high-pressure and high-temperature elasticity measurements in a multi-anvil apparatus by Stony Brook group (Li *et al.*, 1996). To perform ultrasonic measurements, two different methods have been developed; the phase comparison (Rigden *et al.*, 1988; Niesler and Jackson, 1989) and the pulse echo overlap methods (Papadakis, 1990). During those studies, the phase comparison method was used for measurements at room temperature at the Bayerisches Geoinstitut and the European Synchrotron Radiation Facility (ESRF). The pulse echo overlap method was employed during the experiments at high temperatures in conjunction with synchrotron radiation at the Advanced Photon Source (APS).

2.2.1 Phase comparison method

2.2.1.1 Principles

The ultrasonic phase comparison method has been described in detail in previous studies (Rigden *et al.*, 1988, 1992; Niesler and Jackson, 1989). The output from a continuous wave source is gated to produce a pair of phase coherent high frequency pulses. These pulses are applied to a transducer, which is bonded to the back of a WC anvil. The elastic waves generated by each pulse are reflected and transmitted at the WC cube/buffer rod/sample interfaces, and the transmitted portion reverberates inside the cube, buffer rod and sample. As the transducer also acts as a receiver, it transmits a series of echoes, generated by the reflection of the elastic waves at each interface, to the oscilloscope. By increasing the width of the pulse, the first buffer echo will superimpose with the first sample echo from the first source pulse. The phase difference between the superimposed buffer rod and sample echoes can be expressed as $\omega t'$, where ω is the angular frequency of the wave and t' is the apparent two-way travel time of the sample.

As the carrier frequency is varied, alternate constructive and destructive interference between the superimposed signals will occur, resulting in a series of maxima and minima on the amplitude spectrum modulated by the transducer response envelope. The interference extrema occur at frequencies where the phase difference are $\omega t' = n\pi$ for the superimposed echoes. This can be also written as $t' = p/f$, where $p = n/2$ can have either integral or half-integral values. In other words, at frequency f , there are p periods in the round-trip travel time through the sample. Frequencies for p th and $(p + n)$ th extrema, f_p and f_{p+n} , can be used to estimate the travel time by:

$$t'_{est} = n / (f_{p+n} - f_p) \quad (2.2.2.1.1)$$

The p value is calculated from $p = f_p t'_{est}$, the closest half or integral value is therefore assigned to frequency f_p and all remaining extrema can be assigned sequentially. In practice, the interference minima are normally used to reduce the travel-time data because they are sharper than the maxima.

In all these studies, thin (50 μm), gold foils are used as bond between the WC anvil and the buffer rod and between the buffer rod and the sample to increase the quality of the acoustic contact. A correction needs then to be applied to the raw data to subtract the effect of this bond. The contribution to the measured travel time from a bond of known thickness and acoustic impedance can be removed (Davies and O'Connell, 1977; Jackson *et al.*, 1981; Niesler and Jackson, 1989). The intrinsic travel time t through the sample is obtained by subtracting the bond effect, i.e.

$$t = t' - \phi / 2\pi f \quad (2.2.2.1.2)$$

where ϕ is the total bond phase shift between the buffer rod and the sample.

2.2.1.2 Instrumentation

This setup has been derived from the GHz ultrasonic interferometer developed for the diamond anvil cell by Jacobsen *et al.* (2005). The high-frequency ultrasonic interferometer consists of five main components:

- A Gigatronics 6062A radio-frequency (RF) generator provides a highly stable RF source to the interferometer with an output power up to 12 dB.

- A Stanford Research Systems *DG535* Digital Delay/Pulse generator gates the continuous output from the RF generator to provide phase-coherent pulses of programmable duration and delay.
- A signal amplifier is also used to increase the amplitude of the generated pulses and the signal-to-noise ratio.
- A digitizing oscilloscope, *HP54750*, which has GHz-bandwidth and picosecond resolution, well beyond, that required for the use of MHz frequencies.
- A PC, with IEEE 488.2 interface, drives the system and saves the raw amplitude data.

All the components of this setup needs to be connected as shown on the **Figure 2.2.1.2**. The data collection and data reduction for the phase comparison method are explained in the **Appendix 2**.

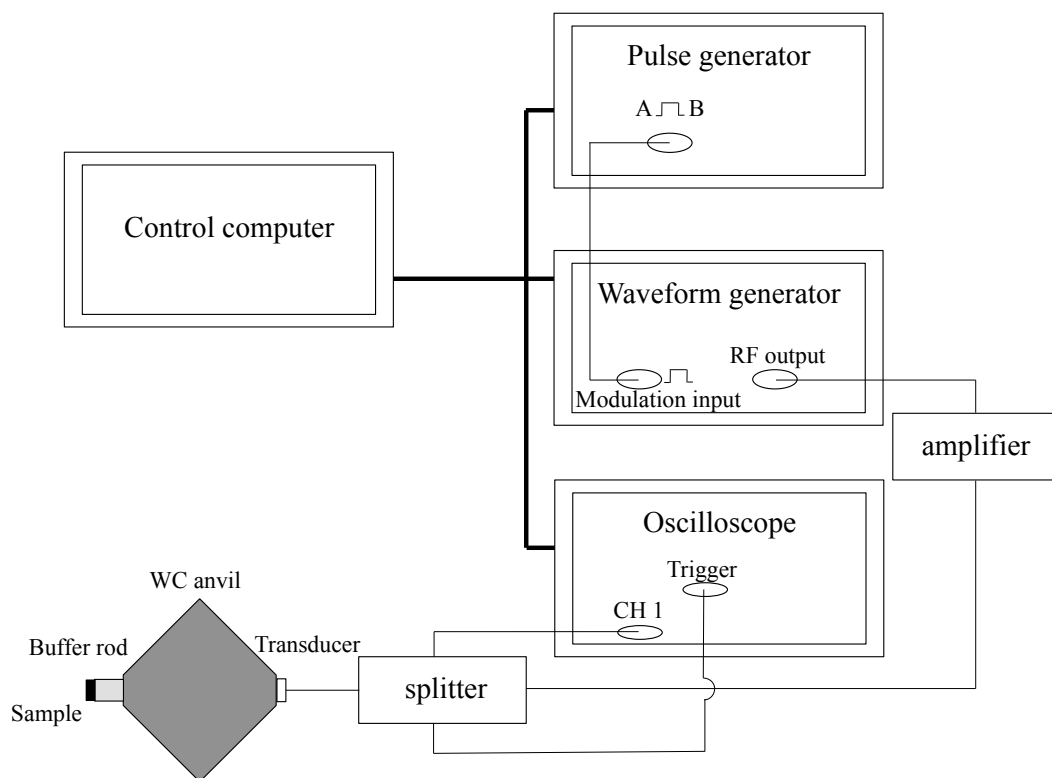


Figure 2.2.1.2: Ultrasonic setup used at BGI and ESRF.

2.2.2 Pulse echo overlap

2.2.2.1 Principle

The seismic method employed for the experiments conducted in conjunction with synchrotron is based on the transfer function of the entire system including the transducer, the WC anvil, the buffer rod and the sample. The high-frequency ultrasonic interferometer is composed of:

- The waveform generator Sony Tektronix *AWG2021* with a graphical user interface allowing the easy creation of composite signals with an on-screen viewing of waveform editing. By editing a signal with a definite width, one can eliminate the pulse generator from this setup.
- The Tektronix *TDS5104* oscilloscope is a graph-displaying device. It incorporates a computer using *Windows* operating system. The included application, *Wave writer*, displays the received signal and allows saving the whole signal as a single file.

All the components of this setup needs to be connected as shown on the **Figure 2.2.2.1**. The data collection and data reduction for the phase comparison method are explained in the **Appendix 3**.

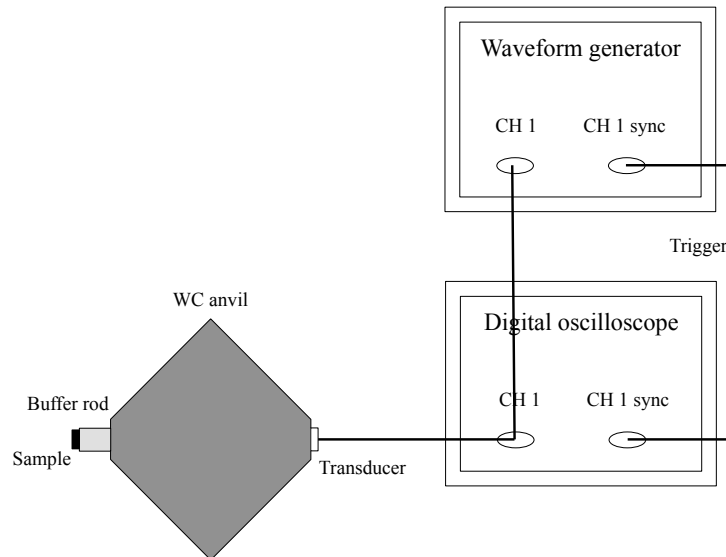


Figure 2.2.2.1 presents the ultrasonic velocity measurement set-up used at APS.

The initial signal $x(t)$ is created by the waveform generator and sent to the transducer. The response $y(t)$ is converted to an electrical signal by the transducer and recorded together with the initial stimulus $x(t)$ by a digital oscilloscope. This procedure is repeated several hundred times to obtain a good signal/noise ratio by stacking the recorded signal. The computer defines the original signal $x(t)$ and records the final stacked response $y(t)$ for further processing.

2.2.2.2 Acquisition of the transfer function

In a linear time invariant (LTI) system the response function $y(t)$ is the convolution of the transfer function $h(t)$ and the stimulus function $x(t)$. The transfer function $h(t)$ is identical with the response function if the system is stimulated by a Dirac pulse $\delta(t)$:

$$(2.2.2.2.1) \quad h(t) = [\text{LTI-system}] * \delta(t)$$

In frequency domain the response $Y(f)$ is obtained by multiplying the Fourier-transforms

$$(2.2.2.2.2) \quad Y(f) = H(f) \cdot X(f)$$

with

$$(2.2.2.2.3) \quad H(f) = \int_{-\infty}^{+\infty} h(t) e^{-i2\pi ft} df$$

and

$$(2.2.2.2.4) \quad X(f) = \int_{-\infty}^{+\infty} x(t) e^{-i2\pi ft} dt$$

The Fourier-transform of the Dirac pulse $\delta(t)$ is the white spectrum $D(f) = 1$ containing all frequencies from $-\infty$ to $+\infty$ Hz at the same amplitude. However, the generation of an ideal Dirac pulse is not feasible in the real world. Therefore, an approximation $D^*(f)$ comprising a frequency range f_{min} to f_{max} at constant amplitude is used as stimulus function to obtain an approximate transfer function $H^*(f)$ or, in time domain, $h^*(t)$. The approximate Dirac pulse $d^*(t)$ is obtained by the inverse Fourier-transform of $D^*(f)$ limiting the frequency range from $f_{min} = f_c - \Delta f$ to $f_{max} = f_c + \Delta f$, where f_c is the center

frequency and $2\Delta f$ is the full frequency range. $d^*(t)$ is the input signal used for the experiments. It is calculated from:

$$(2.2.2.2.5) \quad x(t) = d * (t) = \int_{f_c - \Delta f}^{f_c + \Delta f} D * (f) e^{i2\pi ft} df = 2 \frac{\sin(2\pi\Delta ft)}{2\pi\Delta ft} = 2 \operatorname{sinc}(2\pi\Delta ft)$$

The $\operatorname{sinc}(2\pi\Delta ft)$ function is shown in **Figure 2.2.2.2.1** for two different frequency ranges. If the signal $x(t)$ spans a wider range of frequencies then it is sharper in time domain (**Figure 2.2.2.2.2**).

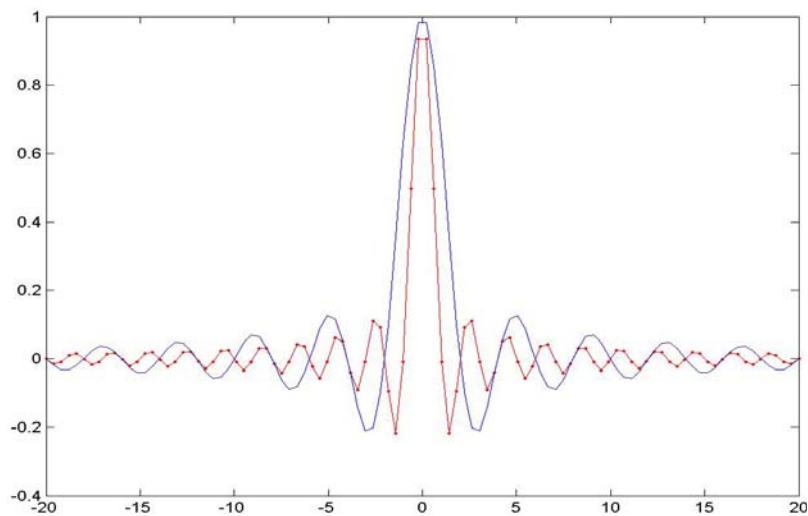


Figure 2.2.2.2.1: $\operatorname{sinc}(t)$ function with $\Delta f = 20\text{MHz}$ (red) and $\Delta f = 10\text{MHz}$ (blue).

The response function $h^*(t)$,

$$(2.2.2.2.6) \quad h^*(t) = [\text{LTI-system}] * \operatorname{sinc}(kt)$$

with $k=2\pi\Delta f$, is a good approximation for the transfer function in the selected frequency range, provided the amplitudes are relatively small (**Figure 2.2.2.2.2**).

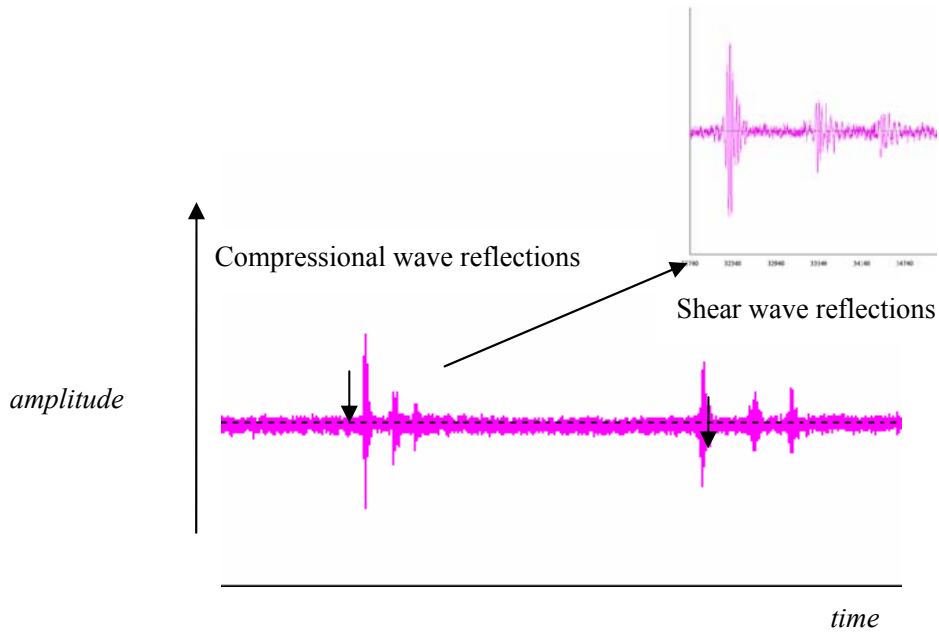


Figure 2.2.2.2.2: Example of recorded signals after acquisition. P and S reflections show as finite wavelets.

2.2.2.3 Travel time measurements

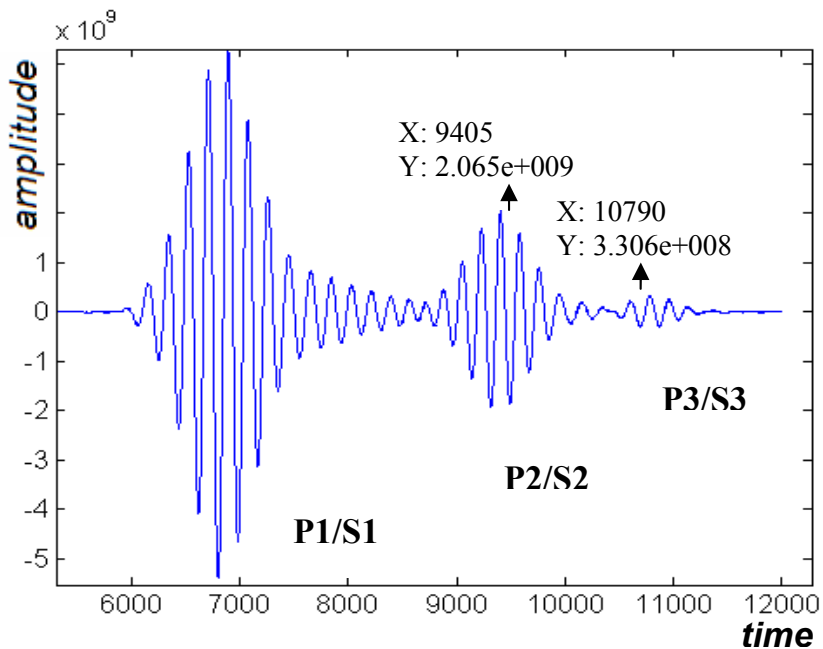


Figure 2.2.2.3: Cross correlation function r_{xy} used for accurate time picking of the recorded signal.

A combination of cross-correlation function and train alignment is used to define the peak-to-peak time differences between the reflection wavelets from the top and the bottom of the sample. The wavelet of the reflection from the bottom of the corundum (P2/S2), $x(n)$, is cross-correlated with the entire wave train, $y(n)$. Local maxima on the cross-correlation function indicate the arrival time at each interface.

$$(2.2.2.3.1) \quad r_{xy}(l) = \sum_{n=-\infty}^{\infty} x(n+l)y(n)$$

Where $l=0, \pm 1, \pm 2, \pm 3, \dots$

To ensure the consistency of the time pickings for the same sample at various pressures the wave trains are aligned by the first reflection (from the top of the buffer rod) and arranged side by side as illustrated in **Figure 2.3.2.3**. The two-way travel time of the signals travelling through the sample is equal to the difference in arrival time between the reflections from the top and the bottom of the sample:

$$(2.2.2.3.2) \quad t_{P,S} = \frac{1}{2}(t_{P3,S3} - t_{P2,S2})$$

2.2.3 Length of the sample

2.2.3.1 Cook Method

Assuming that 1) the pressure is isotropic and 2) deformation of the sample at high pressure is elastic, the length of the sample can be calculated by the method introduced by Cook (Cook, 1957):

$$(2.2.3.1.1) \quad \frac{l_0}{l} = 1 + \frac{1 + \Delta}{3h_0} \int_0^P \frac{dP}{\frac{1}{t_p^2} - \frac{4}{3t_s^2}}$$

$$(2.2.3.1.2) \quad h_0 = 4l_0^2 \rho_0$$

where

l_0 is initial length of the sample at room pressure,

l is the length of the sample at pressure P ,

ρ_0 is the density of sample at ambient condition,

$\Delta \approx 0.01$ (for most isotropic solids) and

t_p , t_s are travel times of compressional (P) and shear waves (S) through the sample.

2.2.3.2 X-ray radiography

Using the synchrotron facilities, one can determine the sample length under high pressure, images were captured at each pressure using a Frelon CCD camera (**Figure 2.1.7.1**), or a Sensicam. As the sample is surrounded by gold foils, one can precisely measure its length by the contrast of absorption (**Figure 2.2.3.2**).

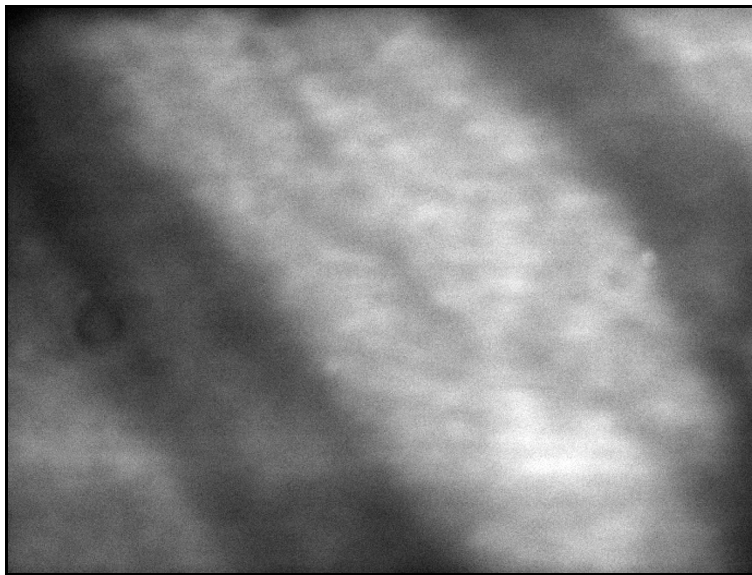


Figure 2.2.3.2: Image of the sample under high pressure. The darker areas, from the absorption contrast, are the gold foils surrounding the sample, appearing in the central region.

3. The elasticity of lawsonite at high pressure and the origin of low velocity layers in subduction zones

3.1 Introduction

Subducting slabs are colder than the surrounding mantle and hence appear, on the whole, to be seismically faster (Creager and Jordan, 1984, 1986; Davies and McKenzie, 1969; Fischer *et al.* 1991; Sleep, 1973). However, in several northern circum-Pacific subduction zones detailed seismic investigations have proposed a more complex layered structure with the presence of a low velocity layer (LVL) that appears to persist to depths of 100 to 250 km (Abers and Sarker, 1996; Gubbins and Snieder, 1991; Gubbins *et al.*, 1994; Hacker, 1996; Helffrich and Stein, 1993; Helffrich, 1996; Matsuzawa *et al.*, 1987). It has been estimated that seismic waves may travel 3 to 10% slower within the top of the subducting slabs compared with the surrounding mantle (Abers, 2000; Connolly and Kerrick, 2002; Kawakatsu and Watada, 2007; Peacock and Wang, 1999). Body-wave dispersion characteristics suggest this LVL may be 5 to 8 km thick. (Abers and Sarker, 1996; Abers, 2000; Helffrich, 1996; Helffrich and Abers, 1997; Lin *et al.*, 1999; Matsuzawa *et al.*, 1987). Oceanic crust is typically ~7 km thick (Mutter and Mutter, 1993; White *et al.*, 1992), implying that the LVL is of comparable thickness (Helffrich and Abers, 1997).

Oceanic crust consists of mafic rocks that has undergone alteration through interaction with seawater. The oceanic crust transforms during subduction to eclogite at depths of 20-50 km (Ringwood and Green, 1966; Schmidt and Poli, 1998). Anhydrous eclogite cannot explain the existence of the LVL because its compressional velocity, V_P , is similar to or exceeding that of the surrounding peridotite (Gubbins *et al.*, 1994). A number of further explanations have been proposed mainly attributing the LVL to either

the presence of H₂O or the persistence of metastable basaltic rocks (Abers, 2000; Gubbins *et al.*, 1994; Helffrich and Stein, 1993) at depth. None of these seems to fully explain the appearance of the LVL, however. Although seismic wave velocities in metastable basalt would be 10-15% slower than the surrounding mantle at depth >50 km, the LVL persists to depths over 100 km and it is not possible for basalt to remain metastable to these conditions. A similar argument can be used to discount the presence of serpentinised layers above or within the slab as an explanation because the reported depth range for the LVL is beyond the stability field of serpentine (Ulmer and Trommsdorff, 1995). The presence of free H₂O-rich fluids might reduce seismic velocities, but calculations indicate that isolated pores with a porosity of 5-10% would be required to fully explain the observed LVL (Abers, 2000; Watson and Lupulescu, 1993) and this would necessitate far more H₂O than that expected to be available during subduction (Schmidt and Poli, 1998). Predicted ratios of shear to compressional wave velocities (V_S / V_P) for a partial-melt layer atop the subducting slab (Abers, 2000; Faul *et al.*, 1994) lie above the LVL observations and a thick partially molten layer of a few kilometers is difficult to reconcile with thermal models that suggest subsolidus conditions at the top of the slab (Peacock, 1993).

One plausible explanation for the LVL, however, is the presence of the hydrous mineral lawsonite ($\text{CaAl}_2\{\text{Si}_2\text{O}_7\}\{\text{OH}\}_2\cdot\text{H}_2\text{O}$) and the formation of lawsonite-bearing blueschists and eclogites from hydrated oceanic crust at the temperatures and pressures relevant to the subduction zone (Connolly and Kerrick, 2002). Experimental results indicate that lawsonite can exist in subduction zones at depths of 100 to 250 km depending on the subduction geotherm (Abers, 2000; Fujimoto *et al.*, 2010; Lin *et al.*, 1999; Pawley and Holloway, 1993; Schmidt and Poli, 1998). Although the proportion of lawsonite in rocks forming directly from altered oceanic crust may be small, this may be supplemented through influxes of H₂O coming from either the dehydration of serpentine in layers below the oceanic crust or from fluids travelling up-dip within the slab and originating from dehydration at greater depths. Consequently, some calculations indicate that lawsonite may comprise up to 20 % of the subducted crust over certain depth intervals (Connolly and Kerrick 2002).

Despite being a potentially important phase, the full elastic tensor constants and the compressional and shear wave velocities of lawsonite at the high pressures relevant to subduction zone conditions are unknown. The V_P of lawsonite has been recently reported up to 1 GPa and 400 °C (Fuis *et al.*, 1991; Fujimoto *et al.*, 2010), while single-crystal elastic constant tensors have been measured at 1 bar (Sinogeikin *et al.*, 2000a) and up to 723 K (Schilling *et al.*, 2003). In this study, high-pressure ultrasonic measurements were conducted to determine both V_P and V_S in samples of polycrystalline lawsonite up to 8 GPa.

3.2 Experimental Methods

3.2.1 Lawsonite synthesis and hot pressing

The starting material was synthesized from chemical reagents, CaCO_3 , SiO_2 , Al_2O_3 , $\text{Al}(\text{OH})_3$, initially mixed in the absence of the required amount of $\text{Al}(\text{OH})_3$ to yield the correct mineral composition. A glass was produced by melting the anhydrous mixture at 1600°C for 5 hours, followed by grinding to a fine powder. The recovered powder was then remelted and quenched once more to a glass and the procedure repeated. The required amount of $\text{Al}(\text{OH})_3$ was then mixed with the glass powder. This starting material was then transformed to a hot pressed lawsonite polycrystalline aggregate in a multi-anvil experiment (# H3057) employing a uniaxial split-sphere apparatus (Hymag 1000-ton) at the Bayerisches Geoinstitut. The powder was encapsulated in a capsule composed of 25 μm thick Re foil that was 4 mm in diameter and 4 mm long. A 25/17 octahedral cell assembly was used, employing a LaCrO_3 heater. The sample was separated from the heater by MgO spacers. Temperature within the cell was monitored by W3%Re and W25%Re thermocouple inserted axially and in direct contact with the Re capsule. The sample was heated to 700 °C at 7 GPa for 24 hours. Further experimental details and calibrations can be found in Keppler and Frost (2005).

3.2.2 Specimen characterization

The recovered samples were analyzed using the scanning electron microscope (SEM) (Figure 3.2.2.1) and employing electron back-scattered diffraction (EBSD) (Figure 3.2.2.2). No preferential orientation was observed with EBSD, the grain size was 1 μm ($\sigma = 0.8$), and the samples were free of cracks, in agreement with optical observations. The chemical composition was determined using a JEOL electron microprobe and was estimated as $\text{CaAl}_2\text{Si}_2\text{O}_7(\text{OH})_2 \cdot (\text{H}_2\text{O})$. The samples were homogeneous in composition. The density of each specimen was determined by Archimedes' immersion method and found to be $3.04(1) \text{ g}\cdot\text{cm}^{-3}$, which is 1.5 % below the ideal density.

As mentioned in §2.2.3, optimum specimens for acoustic experiments should have a length-to-diameter ratio (l/d) of < 0.5 to avoid boundary reflections and for a clear observation of the compressional arrival. The diameter-to-wavelength (d/λ) ratio should be > 3 , to minimize dispersion of the compressional signal, and the wavelength (λ) of the acoustic signal should be > 3 times the diameter (a) of the grains within the sample aggregate, in order to avoid scattering at grain boundaries (Liebermann *et al.*, 1975). The two lawsonite specimens used in this study met these conditions as they had $l = 1.153$ and 1.41 mm and $d = 3.0$ and 3.2 mm and $a \leq 10 \mu\text{m}$. As frequency (f_p) = 10 - 70 MHz and since $\lambda = V_p/f_p$ ($V_p \sim 8.15 \text{ km}\cdot\text{s}^{-1}$), λ varied from 0.116 to 0.272 mm which is $\gg 3a$.

Both ends of each cylindrical specimen were ground and polished flat and parallel using diamond paste of 6, 3 and 1 μm in succession, the final finish being accomplished by 1/4 μm diamond paste. The dense Al_2O_3 buffer rod was also polished using the same procedure.

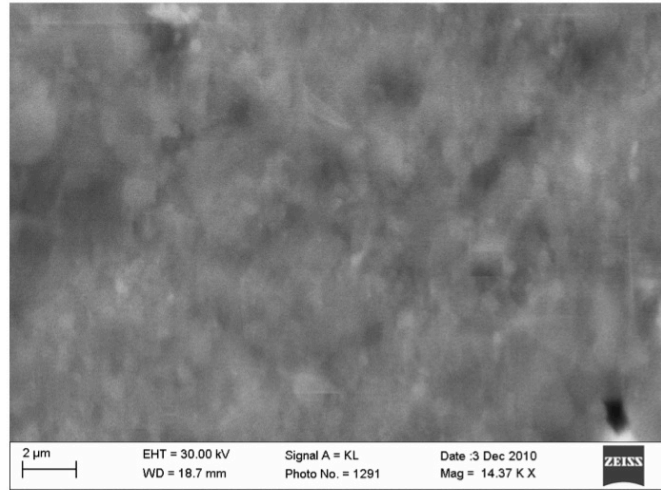


Figure 3.2.2.1: SEM image of the lawsonite sample showing the homogeneous texture, grain size and the absence of porosity.

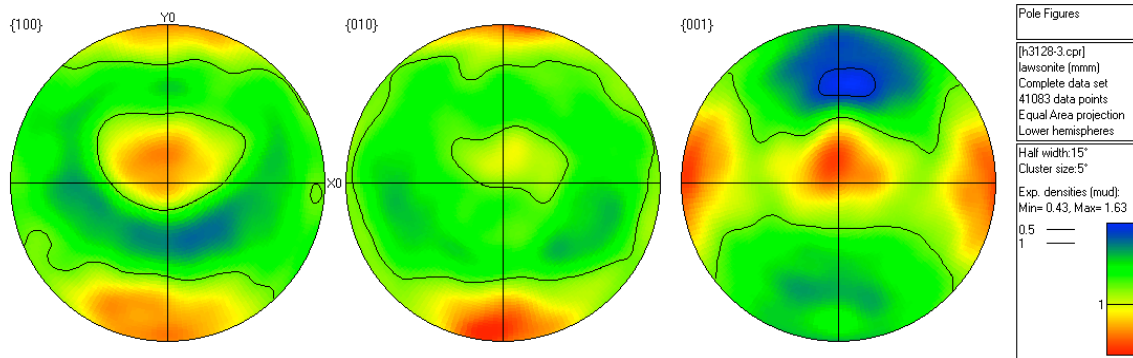


Figure 3.2.2b: Projections of the preferential orientations of the lawsonite polycrystalline sample obtained by EBSD analysis showing no preferential orientation of the crystals.

3.2.3 Velocity measurements at high pressure

Both V_P and V_S as functions of pressure were obtained to 8 GPa in a single compression experiment (# H3152). The S- wave velocities were later re-confirmed in a second run (# H3218). Measurements were performed in a 1000-ton uniaxial split-sphere multi-anvil apparatus (Hymag 1000-ton, Bayerisches Geoinstitut). The cell assembly (**Figure 3.2.3**) for the high-pressure ultrasonic experiments was based on the 18/11

configuration. In order to provide a pseudo-hydrostatic pressure environment, and prevent the sample from cracking, the specimen was backed by a disk of AgCl on the bottom and surrounded by a sleeve of BN.

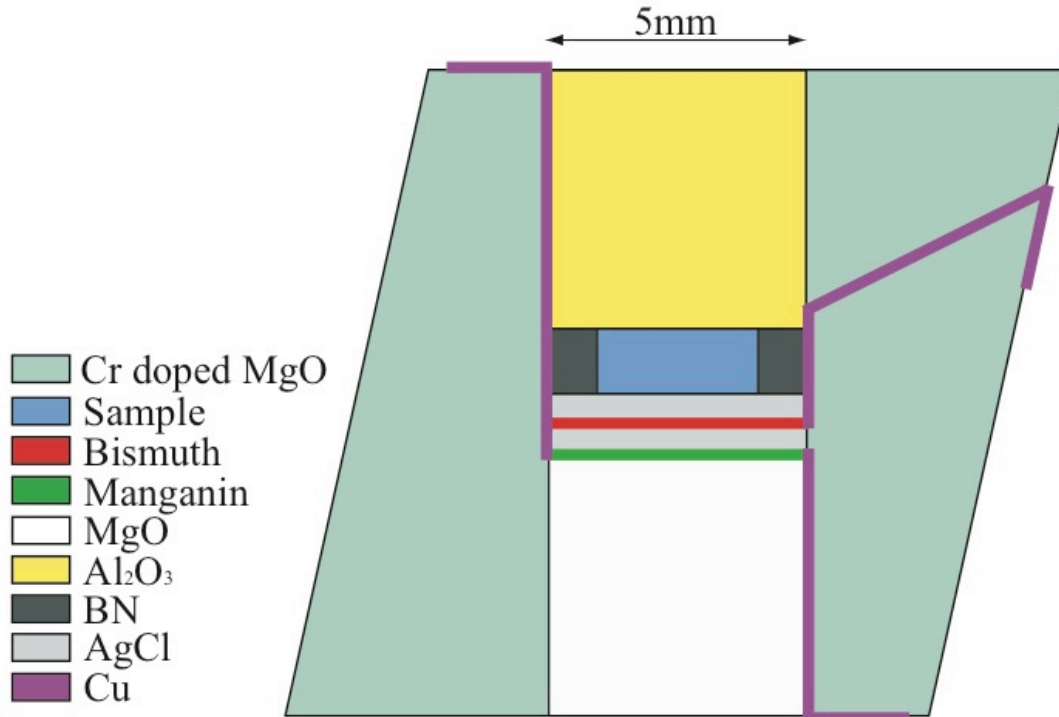


Figure 3.2.3: Schematic diagram of the cell assembly used in the high-pressure ultrasonic interferometry experiments. Specimen was inserted in a cylindrical BN sleeve. Wires of Bi and Manganin were inserted into the AgCl parts to act as pressure markers (see text below).

The pressure of each experiment was calibrated using a combination of the electrical resistance of a Manganin alloy wire as a function of increasing pressure and the fixed-point changes in resistance resulting from phase transformations in Bi [Bi I-II at 2.55 GPa, Bi II-III at 2.70 GPa and Bi III-IV at 7.70 GPa] (Keppler and Frost, 2005). The resistance of Manganin wire varies as a function of pressure but the proportionality constant is calibrated in each experiment using the Bi fix point transitions. The uncertainty in determining the pressure from the electrical resistance of Manganin is estimated to be 0.2 GPa.

The LiNbO₃ dual-mode piezoelectric transducer was rigidly mounted with heated crystal bond, on a stress free corner of one of the WC cubes, diagonally opposing the truncation in contact with the octahedra. A dense Al₂O₃ cylindrical buffer rod acoustically coupled the WC cube and the sample. Thin gold foils (2 μm) were placed at each interface to enhance mechanical bonding: between the specimen and the bottom of the Al₂O₃ buffer rod and between the top of the Al₂O₃ buffer rod and the polished end of the WC cube. Excellent acoustic echoes with a very high signal to noise ratio were maintained throughout the runs.

The round trip travel times of the acoustic compressional and shear waves were measured by ultrasonic phase comparison interferometry. Details of the method have been reported previously (Li *et al.*, 1998; Niesler and Jackson, 1989; Rigden *et al.*, 1988; Rigden *et al.*, 1992) and in §2.3.1. The observation that one is able to transmit a high frequency signal through these specimens coherently is evidence for the high acoustic quality of the sample because high frequency waves are scattered and attenuated by microcracks and porosity in polycrystals. The high signal-to-noise ratio of the buffer rod and sample echoes and the complete absence of any spurious echoes, such as those from side-wall reflections, also allows for precise measurement of travel times of the acoustic waves through the sample. A power amplifier (+12 dB) was also used to increase the amplitude of the reflected pulses and strengthen the signal-to-noise ratio. Analysis of the minima data from the interference pattern yields the travel time as a function of carrier frequency for both *P* and *S* waves. The average round trip travel time of the acoustic *P* and *S* waves through each sample was calculated respectively from the 40 - 55 MHz and 10 - 25 MHz regions, because no dispersion is observed, after correction for the effect of the bond between the sample and the buffer rod as described in previous experimental studies (Jackson *et al.*, 1981; Niesler and Jackson, 1989).

Velocities were calculated from the high-pressure travel times with consideration of the specimen length changes under compression using the self-consistent method of Cook (1957), in which the *P* and *S* wave travel times (t_P and t_S), pressure (*P*) under which the travel times were taken and the length of the specimen (*l*) are related by the following equation:

$$\frac{l_0}{l} = 1 + \frac{1}{3h_0} \int_0^P \frac{dP}{\left[\left(\frac{1}{t_P^2} \right) - \left(\frac{4}{3t_S^2} \right) \right]} \quad (3.2.3.1)$$

where

$$h_0 = 4l_0^2\rho_0 \quad (3.2.3.2)$$

and l_0 and ρ_0 are the ambient pressure sample length and density respectively. The density of the specimen under high pressure was calculated from the corrected length data via the equation:

$$(l_0/l)^3 = (\rho/\rho_0) \quad (3.2.3.3)$$

3.3 Results

The V_P and V_S values for lawsonite, obtained from high-pressure ultrasonic interferometry measurements are reported in **Table 3.3.1**. The velocity trends when extrapolated to room pressure are consistent with velocities determined by Brillouin spectroscopy at ambient conditions (Sinogeikin *et al.*, 2000a). Since the samples were sufficiently long (1.1-1.4 mm), the bond corrections in the travel times for both the P and S waves, taking into account the gold foil at each interface, are generally less than 0.5 ns, resulting in uncertainty of 0.1% for V_P and V_S . The V_S were consistently reproduced in two different experiments.

K and G , respectively of 124.5(4) and 52.5(8) GPa at ambient pressure, were calculated from our ultrasonic interferometry data and are in excellent agreement with the previous static compression studies, $K = 124.1$ (18) GPa (Daniel *et al.*, 1999), and Brillouin measurements $G = 52$ GPa (Sinogeikin *et al.*, 2000a), at 298 K. K and G increase monotonically with pressure with a pressure derivative of $K' = (\delta K / \delta P) = 3.8(1)$ and $G' = (\delta G / \delta P) = 0.6(2)$ (**Figure 3.3**). The K' of 3.8 is in good agreement with K' fixed at 4.0 (Daniel *et al.*, 1999) and slightly lower than K' of 5.5 (2) (Boffa Balaran and Angel, 2003). The value of G' of 0.6 is low compared to most mantle silicates, including talc

(Mainprice *et al.*, 2008), which have G' values generally in the range 1-2. Our measurement of G' for lawsonite is one of the first experimental determinations for a hydrous mantle mineral. This low value of G' has important implications for the LVL, as discussed later.

P (GPa)	ρ (g.cm ⁻³)	V_p (km.s ⁻¹)	V_s (km.s ⁻¹)	K (GPa)	G (GPa)	$\partial K/\partial P$	$\partial G/\partial P$
0.5 ^a	3.05	8.03	4.16	126.4	52.8	3.8	0.6
1.2 ^a	3.07		4.16		53.2		
1.8 ^a	3.08	8.15	4.17	132.6	53.6		
3.2 ^a	3.11		4.18		54.4		
4 ^a	3.13	8.28	4.19	140.1	55.0		
5.3 ^a	3.16		4.20		55.7		
6.3 ^a	3.18	8.44	4.21	149.3	56.3		
8.1 ^a	3.21	8.54	4.22	155.4	57.3		
0* ^b	3.09	7.93	4.08	125.3	51.8		
0* ^c	3.09	7.94	4.12	125.1	52.3		

* room pressures; ^a: this study; ^b: Sinogeikin et al. (2000a); ^c: Schilling et al. (2003).

Table 3.3.1: Ultrasonic interferometry data collected at various pressures.

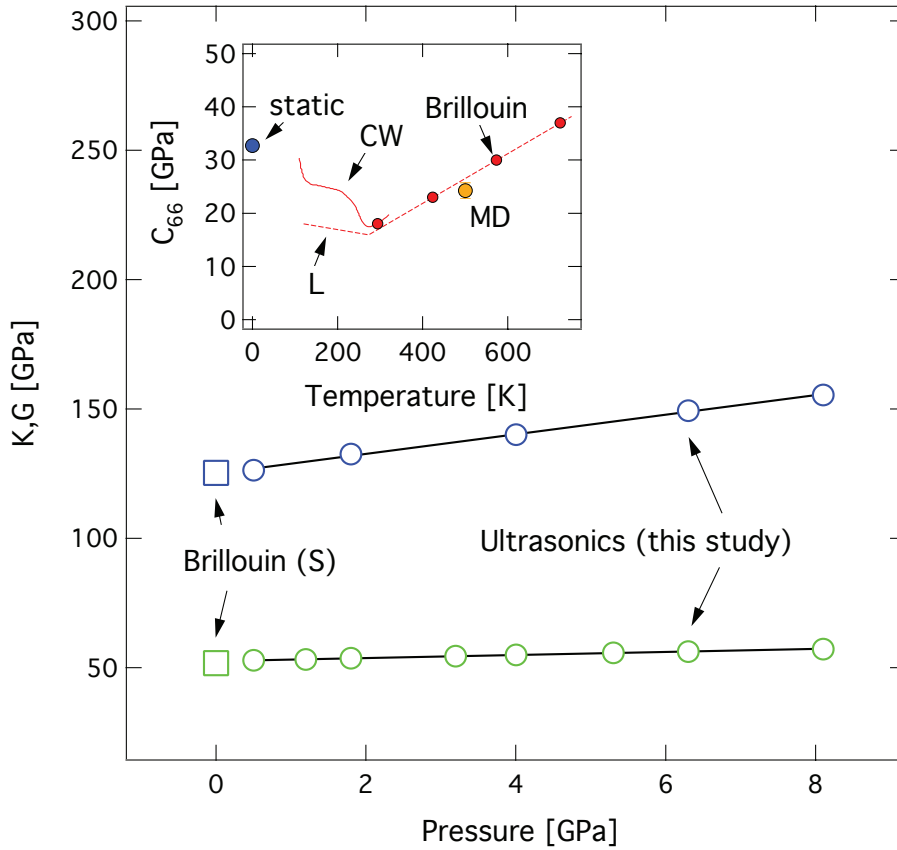


Figure 3.3: *K* and *G* vs. pressure; circles represent the ultrasonic measurements from this study and the squares represent Brillouin spectroscopy measurement (Sinogeikin et al. 2000a); inset shows the temperature dependence of the shear elastic constant, C_{66} vs. temperature from Brillouin spectroscopy (red filled circles, Schilling et al. 2003), static calculations (blue filled circle: this study), Landau theory (dashed lines), molecular dynamics simulation (orange filled circle: this study).

3.4 Discussion

3.4.1 High temperature and pressure model

As lawsonite is stable within eclogitic assemblages to depths of up to ~250 km, its presence can potentially explain some LVL inferences at depths >90 km made through seismic observations (Abers, 2000). The anomalously low value determined for the

pressure derivative of the lawsonite shear modulus, G' , which in turn results from pressure invariance of the elastic constant C_{66} , is important in this respect as it results in low values for V_S at higher pressure (Chantel *et al.*, 2012a). However, as room pressure Brillouin measurements have shown, G increases anomalously with temperature (Schilling *et al.*, 2003), which most likely results from softening of C_{66} with decreasing temperature as a low temperature structural phase transition is approached (Libowitzky and Armbruster, 1995; Sondergeld *et al.*, 2005). Two transitions have been observed in lawsonite, from the room temperature structure $Cmcm$, the first occurs at 270 K to $Pmcn$ and the second at 125 K to $P2_1cn$. These transitions have been related to the orientation of the water molecule within the lawsonite structure and associated changes in the hydrogen bonding (Chantel *et al.*, 2012a). A plausible explanation for the low G' for lawsonite determined is that the temperature of the underlying structural transition is increasing moderately with pressure, causing a softening influence on C_{66} (Chantel *et al.*, 2012a). However K_S is not affected by the softening of C_{66} .

In order to calculate the effects of lawsonite on slab velocities some account has to be taken for the effects of temperature on wave velocities. This can be achieved by fitting the available experimental data for lawsonite to an equation of state that can be extrapolated into regions of P and T where experimental data are lacking. The recent thermodynamic model described by Stixrude and Lithgow-Bertelloni (2005), based on the strain derivatives of the Helmholtz free energy, provides a suitable framework for such a calculation. In this self-consistent model the thermal contribution to the free energy is described by a Debye-Grüneisen approximation and a 3rd order Birch-Murnaghan equation of state is used to describe cold compression (Birch, 1978). The parameters required to model the elasticity of each mineral or mineral component can be obtained by fitting various types of experimental data. The resulting P-V-T- V_S - V_P equation of state depends at room temperature on the bulk and shear modulus and their pressure derivatives, which can be determined for lawsonite from the results of this study, and at high temperature on θ , the Debye temperature, γ_0 the Grüneisen parameter, q_0 the logarithmic volume derivative of γ , and η_{s0} the shear strain derivative of γ . The acoustic Debye temperature for lawsonite can be determined as 710 K using Brillouin data (Sinogeikin *et al.*, 2000a) and γ_0 and q_0 are determined to be 1.06 and 2.1 respectively,

fitted to volume and velocity measurements (Chinnery *et al.*, 2000; Pawley *et al.*, 1996; Schilling *et al.*, 2003). G determinations of Schilling *et al.* (2003) on lawsonite can be refitted by allowing η_{s0} to vary as a function of temperature i.e.

$$\eta_{s0} = -11.649 + 0.0084T(K) \quad (3.4.1.1)$$

Molecular dynamic simulations can also be incorporated into this model to account for the effect of temperature on G at high pressure. The simulations indicate that at high pressure the anomalous positive temperature dependence of G decreases slightly and, accordingly, a further expression for η_{s0} was also derived that includes a pressure term i.e.

$$\eta_{s0} = -11.649 + 0.0084T(K) + 0.357P(GPa) \quad (3.4.1.2)$$

This expression reproduces the molecular dynamics results at high P and T as well as ambient pressure Brillouin measurements. Although empirical, the expression provides an estimation for the effect on the velocities resulting from changes in the lawsonite shear modulus dependence with T and P .

3.4.2 Low velocity layers and the presence of lawsonite

Using the previously described model, seismic wave velocities for a lawsonite bearing eclogite can be calculated at subduction zone conditions and compared with velocities determined for anhydrous eclogite and peridotite rocks at similar conditions. In this way the effectiveness of lawsonite in lowering velocities and creating a LVL can be assessed.

Figure 3.4.2 (and **Table 3.4.2**) show calculations of V_P and V_S for an anhydrous eclogite and peridotite, determined along a subduction geotherm employing the model of Stixrude and Lithgow-Bertelloni (2005) to determine mineral and mineral component elastic properties. Rock properties were calculated using the Reuss-Voigt-Hill approximation (Stixrude and Lithgow-Bertelloni, 2005). Peridotite and eclogite rock compositions and mineral component proportions were taken from the auxiliary online database file of Hacker and Abers (2004). All elastic properties, except those for lawsonite, which are described above, are taken from the tabulations of Stixrude and Lithgow-Bertelloni, (2005). The mineral and mineral component proportions in the rock

are assumed to be constant over the P and T range of the calculations. As the same assumption is made when velocities for a lawsonite bearing eclogite are determined, this simplification should not influence the change in velocity determined between dry and hydrated rocks. The calculated velocities for anhydrous peridotite and eclogite are in good agreement with previous estimates (Bascou *et al.*, 2001; Bezacier *et al.*, 2010; Christensen, 1972; Connolly and Kerrick, 2002; Helffrich and Stein, 1993; Pera *et al.*, 2003). The subduction geotherm used in the calculation was taken from the upper boundary of the NE Japan subduction zone calculated by Peacock and Wang (1999). This particular geotherm has been shown to traverse the lawsonite stability field and is consistent with field evidence for the formation of lawsonite-eclogites (Tsujimori *et al.*, 2006).

In **Figure 3.4.2** the room temperature lawsonite experimental measurements and high temperature, high-pressure molecular dynamics simulation results are shown (Chantel *et al.* 2012a). In addition, the calculations for monomineralic lawsonite along the subduction geotherm and for an eclogite containing 20 vol% lawsonite are also shown in **Figure 3.4.2**. This proportion of lawsonite is the maximum amount that can form in eclogitic rocks i.e. at H_2O saturation (Connolly and Kerrick, 2002; Hacker and Abers, 2004). The entire rock would contain approximately 2 wt% H_2O . By employing a fully hydrated eclogite composition the maximum plausible drop in velocity, i.e. LVL, the probability that lawsonite can produce in an eclogitic rock can be assessed. This amount of lawsonite can potentially form as a result of an H_2O influx from dehydration of hydrous phases such as talc and serpentine in layers below the eclogitic layer (Connolly and Kerrick, 2002). H_2O -rich fluids, formed by dehydration reactions at higher pressures, may also travel up dip within the crustal layer and produce lawsonite. For smaller degrees of hydration the lawsonite-eclogite velocities would move towards those of anhydrous eclogite in **Figure 3.4.2**. The maximum proportion of lawsonite that can form in an eclogitic rock will also depend to some extent on the Ca/Al ratio of the rock.

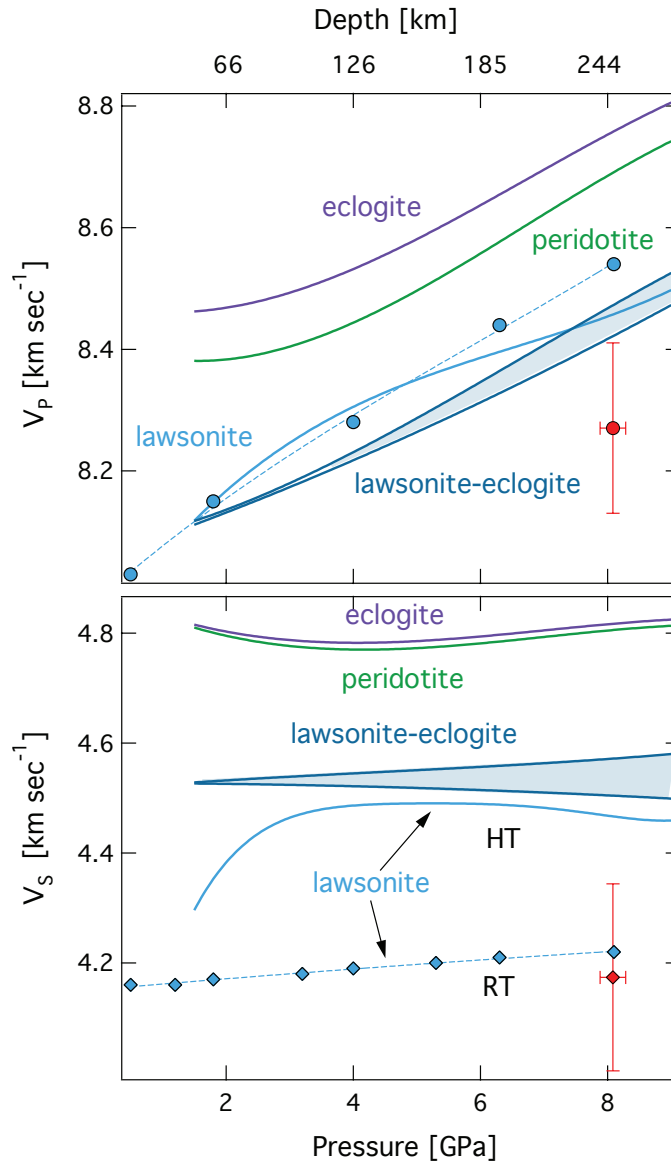
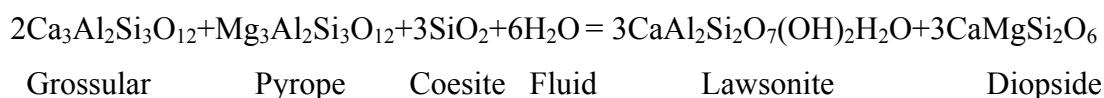


Figure 3.4.2: (a) V_p and (b) V_s variations with pressure (depth shown in the top axis) for peridotite, eclogite and lawsonite eclogite rocks calculated at conditions of a subduction geotherm by employing the model of Stixrude and Lithgow-Berteloni (2005) with parameters for lawsonite determined in from this study (see text for details). The ultrasonic experimental data on lawsonite at room temperature (RT) are also shown (blue circles and diamonds) in addition to the extrapolation of these data to temperatures corresponding to a subduction geotherm (light blue curve). Lawsonite velocities determined from molecular dynamics simulations at 1000 K and 8.1 (\pm 0.2) GPa are shown by red diamonds. The lower bound of the shaded lawsonite eclogite region incorporates these molecular dynamic results into the velocity calculation.

Depth km	Pressure GPa	Temperature		Peridotite		Eclogite		Lawsonite-eclogite		Lawsonite (HighT)	
		$^{\circ}\text{C}$	K	V_p (km.s $^{-1}$)	V_s (km.s $^{-1}$)	V_p (km.s $^{-1}$)	V_s (km.s $^{-1}$)	V_p (km.s $^{-1}$)	V_s (km.s $^{-1}$)	V_p (km.s $^{-1}$)	V_s (km.s $^{-1}$)
51	1.5	200	523	8.384	4.812	8.465	4.817	8.118	4.527	8.111	4.296
66	2	300	593	8.382	4.794	8.467	4.802	8.137	4.534	8.175	4.382
96	3	450	673	8.397	4.772	8.487	4.783	8.176	4.538	8.251	4.465
126	4	520	773	8.45	4.774	8.537	4.786	8.234	4.546	8.303	4.485
155	5	600	853	8.496	4.772	8.581	4.785	8.285	4.548	8.343	4.491
185	6	640	913	8.56	4.783	8.639	4.795	8.348	4.557	8.385	4.489
215	7	680	953	8.622	4.793	8.695	4.805	8.408	4.565	8.424	4.482
244	8	725	998	8.68	4.801	8.749	4.813	8.464	4.57	8.456	4.468
274	9	750	1023	8.745	4.815	8.808	4.826	8.527	4.58	8.495	4.459

Table 3.4.2: The seismic velocities have been determined using the finite strain thermoelastic models (Sixtrude and Berteloni 2005) for individual minerals that constitute peridotite, eclogite and lawsonite-eclogite along a subduction zone temperature and depth profile.

The mineralogy of the lawsonite-eclogite rock was determined from the eclogite rock mineralogy of Hacker and Abers (2004) by adding 20 vol% lawsonite (Connolly and Kerrick, 2002) at the expense of coesite and grossular and pyrope garnet components. Lawsonite was added through the following reaction stoichiometry, in line with the experimental observations of Schmidt and Poli (1998) and Okamoto and Maruyama (1999),



In addition to lawsonite, the rock then comprises 18 vol % garnet, 57 vol % cpx and 4 vol % quartz/coesite. Determinations for V_P and V_S of lawsonite-eclogite are very close to estimates for monomineralic lawsonite at the same conditions. This is because the formation of lawsonite also reduces the proportion of garnet in the rock, which has the highest V_P and V_S . The removal of garnet plays an equally important role in lowering the eclogite velocities as the addition of lawsonite does.

At temperatures above the employed geotherm the proportion of lawsonite will reduce continuously, rendering the eclogite lawsonite-free at temperatures ~200 °C higher (Connolly and Kerrick, 2002). The proportion of lawsonite will also start to continuously decrease at pressures above approximately 7 GPa (Okamoto and Maruyama, 1999). As will be seen, lawsonite contents of the order of 20 vol % would be required within the subducting eclogite layer to render seismic velocities close to those proposed by many LVL seismic estimates. This, therefore, puts tight constraints on the conditions at which lawsonite might cause a LVL and requires that large amounts of lawsonite form through hydration by in-coming fluids during subduction.

The extent to which fully hydrated lawsonite-eclogite can produce a LVL can be assessed by comparing the velocities for this rock with those expected for the overlying mantle, that is, an anhydrous peridotite. Between 1.5 GPa and 8 GPa this velocity difference is relatively constant and approximately 2 % for V_P and 5 % for V_S . The lawsonite-eclogite velocities are relatively temperature insensitive and the velocity difference remains similar at temperatures lower than the geotherm. At temperatures 200 °C higher than the geotherm lawsonite would breakdown completely and velocities would revert to essentially, those corresponding to anhydrous eclogite. In this analysis it is assumed that the temperature of the overlying

mantle is the same as the lawsonite-eclogite. However there are likely to be strong thermal gradients at the slab mantle interface and, depending on the seismic technique employed, the effective overlying mantle temperature may be higher. If overlying mantle temperatures are for example 200 °C higher, this reduces the velocity contrast at the slab interface by approximately 1% in V_S and V_P velocities.

Inferences for the presence of a LVL have been made with a number of seismic techniques. They indicate different velocity contrasts in several subduction zones to various depths (Abers, 2000; Gubbins *et al.*, 1994; Helffrich and Abers, 1997; Matsuzawa *et al.*, 1986; Nakajima *et al.*, 2009). At depths < 90 km several other hydrous phases, including glaucophane, may render low slab velocities in addition to the possibility that basaltic rocks may remain metastable. The presence of lawsonite has, therefore, been proposed mainly to explain the existence of LVLs that extend to depths greater than this (Connolly and Kerrick, 2002). The estimated velocity perturbation of 2 and 5% for V_P and V_S due to lawsonite-eclogite made in our study are at the lower end of many seismic LVL estimates, which are generally in the range 3-10 % for V_P and V_S (Abers and Sarker, 1996; Abers, 2000; Gubbins *et al.*, 1994; Helffrich and Stein, 1993; Helffrich and Abers, 1997; Lin *et al.*, 1999; Matsuzawa *et al.*, 1986). However, there are a number of instances where velocities calculated for lawsonite-eclogite match seismic estimates very well. The study of Abers and Sarker (1996) beneath Alaska, for example, proposes a LVL to 150 km depth with velocity perturbations of 1.5 – 4 % and 3 - 6 % for P and S respectively. The tomographic study of Nakajima *et al.* (2009) identified a LVL extending to 150 km beneath the Kanto district of Japan where S velocities were 5 - 10 % below the overlying mantle but the corresponding P wave anomaly was much weaker, which is again in good agreement with a lawsonite-eclogite origin for the LVL.

Lawsonite-eclogite, therefore, provides a plausible explanation for some LVL seismic estimates at depths greater than 100 km. Levels of lawsonite formed in the slab would have to be close to H₂O saturated levels for the drop in velocity to be sufficiently large to explain many LVL occurrences. This would require H₂O rich fluids originating from dehydration elsewhere in the slab to hydrate eclogite in the subducting crustal layer as it passes through the lawsonite stability field. Seismic observations might, therefore, be used to place constraints on the H₂O content of the subducting crust at depths where an LVL is observed, as such zones would need to contain ~ 2 weight % H₂O. In addition, as lawsonite will ultimately breakdown at

depths above 200 km to release fluids and, or, melts, experimentally determined H₂O contents of nominally anhydrous minerals in the mantle at the conditions of dehydration can be used to place constraints on the likely proportion of H₂O subducted into the deeper mantle. In addition to its potential involvement in LVL formation, lawsonite formation has the potential to influence the velocity of subducting slabs, partly by virtue of its formation at the expense of garnet, and should not, therefore, be neglected in calculations of slab velocities.

4. Sound velocities of garnets with MORB and pyrolite compositions in the transition zone.

4.1 Introduction

Chemical heterogeneities in the mantle are developed through the subduction of basaltic oceanic crust and variably basalt-depleted sub-oceanic lithosphere (Christensen and Hofmann, 1994). Due to the extremely slow rates of cation diffusion, the only viable mechanism for the homogenisation of such heterogeneities is through mechanical mixing which is likely an inefficient process even on the time scales of the age of the Earth. As such it is quite likely that the mantle is a mixture of recycled material on a range of length scales and that at any specific depth the mantle comprises different lithologies. Seismic velocities may therefore reflect the average velocities arising from this mixture of different mineral assemblages (Xu *et al.*, 2008). In addition, it is possible that through the stagnation of subducting material, as a result of reduced density contrast or differences in viscosity, chemically distinct material may accumulate at specific depths in the mantle. The transition zone has, in particular, been proposed as a region where such stagnation may occur as a result of buoyancy-driven resistance to subducting slabs entering the lower mantle (Bina and Kawakatsu, 2010).

In terms of transition zone mineralogy one of the main differences between rocks formed from subducted basaltic crust (Mid Ocean Ridge Basalt: MORB is used here and after to signify composition rather than mineralogy) and typical ultramafic mantle (peridotite or pyrolite) will be the proportion and chemistry of the mineral garnet. MORB rocks are enriched in Ca, Fe and Na, in addition to other minor and trace elements, through the melting process. Both MORB and peridotite composition rocks will contain garnet at pressures above 3 GPa. However, at pressures above 5 GPa substitution of Mg, Fe and Si into the octahedrally coordinated Al site of garnet will lead to the breakdown of pyroxene minerals in both rock types. This substitution can be understood with reference to the majorite end member component, which has

pyroxene stoichiometry. With increasing pressure the proportion of pyroxene minerals in both MORB and peridotite composition rocks will decrease as the majorite component increases, such that by transition zone pressures both rock types may be pyroxene free. MORB rocks contain a higher proportion of garnet compared to peridotite and in the transition zone, depending on the exact whole rock composition, can be composed of monomineralic majoritic garnet (Ringwood, 1967; Irifune and Ringwood, 1987). As a result of the larger proportion of pyroxene minerals in peridotite rocks, however, peridotite transition zone garnets are richer in the majorite component at transition zone conditions (Akaogi and Akimoto, 1997; Irifune, 1987).

The general structural formula for garnets can be written as $A_3B_2Si_3O_{12}$ where A and B represent atoms in dodecahedral and octahedral sites, respectively, and the Si is tetrahedrally coordinated. Solid solutions occur involving both the A and B sites. Pyrope ($Mg_3Al_2Si_3O_{12}$; Py) forms several solid solutions over a wide compositional range: with majorite garnet ($Mg_4Si_4O_{12}$; Mj) by substituting Si and Mg cations for Al in the garnet structure, with almandine ($Fe_3Al_2Si_3O_{12}$; Alm) by substituting Fe cations for Mg, with grossular ($Ca_3Al_2Si_3O_{12}$; Grs) by substituting Ca cations for Mg.

Garnets will be present in the mantle between approximately 2 and 27 GPa (60-700 km depth) and will, in particular, be abundant in the transition zone. As a result of varying chemical composition in the upper mantle and transition zone, garnets will be complex solid solutions containing varying proportions of the different end members. Other than magnesium silicate perovskite no other major mantle mineral is likely to be as chemically complex. Due to the predominance of garnet, the ability to model its elastic properties to determine S and P wave velocities is of prime importance.

There have been several studies to investigate the elastic properties of Py and Py–Mj garnets at high P and RT (Gwanmesia *et al.*, 1998; Chen *et al.*, 1999). The high temperature elasticity of polycrystalline $Py_{50}Mj_{50}$ and $Mj_{80}Py_{20}$, and single crystal pyrope (Py_{100}) has been investigated to 800°C at room pressure by Brillouin scattering (Sinogeikin and Bass, 2000b). Gwanmesia *et al.* (2006) have measured the elasticity of Py_{100} to 9 GPa and 1000°C, and Murakami *et al.* (2008) performed simultaneous high-pressure, high-temperature ultrasonic elasticity measurements for a Fe-bearing majoritic garnet. Irifune *et al.* (2008) reported the sound wave velocities of majorite with a ‘pyrolite minus olivine’ composition towards conditions of the mantle transition region (up to 18 GPa and 1500K). The ‘pyrolite minus olivine’

composition is the residual pyroxene + garnet component of pyrolite obtained by subtracting 62 wt% olivine (Fo₈₈) from the pyrolite composition.

In order to calculate the elastic properties of a realistic mantle solid solution most models use a formulism whereby the elastic modulus of the complex mineral is derived through a summation of the individual elastic moduli of the end members. Such an equation normally makes the summation as a function of volume or density fraction i.e.

$$\psi_{ss} = \frac{1}{\sum_{i=1}^n \frac{1}{m_i V_i} \sum_{i=1}^n \frac{m_i V_i}{\Psi_i}} \quad (4.1)$$

where ψ_{ss} is the bulk elastic property, ψ_i is the elastic modulus of component i and V_i and M_i are the volume and mole fraction of component i . While such a summation is not physically justified it cannot take account of the possibility of non-ideal behaviour i.e. where the properties of a solution deviate from those derived from a summation of the end member properties. Almost all silicate solid solutions display some non-ideal properties. Excess volumes of mixing are well known for many solid solutions and particularly for garnet solid solutions (Newton and Wood, 1980; Ganguly *et al.*, 1996). Further deviations from ideality can occur when more than two components are present. It would seem however that no study has specifically addressed the possibility that measureable excess properties may exist in elastic moduli. For garnet, for example, such a summation assumes that the effect on the elastic moduli of adding Grs to Py is proportionately the same as adding Grs to Mj. Although this may be reasonable, no studies have been specifically designed to test the applicability of equation 4.1.

In this study the elastic properties of complex garnet solid solutions containing 4 components, which have compositions specifically relevant to heterogeneities in the transition zone, are determined using ultrasonic acoustic velocity measurements in the multianvil press at high pressure. In addition properties of simply binary solid solution garnets are determined in an internally consistent manner. The compositions investigated are the pyrope end-member (Py), simple solid solutions: pyrope-majorite (Py₆₂Mj₃₈, Py₅₀Mj₅₀), pyrope-almandine (Py₉₀Alm₁₀, Py₈₀Alm₂₀) and pyrope-grossular

(Py₈₀Grs₂₀), and finally two complex compositions: garnets at transition zone conditions with compositions expected (Aoki and Takahashi, 2004, Irifune *et al.*, 2008) for subducted basaltic material (Gt_{MORB}: Py_{0.182}Alm_{0.123}Grs_{0.170}Mj_{0.525}) and typical ultramafic mantle, peridotite (Gt_{PyR}: Py_{0.176}Alm_{0.016}Grs_{0.068}Mj_{0.740}), with the MORB garnet being richer in Fe and Ca and depleted in majoritic component. Using the simple binary data end member garnet properties are evaluated and these data are used to test the accuracy of equation 4.1 in predicting the elasticity of the two complex garnet solid solutions. This procedure should indicate if excess elastic properties are significant in garnet solid solutions. These data are also used to discuss implications for the seismic velocity gradients in the transition zone.

4.2 Experimental procedures

4.2.1 Garnets synthesis, hot pressing and characterization

The starting materials were synthesized from chemical reagents, MgO, SiO₂, Fe₂O₃, Al₂O₃ and CaCO₃, mixed to yield the correct mineral compositions. Glasses were produced by melting the anhydrous mixtures at 1600°C for 1 hour, followed by grinding to fine powders. The recovered powders were then remelted and quenched once more to glass and the procedure repeated. The starting materials were then transformed to hot-pressed polycrystalline garnet aggregates in multi-anvil experiments.

The specimens used in this study were synthesized at the Bayerisches Geoinstitut, in the 1000 tons uniaxial split sphere apparatus, Hymag 1000, in runs H3065 (Py), H3071 (Py₉₀Alm₁₀), H3087 (Py₈₀Alm₂₀) and H3209 (Py₈₀Grs₂₀), at conditions of about 5 GPa and 1350°C for 2 hours. The other samples were hot pressed in the 5000 tons uniaxial split sphere multi-anvil, Voggenreiter Zwick 5000, Z718 (Py₅₀Mj₅₀), Z722 (Py₆₂Mj₃₈), Z761 (Gt_{MORB}) and Z768 (Gt_{PyR}) at conditions of about 14 GPa and 1400 °C for 2 hours.

The powders were encapsulated in capsules composed of 25 μm thick Re foil that were 2 mm in diameter and 3 mm long. Experiments were performed using a 18 mm octahedral pressure medium with 11 mm WC cube truncations, employing a

LaCrO₃ heater. The samples were separated from the heater by MgO spacers. Temperature within the cell was monitored by a W3%Re and W25%Re thermocouple inserted axially and in direct contact with the Re capsule. Further experimental details and calibrations can be found in Keppler and Frost (2005).

The recovered samples were characterized using the scanning electron microscope (SEM) and electron back scattered diffraction (EBSD). No preferential orientation was observed with EBSD. The grain size was 2-10 μm, and the samples were free of cracks. The chemical composition was determined using a JEOL electron microprobe and was found to be as dictated by the stoichiometry. The samples were homogeneous in composition. The density of each specimen was determined by Archimedes' immersion method and reported in **Table 4.1**. Both ends of each cylindrical specimen and the Al₂O₃ buffer rod were ground and polished flat and parallel using diamond pastes of 6, 3, 1 and ¼ μm in succession.

Electron microprobe analyses of recovered pyrolite and MORB composition garnets yielded the formulas (Mg_{2.03}Fe_{0.19}Ca_{0.78})(Al_{0.52}Si_{0.74}Mg_{0.74})Si₃O₁₂ and (Mg_{1.15}Fe_{0.78}Ca_{1.07})(Al_{0.95}Si_{0.525}Mg_{0.525})Si₃O₁₂ respectively which equated to the 4 garnet en members yields (Py_{0.176}Alm_{0.016}Grs_{0.068}Mj_{0.740}) and (Py_{0.182}Alm_{0.123}Grs_{0.170}Mj_{0.525}) (**Table 2.1**).

Gt _{pyr}	Al ₂ O ₃	SiO ₂	CaO	FeO	MgO	Total
Average	20.29	44.45	9.18	2.89	23.42	100.23
σ	0.12	0.62	0.08	0.05	0.2	0.64
Gt _{MORB}						
Average	19.68	43.04	12.21	11.39	13.73	100.05
σ	0.18	0.42	0.11	0.13	0.18	0.43

Table 2.1: Electron microprobe analysis of the pyrolite and MORB compositions garnets (reported in wt%).

4.2.2 Velocity measurements at high pressure

Both P- and S- wave velocities as functions of pressure were obtained up to 16 GPa. Measurements were performed in the 5000-tonne uniaxial split-sphere

multianvil apparatus (Zwick 5000-ton) at the Bayerisches Geoinstitut, Bayreuth, Germany. The cell assembly for the high-pressure ultrasonic experiments was based on the 18/11 configuration (edge length of MgO octahedron = 18 mm; truncated edge length on tungsten carbide cubes = 11 mm) (Chantel *et al.*, 2012a). In order to provide a pseudo hydrostatic pressure environment, and avoid sample cracking, the specimen was surrounded by a sleeve of boron nitride (BN) and supported by a disk of AgCl at the base.

The pressure of each experiment was calibrated using a combination of the electrical resistance of a Manganin alloy wire as a function of increasing pressure and the phase transformations in Bi (Bi I-II at 2.55 GPa, Bi II-III at 2.70 GPa and Bi III-IV at 7.70 GPa) (Lloyd, 1971) and associated discontinuities in resistance. The resistance of Manganin wire varies as a function of pressure but the proportionality constant is calibrated in each experiment using the phase transitions in Bi. The uncertainty in the pressure is estimated to be 0.2 GPa.

The LiNbO₃ dual-mode piezoelectric transducer was rigidly mounted with crystal bond, on a stress free corner of one of the tungsten carbide (WC) cubes, diagonally opposing the truncation in contact with the octahedron. A dense Al₂O₃ cylindrical buffer rod acoustically connected the WC cube and the sample. Thin gold foils (2 μm) were placed at each interface: between the specimen and the bottom of the Al₂O₃ buffer rod, and between the top of the Al₂O₃ buffer rod and the polished end of the WC cube, to enhance mechanical bonding. Excellent acoustic echoes were maintained throughout the runs.

The round trip travel times of the acoustic compressional and shear waves were measured by ultrasonic phase comparison interferometry. Details of the method have been reported previously (Li *et al.*, 1998; Niesler and Jackson, 1989; Rigden *et al.*, 1988; Rigden *et al.*, 1992). Velocities were calculated from the high-pressure travel times by accounting for the specimen length changes under compression using the self-consistent method of Cook (1957). In this method, the P and S wave travel times (t_P and t_S), pressure (P) under which the travel times were collected and the length of the specimen (l) are related by the following equation:

$$\frac{l_0}{l} = 1 + \frac{1}{3h_0} \int_0^P \frac{dP}{\left[\left(\frac{1}{t_p^2} \right) - \left(\frac{4}{3t_s^2} \right) \right]} \quad (4.2.2.1)$$

where, $h_0 = 4l_0^2\rho_0$; l_0 refers to the sample length; ρ_0 refers to the sample density, the subscript “0” refers to the ambient pressure condition. Sample densities were determined at room pressure using literature data on sample volumes. Volumes for solid solutions and complex garnet compositions were determined using linear combinations of end member volumes from the literature (Xu *et al.*, 2008) uncertainties in the volume of 0.5% correlate to velocity uncertainties of 1%. The densities of the specimens under high pressure were calculated from the corrected length data via the equation:

$$(l_0/l)^3 = (\rho/\rho_0). \quad (4.2.2.2)$$

In addition, a further experiment was performed on member pyrope garnet at the beamline ID06, ESRF, Grenoble, France, employing simultaneous ultrasonic and x-ray measurements up to 10.3 GPa. Using in situ radiography the length of the sample could be measured, rather than having to assume an elastic shortening as in the Cook method, (equation 4.2.2.1). X-ray diffraction patterns of the sample were collected at each pressure while the length of the experimental sample was measured using an image plate detector MAR 345. X-ray diffraction data were also collected simultaneously from an MgO pressure marker placed in the center of the assembly. From these data and using the well-establish equation of state of MgO (Zha *et al.*, 2000), the pressure could be determined.

4.3 Results

4.3.1 Ultrasonic measurements

Travel times were measured between room pressure and 16 GPa on samples of pyrope (Py), pyrope-almandine solid solutions (Py₉₀Alm₁₀), (Py₈₀Alm₂₀), pyrope-grossular solid solution (Py₈₀Grs₂₀), pyrope-majorite solid solutions (Py₅₀Mj₅₀), (Py₆₂Mj₃₈), and multicomponent MORB (Gt_{MORB}) and transition zone pyrope garnets

(Gt_{Pyr}). **Table 4.3.1** and **Figure 4.3.1.1** summarize the aggregate sound wave velocities and density of the garnets obtained in this study. For all the specimens the thin bonds employed (2 μm) meant that travel times bond corrections for both P and S waves were generally less than 5 ns, taking part of the overall uncertainties of 1% for both P- and S- waves velocities. The P and S wave velocities along with densities of the aggregates were calculated using the Cook's method employing room pressure densities determined from chemical compositions of each individual sample using literature data on molar volumes (Xu *et al.*, 2008).

As can be seen in **Figure 4.3.1** determined velocities for garnet solid solutions increase uniformly with pressure. Only at room pressure do some velocities appear anomalous, likely due to poor contact or initial sample porosity. Compared to pyrope the addition of almandine and majorite components lowers velocities while the grossular component raises them. Likely due to high almandine and majorite components, the multi component transition zone MORB and pyrolite garnets display the lowest velocities.

Figure 4.3.1.2 shows the results of measurements on pyrope samples performed both at the BGI using the Cook method (equation 4.2.2.1), compared with measurements performed at the ESRF using in situ methods to determine both the sample length and the pressure. The velocity profiles obtained are identical within the uncertainties. The Cook's method should be reliable for data collected at room temperature as little plastic deformation can occur at these conditions such that sample lengths should be responding only in an elastic manner, as assumed by the method. Changes in sample length due to brittle behaviour would anyway result in loss of the ultrasonic signal.

	Py			Py**			Py ₉₀ Alm ₁₀		
P (GPa)	V_P	V_S	ρ	P (GPa)	V_P	V_S	V_P	V_S	ρ
RP*	9.00	5.10	3.565	2	9.12	5.14	9.02	5.09	3.639
2.55	9.15	5.15	3.619	3.8	9.22	5.16	9.07	5.10	3.694
5	9.28	5.18	3.669	4.8	9.27	5.18	9.20	5.13	3.744
7.7	9.42	5.22	3.719	6.2	9.35	5.20	9.34	5.17	3.800
10	9.54	5.25	3.764	7.8	9.43	5.22	9.46	5.20	3.842
12	9.63	5.28	3.800	9.4	9.51	5.24	9.55	5.22	3.878
14	9.73	5.30	3.836	10.3	9.55	5.25	9.64	5.25	3.915
16	9.82	5.32	3.869				9.73	5.27	3.949
	Py ₈₀ Alm ₂₀			Py ₈₀ Grs ₂₀			Py ₅₀ Mj ₅₀		
P (GPa)	V_P	V_S	ρ	V_P	V_S	ρ	V_P	V_S	ρ
RP*	8.94	5.04	3.716	9.13	5.20	3.573	8.91	4.96	3.539
2.55	8.99	5.05	3.769	9.19	5.22	3.626	9.01	4.99	3.593
5	9.12	5.09	3.823	9.32	5.25	3.678	9.15	5.04	3.645
7.7	9.26	5.12	3.876	9.45	5.29	3.727	9.29	5.08	3.695
10	9.38	5.15	3.919	9.56	5.31	3.772	9.41	5.12	3.739
12	9.47	5.17	3.960	9.65	5.33	3.810	9.50	5.14	3.778
14	9.56	5.19	3.993	9.74	5.35	3.846	9.60	5.17	3.814
16	9.65	5.21	4.031	9.82	5.37	3.882	9.69	5.20	3.847
	Py ₆₂ Mj ₃₈			Gt _{MORB}			Gt _{pyr}		
P(GPa)	V_P	V_S	ρ	V_P	V_S	ρ	V_P	V_S	ρ
RP*	8.95	5.00	3.545	8.79	4.94	3.635	8.80	4.89	3.540
2.55	9.04	5.03	3.599	8.94	4.98	3.692	8.95	4.94	3.596
5	9.18	5.07	3.648	9.07	5.02	3.741	9.08	4.98	3.644
7.7	9.32	5.11	3.702	9.21	5.06	3.798	9.23	5.03	3.701
10	9.44	5.15	3.746	9.32	5.09	3.840	9.34	5.07	3.742
12	9.53	5.18	3.782	9.41	5.12	3.879	9.44	5.10	3.780
14	9.63	5.20	3.818	9.50	5.14	3.915	9.53	5.12	3.815
16	9.72	5.23	3.854	9.58	5.17	3.951	9.62	5.15	3.851

*RP stands for room pressure.

**Measurements performed at the ESRF in conjunction with x-rays.

Table 4.3.1: *Experimental conditions and the results for the investigated garnets.*

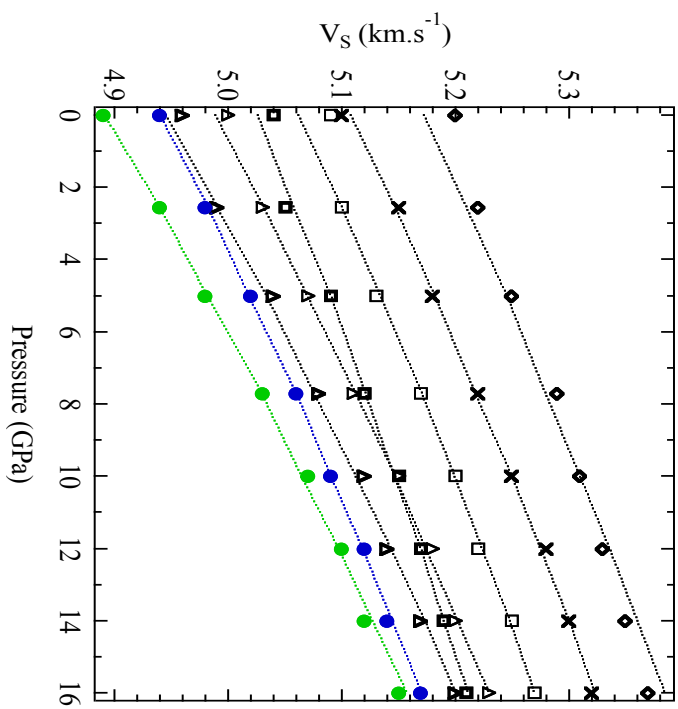
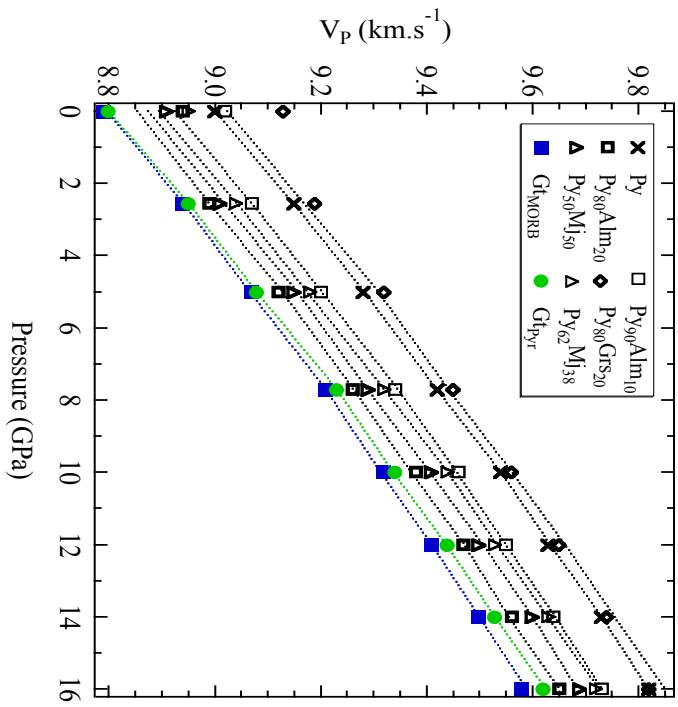


Figure 4.3.1.1: S- and P-wave velocities and density changes of the investigated samples with pressure. Symbols stand for the experimental data points and lines for the fit from thermo-elastic models.

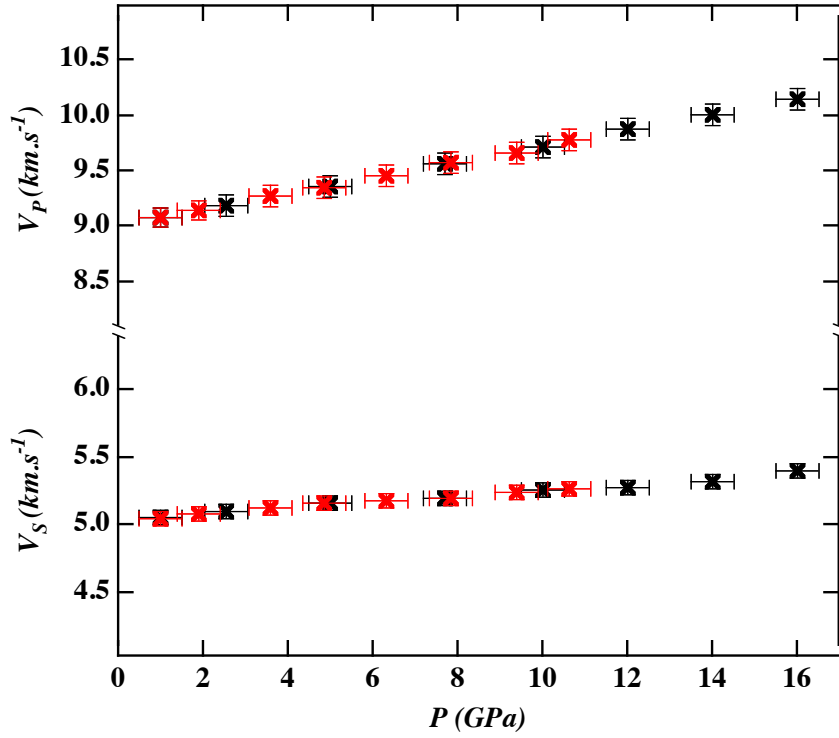


Figure 4.3.1.2: Compressional and shear wave velocities for pyrope, measured at BGI (black crosses) compared with those determined at the ESRF (red crosses) using in situ radiographic sample length measurements and pressure calibration using in situ x-ray diffraction of an MgO pressure standard.

4.3.2 Data fitting

Room temperature and pressure elastic properties were extracted from the density (ρ) and compressional (V_p) and shear (V_s) velocity data employing 3rd order finite strain equations (Davies and Dziewonski, 1975):

$$\rho V_p^2 = (1 - 2\varepsilon)^{5/2} (L_1 + L_2 \varepsilon) \quad (4.3.2.1)$$

$$\rho V_s^2 = (1 - 2\varepsilon)^{5/2} (M_1 + M_2 \varepsilon) \quad (4.3.2.2)$$

where $\varepsilon = 0.5 \left[1 - (\rho/\rho_0)^{2/3} \right]$. By fitting the L and M fitting coefficients, the zero pressure adiabatic shear modulus, $G = M_1$, and bulk modulus, $K_S = L_1 - \frac{4}{3}G$, and the respective pressure derivatives, $G' = \frac{1}{3}(5M_1 - M_2)/K_0$ and $K' = \frac{1}{3}(5L_1 - L_2)/K_0 - \frac{4}{3}G'$,

can be determined. To check internal consistency the pressure can then also be calculated from:

$$P = -(1 - 2\varepsilon)^{5/2} (C_1\varepsilon + 0.5C_2\varepsilon^2) \quad (4.3.2.3)$$

where $C_1=3L_1-4M_1$ and $C_2=3L_2-4M_2+7C_1$.

Least squares fitting of equations 4.3.2.1 and 4.3.2.2 to the experiments on pyrope and all the solid solutions presented in the **Table 4.3.1** yields the values given in **Table 4.3.2**. For the studied garnets, values refined for K_S , K_S' , G and G' are in reasonable agreement with previous studies (Sinogeikin and Bass, 2000b; Jiang *et al.*, 2004, Kono *et al.*, 2010; Sinogeikin and Bass, 2002; Liu *et al.*, 2000; Wang *et al.*, 1993; Irifune *et al.*, 2008; Murakami *et al.*, 2008). As shown in **Table 4.3.2** pyrope properties determined at BGI and at ESRF are identical within uncertainties, but the bulk modulus is slightly lower than observed in previous studies, (Sinogeikin and Bass, 2000b; Chen *et al.*, 1999) although once the uncertainties are considered the disagreement is only 2 GPa.

4.3.3 Refinement of elastic properties for the garnet end members almandine, grossular and majorite

Using equations 4.3.2.1 and 4.3.2.2, the room temperature moduli and pressure derivatives for the garnet end members other than pyrope (Alm, Grs and Mj) were extracted from the velocities measured for the binary solid solutions in this study. To do this the velocity data from the binary garnet solid solutions were refitted as a function of pressure where the velocity at each condition was calculated from a summation of properties for the two end members in the correct molar proportions. Data for the almandine end member, for example, were fitted using the experimental velocity data for the Py₉₀Alm₁₀ and Py₈₀Alm₂₀ solid solutions and the end member pyrope properties determined for the ESRF pyrope sample given in **Table 4.3.2**. In detail the least squares refinement was performed using the cold portion (not considering the temperature) of the self-consistent model described by Stixrude and Lithgow-Bertelloni (2005). This model employs a 3rd order Eulerian finite strain equation for the room temperature properties. At each condition the bulk modulus and

Samples	K_S	dK_S/dP	G	dG/dP	References
Py	165(2)	4.0(2)	93(1)	1.1(1)	This study
Py**	164(2)	4.2(2)	94(1)	1.0(1)	
Py ₉₀ Alm ₁₀	165(2)	4.1(2)	93(1)	1.1(1)	
Py ₈₀ Alm ₂₀	166(2)	4.1(2)	94(1)	1.1(1)	
Py ₈₀ Grs ₂₀	164(2)	4.1(2)	96(1)	1.1(1)	
Py ₅₀ Mj ₅₀	163(2)	3.8(2)	87(1)	1.2(1)	
Py ₆₂ Mj ₃₈	163(2)	4.0(2)	88(1)	1.2(1)	
Gt _{MORB}	163(2)	3.9(2)	89(1)	1.1(1)	
Gt _{Pyr}	161(2)	3.8(2)	85(1)	1.2(1)	
Alm	172(2)	4.1(2)	96(1)	1.5(1)	This study
Grs	163(2)	3.2(2)	109(1)	1.2(1)	
Mj	160(2)	3.8(2)	81(1)	1.3(1)	
Py	171(3)	4.1(3)	94(2)	1.3(2)	Sinogeikin and Bass(2000b)
Py	171(2)	5.3(4)	92(1)	2.0(1)	Chen et al.(1999)
Alm	174(2)	4.9(2)	96(1)	1.4(1)	Jiang et al.(2004)
Grs	171.5(1)	4.42(2)	108.4(4)	1.27(1)	Kono et al.(2010)
Py ₅₀ Mj ₅₀	167(3)	4.2(3)	90(2)	1.4(2)	Sinogeikin and Bass(2002)
Py ₅₀ Mj ₅₀	170(5)	6.4(5)	89(1)	2.1(1)	Liu et al.(2000)
Py ₆₂ Mj ₃₈	169(6)	5.3(2)	89(5)	2.0(1)	Rigden et al.(1994)
Py ₆₂ Mj ₃₈	160(3)	4.9(5)			Wang et al.(1993)
Mj	166(3)	4.2(3)	85(2)	1.4(2)	Sinogeikin and Bass(2002)
Mj	167(3)	6.7(4)	88(2)	1.9(1)	Gwanmesia et al.(1998)
Gt _{Pyr} ^a	164.4(5)	4.24(6)	94.9(2)	1.11(3)	Irifune et al. (2008)
Fe-Mj ^b	166(2)	4.2(2)	88.7(7)	1.28(8)	Murakami et al. (2008)

^a majorite with a 'pyrolite minus olivine' composition, ^b iron-bearing majorite.

Table 4.3.2: Obtained elastic parameters of the studied garnets.

modulus and shear modulus at room temperature and the pressure of interest are determined from the room pressure moduli (K_0, G_0) and pressure derivatives (K'_0, G'_0) using the equations (§2.5)

$$K = (1 + 2f)^{\frac{5}{2}} \left[K_0 + (3K_0K'_0 - 5K_0)f + \frac{27}{2}(K_0K'_0 - 4K_0)f^2 \right]$$

(2.5.13)

and

$$G = (1 + 2f)^{\frac{5}{2}} \left[G_0 + (3K_0G'_0 - 5G_0)f + (6K_0G'_0 - 24K_0 - 14G_0)f^2 \right]$$

(2.5.14)

where f is the finite strain defined as $f = \frac{1}{2} [(V_0/V)^{2/3} - 1]$, with V and V_0 being the volume at pressure and room pressure respective. The moduli for the solid solutions are calculated from the two end member properties using equations 4.3.2.1 and 4.3.2.2. These moduli along with the densities are then used to calculate V_s and V_p which are then compared with the experimental values and the sum of the squared residual is then minimised by refining the unknown end member properties i.e, for (Alm, Grs and Mj). Data for these three refined end members are reported in **Table 4.3.2** and can be compared with values from the literature. The values refined for almandine are in very good agreement with those determined by Jiang *et al.* (2004). The bulk modulus refined for grossular, 163(2) is slightly lower than the value obtained by Kono *et al.* (2010) of 171.5 (1) and the pressure derivative is also slightly lower but the shear modulus is in perfect agreement. The refined bulk and shear moduli for majorite are both slightly lower than those reported from previous studies (Sinogeikin and Bass 2002; Gwanmesia *et al.*, 1998), however, these studies examined the tetragonally distorted majorite end member, while that refined from the current data corresponds to a cubic end member as it is extrapolated from cubic garnets with majoritic components.

4.4 Discussion

4.4.1 The calculation of elastic properties for multi component garnets from end members

Although garnet elastic properties have been investigated in a number of studies, no study to date has examined sufficient data through which to refine elastic data for all major garnet end members in an internally consistent manner. Internal consistency is important for determining the effects of varying chemistry because these effects are quite subtle and large differences seem to arise in the literature between studies obtained using different techniques.

Figure 4.4.1 summarises the results of garnet elastic properties at room pressure and 16 GPa. Compared to pyrope, substitution of Fe, Ca and majorite result in shifts in the two moduli in very different directions. Ca raises G but has little effect on K , Fe raises K with little effect on G while the majorite substitution lowers both G and K . Due to the magnitude of the pressure derivatives at 16 GPa, with increasing pressure, the effect of Ca on G increases, the effect of Fe on K decreases but a positive effect on G develops and the effect of the majorite substitution on both moduli decreases.

In this study two multicomponent garnets were also studied with compositions equivalent to those expected for garnets forming within peridotite (pyrolite) and MORB composition mantle in the transition zone. The chemical formulas of the MORB and pyrolite garnets are $(\text{Mg}_{1.15}\text{Fe}_{0.78}\text{Ca}_{1.07})(\text{Al}_{0.95}\text{Si}_{0.525}\text{Mg}_{0.525})\text{Si}_3\text{O}_{12}$ and $(\text{Mg}_{2.03}\text{Fe}_{0.19}\text{Ca}_{0.78})(\text{Al}_{0.52}\text{Si}_{0.74}\text{Mg}_{0.74})\text{Si}_3\text{O}_{12}$ respectively and they contain differing proportions of all 4 garnet end members i.e. $\text{Py}_{0.182}\text{Alm}_{0.123}\text{Grs}_{0.170}\text{Mj}_{0.525}$ for MORB and for pyrolite $\text{Py}_{0.176}\text{Alm}_{0.016}\text{Grs}_{0.068}\text{Mj}_{0.740}$. In **Figure 4.4.1** these 2 compositions are plotted and found to be close to the majorite substitution trend, which dominates their compositions. Using the procedure outlined above and employing equations 4.2.2.1, 3.2.1, 3.2.2 and 3.2.3 the elastic moduli of for these multicomponent garnets have been calculated using the values for the 4 end members determined in this study. These calculated values are shown in **Figure 4.4.1** at both pressures as open circles of the same colour as the equivalent garnet data points. At room pressure the calculated and experimental moduli are in perfect agreement and the data point for the calculated

values is almost obscured in both cases. At 16 GPa the value calculated for the pyrolite composition from the end members is again in excellent agreement with the measured value while the bulk modulus for the MORB value deviates by only 4 GPa. This small deviation for the MORB bulk modulus value at 16 GPa may arise from the refinement of the grossular end member, which has a slightly lower K' than many of the other garnet determinations.

This comparison between the measured elastic properties of a multicomponent garnet composition and those calculated from the end members is an effective test of the use of the equation 4.1 in determining bulk mineral elastic properties. It seems that garnet elastic properties can be determined from the end members with an accuracy that is generally within experimental uncertainties. There seems to be no evidence that large excess properties exist that cause non-linear contributions to multicomponent elastic properties for the mineral garnet.

The comparison with literature data at high pressure is particularly interesting. While discrepancies have been described previously between the elastic moduli determined in this study and literature data at room pressure, at high pressure literature data on majoritic garnets become widely scattered as a result of differences in the determined pressure derivatives. Literature calculations for the bulk modulus of majoritic garnets at 16 GPa deviate by up to 50 GPa while the values determined for the 4 majorite bearing solid solutions in this study keep the same general behaviour relative to each other. In addition several literature majorite values converge with those determined in this study at pressures of 16 GPa, where the data are most relevant.

4.4.2 A comparison with mantle velocity models

The garnet elastic properties determined in this study can be used with additional literature data to estimate seismic velocities for pyrolite and MORB bulk compositions at the base of the transition zone i.e. between 520 and 580km. In this depth range, MORB compositions are almost entirely composed of garnet as the pressure is insufficient for the formation of either Ca or Mg silicate perovskite (Hirose and Fei, 2002). A pyrolitic mantle composition, on the other hand, will contain only two coexisting phases, ringwoodite and majoritic garnet (Irifune, 1987). Over this depth interval the garnet compositions in both MORB i.e.

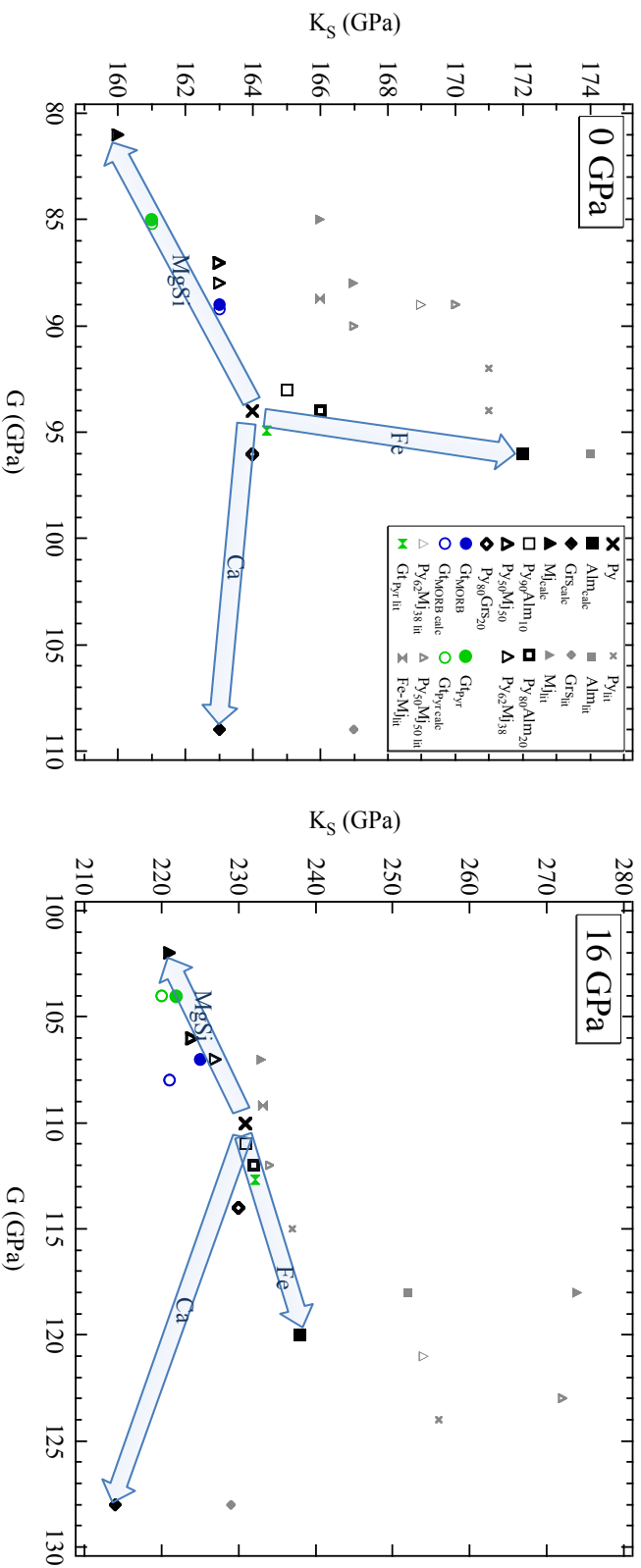


Figure 4.4.1: Shear (G) and Bulk (K_S) moduli of polycrystalline hot pressed garnet aggregates measured up to 16 GPa using ultrasonic interferometry in the multianvil device. The cross marks the determination of pyrope from this study. Large black symbols unfilled symbols are for solid solutions determined in this study. Arrows show directions of major substitutions. The solid blue and green symbols are for the MORB and pyrolic garnet compositions respectively. Open circles of the same color show calculations of these multicomponent garnet properties using the end member determinations. Small grey symbols show literature data while the small green symbol shows the pyrolic minus olivine composition of Irifune et al. (2008).

$(\text{Mg}_{1.15}\text{Fe}_{0.78}\text{Ca}_{1.07})(\text{Al}_{0.95}\text{Si}_{0.525}\text{Mg}_{0.525})\text{Si}_3\text{O}_{12}$ and pyrolite i.e. $(\text{Mg}_{2.03}\text{Fe}_{0.19}\text{Ca}_{0.78})(\text{Al}_{0.52}\text{Si}_{0.74}\text{Mg}_{0.74})\text{Si}_3\text{O}_{12}$ bulk compositions will assume those of the multicomponent garnets examined in this study. In detail the calculation assumes a transition zone region comprising 56 vol% of ringwoodite and 44 vol% of majorite, meaning 78 mole% $(\text{Mg}_{0.9}\text{Fe}_{0.1})_2\text{SiO}_4$ ringwoodite and 22 mole% majoritic garnet (Gt_{Pyr}) for the pyrolite composition and 100 % garnet Gt_{MORB} for the MORB. The calculation is performed along the geotherm of Brown and Shankland (1981).

In this study no data were collected at high temperature, so high temperature elastic properties were estimated using a thermal equation of state and data on thermal parameters taken from the literature. To do this the equation of state model of Stixrude and Lithgow-Bertelloni (2005) was used where in addition to the ambient temperature contribution to the elastic moduli (equations 3.2.1, 3.2.2 and 3.2.3) high temperature terms are added which arise from a Mie-Grüneisen equation of state. A Debye approximation is used to determine the change in the internal energy. In addition to the 4 room-pressure moduli and pressure derivatives, 4 additional thermal terms are required for each phase; θ , the Debye temperature, γ , the Grüneisen parameter, q , the volume dependence of γ , and η , the shear strain derivative of γ . All thermal terms are taken from the refinement reported by Xu *et al.* (2008), **Table 4.4.2**. Equation 4.1 is used to determine bulk mineral moduli and the Voigt-Reuss-Hill average is used to determine the velocities of the aggregate mineral assemblage.

		V_0 ($\text{cm}^3\text{mol}^{-1}$)	K_T (GPa)	K'	G (GPa)	G'	θ (K)	γ	q	η
$\text{Mg}_3\text{Al}_2\text{Si}_3\text{O}_{12}$	Pyrope	11.31	165	4	93	1.1	823	0.8	1.9	1.1
$\text{Fe}_3\text{Al}_2\text{Si}_3\text{O}_{12}$	Almandine	11.54	172	4.1	96	1.5	741	0.8	2.6	2.9
$\text{Ca}_3\text{Al}_2\text{Si}_3\text{O}_{12}$	Grossular	12.51	163	3.2	109	1.2	823	0.8	2.4	1.8
$\text{Mg}_4\text{Si}_4\text{O}_{12}$	Majorite	11.43	160	3.8	81	1.3	835	0.8	2.6	2.4
Mg_2SiO_4	Mg-ringwoodite	3.95	185	4.2	123	1.4	891	1.11	2.4	2.3
Fe_2SiO_4	Fe-ringwoodite	4.19	213	4.2	92	1.4	652	1.26	2.4	1.8

Table 4.4.2: Properties of the main phases at the base of the transition zone.

In **Figure 4.4.2** the calculated velocities for a MORB and pyrolite mantle compositions are compared with the seismic reference models PREM (Dziewonski and Anderson, 1981), AK135 (Kennett *et al.*, 1995) and those of Cammarano *et al.*

(2005). Deviation between the two calculated mantle models is about 3% for both V_P and V_S , with the modelled slab composition being slower. As already proposed by Irifune et al. (2008) both trends, of the pyrolitic and MORB compositions, exhibit similar slopes, which are most importantly of smaller gradient than the seismic reference models PREM and Ak135 in this region of the mantle. The gradients with pressure in the model calculations performed here arise from pressure derivatives of the elastic constants and are not influenced strongly by the thermal properties, such that uncertainties and assumptions made on the thermal properties are not likely to affect this result. This difference may arise due to the inability of seismic models to accurately determine velocity gradients in the transition zone due to the occurrence of discontinuities. The magnitude of the discontinuities refined by the seismic models will be highly correlated with neighbouring velocity gradients.

In the AK135 and PREM models velocities in the Earth are described by a set of polynomial functions that are applied over defined depth intervals, with the assumption that seismic discontinuities occur at certain depths. Both models include infinitesimally sharp discontinuities at approximately 410 and 660 km. However in addition a 3rd transition zone discontinuity is also known to occur at 520 km depth due to the transformation of wadsleyite to ringwoodite. This will cause a sharper increase in the velocities than occurs in the models at this depth. By missing this discontinuity the models are likely forced to compensate by having steeper gradients in this region. No seismic reference model is a unique fit to the global seismic data from which they are refined, due to tradeoffs between the magnitude of the discontinuities and the velocity gradients. In PREM and Ak135, the underlying structure is described by a series of polynomial functions with no theoretical justification. Cammarano et al. (2005) fitted the same global seismic data to models calculated for actual mineral assemblages assuming a particular bulk composition and temperature gradient. The adjustable parameters in the fitting procedure are the mineral elastic properties, which are varied only within the bounds of the experimental uncertainties (**Figure 4.4.2**).

Cammarano et al. (2005) produced a range of velocity profiles that would all be consistent with the global seismic data but which had some underlying mineral physical justification. These models include for example an increased gradient at 520 km due to the wadsleyite ringwoodite phase transition, which is not predicted to form a sharp discontinuity but a steeper gradient. Many of the Cammarano et al. (2005) models are in good agreement with the calculation made here and, in particular, with

the gradient. Within the uncertainties of the seismic data therefore a pyrolite mantle composition is quite consistent with velocities at the base of the transition zone. The presence of stagnant slabs near the base of the mantle transition zone might cause a low-temperature anomaly, which would increase the average velocities in this region. Subducted slabs are known to be composed of a thin layer of oceanic crust on top of a residual harzburgite layer, mainly olivine. The harzburgite with higher olivine content and $Mg/(Mg + Fe)$, relative to the surrounding mantle, should increase the seismic velocities. Both relatively low temperatures and olivine-rich nature of the stagnant slab support that there would seem little grounds to argue that significant accumulation of MORB composition material may occur at the base of the transition zone.

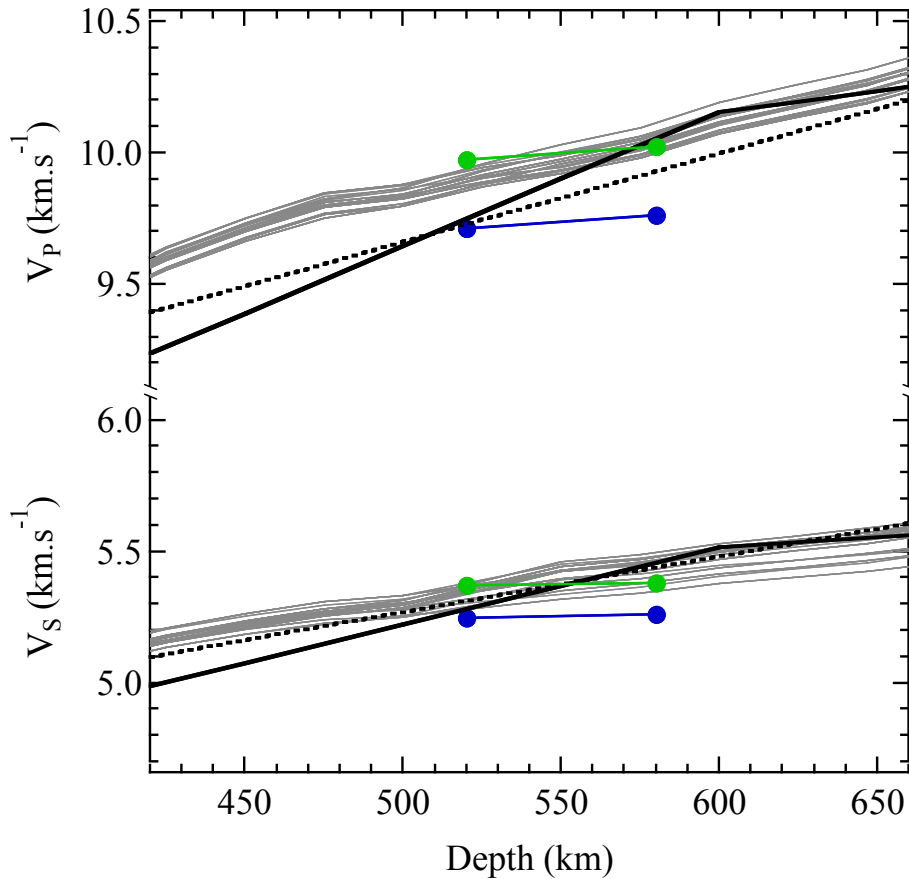


Figure 4.4.2: Estimates for V_s and V_p of a pyrolitic composition and a subducted slab composition, respectively comprising $(Mg_{0.9}Fe_{0.1})_2SiO_4$ ringwoodite and $(Mg_{2.03}Fe_{0.19}Ca_{0.78})(Al_{0.52}Si_{0.93}Mg_{0.55})Si_3O_{12}$ majoritic garnet (Gt_{Pyr}) shown as the solid line between the green dots and only $(Mg_{1.15}Fe_{0.78}Ca_{1.07})(Al_{0.95}Si_{0.80}Mg_{0.25})Si_3O_{12}$ majoritic garnet (Gt_{MORB}) shown as the solid line between the blue dots. Both are calculated at the pressures and temperatures corresponding to the lower mantle depths indicated. Data for the two different majoritic garnets are taken from the equation of state model determined in this study, while models for the other phases are taken from the literature. The solid and dashed black lines show PREM and Ak135 seismic reference models for the transition zone. The numerous reference models by Cammarano et al. (2005), represented by the thin grey lines, were obtained by fitting similar global seismic data to 1-D velocity models calculated for a pyrolite mineral assemblage by adjusting mineral elastic properties within the range of their uncertainties.

5. Sound velocities of aluminum-bearing iron-magnesium silicate perovskite of 25 GPa and 1500K

5.1 Introduction

It has been accepted that the lower mantle is composed of peridotite composition with about 72 mol% (Mg, Fe)(Al, Si)O₃ perovskite and lesser amounts of ferropericlase (22 mol%) plus a small (6 mol%) amount of CaSiO₃ perovskite. The composition of silicate perovskite forming within a typical Bulk Silicate Earth (BSE: primitive mantle, which is the sum of our actual current and crust) composition is dominated by the MgSiO₃ (hereafter referred to as Mg-Pv) component but will also contain sub-equal proportions of Fe and Al, through the coupled substitutions $Mg_A + Si_B = Fe^{3+}_A + Al^{3+}_B$ and $Si_B = Al_B + 0.5\Box$ (where \Box means oxygen vacancy). It is likely that the Fe content of Mg-Pv varies in the lower mantle as a result of the effect of pressure on the partitioning of Fe between Mg-Pv and coexisting ferropericlase (Sinmyo *et al.*, 2008) and possibly due to the presence of chemical heterogeneities that may arise either from subduction of oceanic crust or the presence of primordial material (Christensen and Hofmann, 1994; Kellogg *et al.*, 1996).

The lower mantle is considered to have a Mg/Si ratio identical to that of the upper mantle and equal to 1.3. This value is higher than the Mg/Si < 1.0 of the chondritic meteorite, considered of the composition of the bulk silicate earth (BSE). This depletion of silicon in the lower mantle has been already been addressed in a mineralogical model suggesting a lower mantle enriched in silicon relative to the upper mantle, which is consistent with the BSE model. It also implies layered-mantle convection with limited mass transfer between the upper and lower mantle (Murakami *et al.*, 2012).

The 660 km discontinuity conversion is weaker than global Earth models predict. It has been proposed that it originate either from a significant attenuation below 410 km or regional non-thermal variations in 660 km discontinuity properties

that decrease its velocity and density jumps to 2% ΔV_p (Helffrich *et al.*, 2003; Estabrook and Kind, 1996), whereas the S-wave velocity and density remain unchanged with respect to previous global models. Helffrich *et al.* 2003 explained the low amplitude of the 660 km discontinuity by its broadening, possibly due to the lateral variations in the transition zone water content at this depth. Estabrook and Kind (1996) supported a model of mantle rheology with an increase in the viscosity of the mantle across the 660km to explain the geophysical observations.

In order to interpret one dimensional seismic velocity profiles for the lower mantle it is crucial not only to determine velocities for the major minerals such as Mg-Pv but also to assess the effect of major chemical substitutions on the elasticity. A number of studies have examined the elastic properties of end-member Mg-Pv through compression studies and computer simulations (Boffa Ballaran *et al.*, 2012; Fiquet *et al.*, 2000; Li and Zhang, 2005; Murakami *et al.*, 2007; Sinogeikin *et al.*, 2004; Ross and Hazen, 1990; Vanpeteghem *et al.*, 2006a). However, very few studies have examined the shear elastic properties and only the study of Li and Zhang (2005) has examined these properties at high temperatures, albeit at pressures lower than the Mg-Pv stability field. No studies exist on the shear wave properties of Fe-bearing MgSiO₃ (hereafter referred to as (Mg, Fe)-Pv) and there is some disagreement between studies as to whether Al substitution raises (e.g., Andraut *et al.* 2001) or lowers (e.g., Zhang and Weidner, 1999) the bulk modulus of MgSiO₃ perovskite. Recently Murakami *et al.* (2012) studied properties of Al bearing MgSiO₃ in laser heated diamond anvil cells. Murakami *et al.* (2012) concluded that S wave velocities for a peridotitic lower mantle composition, comprising perovskite and ferropericlasite, would be lower than seismically observed and instead proposed that the lower mantle must be composed predominantly of perovskite.

Ultrasonic interferometry can measure adiabatic elastic properties of minerals in the multianvil press through travel time measurements of P and S-wave velocities. In this study densities and P and S velocities of monomineralic hot-pressed powdered samples of magnesium silicate perovskite were measured at conditions encompassing the upper region of Earth's lower mantle (up to 25 GPa and 1200 K). These properties were examined for the MgSiO₃ end member perovskite (Mg-Pv), a Fe bearing perovskite and two Fe and Al bearing perovskite hereafter referred to as 2%Fe³⁺ and Al, and 4%Fe³⁺ and Al. In this way the influence of the two main chemical variants in the lower mantle on seismic wave velocities was constrained.

5.2 Methods

Polycrystalline samples of perovskite: MgSiO_3 , $(\text{Mg}, \text{Fe})\text{SiO}_3$ with 3.6 wt% of FeO, $(\text{Mg}, \text{Fe})(\text{Si}, \text{Al})\text{SiO}_3$ with 3.8 wt% of FeO and 2 wt % of Al_2O_3 , and $(\text{Mg}, \text{Fe})(\text{Si}, \text{Al})\text{SiO}_3$ with 7.5 wt% of FeO and 4.9 wt % of Al_2O_3 , were prepared from dried reagent grade MgO , SiO_2 , Al_2O_3 and Fe_2O_3 . The oxides were ground together in ethanol in the correct proportions and then each composition was melted in a box furnace at 1873 K and quenched to a glass. The iron-bearing composition was then subsequently reduced in a gas-mixing furnace with a H_2/CO_2 gas mixture at 1000K for 24 hours (-21 log units of $f\text{O}_2$).

Samples were transformed and hot pressed using a multianvil apparatus at 26 GPa and 2,000K. A 10 mm edge length octahedral assembly was employed with 4 mm truncation edge length tungsten carbide cubes (a so called 10/4 assembly). The cell assembly was composed of the Cr-doped MgO pressure medium, inside of which a LaCrO_3 sleeve furnace was used to heat the sample. A ZrO_2 sleeve was used for thermal insulation of the furnace. Finally, a MgO capsule was used to surround the sample, inside the furnace. Temperature was measured with a W_{97}Re_3 – $\text{W}_{75}\text{Re}_{25}$ thermocouple, the hot junction of which was placed near the sample. The recovered samples were about 1 mm long in diameter. The top and bottom surfaces of each sample were analyzed using a scanning electron microscope to determine purity and grain size, which was $<20 \mu\text{m}$. The density of the samples was measured by the Archimedes' method and confirmed that the hot-pressed cylindrical samples consisted of pure perovskite and had almost zero porosity ($>99\%$).

Combined in situ X-ray and ultrasonic measurements were conducted at the 13-ID-D beamline of GSECARS at the Advanced Photon Source, Argonne, IL, using a 1000 ton press and a T-25 multi-anvil module (Wang et al., 2009). A 10/4 assembly was employed with a cylindrical rhenium foil furnace with two opposite, laser-cut, windows to facilitate X-ray transparency. Outer ZrO_2 sleeves thermally insulate the furnace; however in the central region a MgO sleeve replaces ZrO_2 in order to reduce the X-ray absorption. The sample was separated from the furnace using a MgO spacer. One end of the sample was in direct contact with the dense alumina buffer rod used for the ultrasonic measurements, while the opposite end of the sample was backed by a softer $\text{NaCl}+\text{BN}$ mixture (**Figure 5.2.1**). $2 \mu\text{m}$ thick gold foils were

placed at both ends of the sample to enhance bonding and to function as indicators for sample length measurements using X-ray radiographic images (**Figure 5.2.2**).

Throughout the experiment, temperature was monitored with a $W_{97}Re_3-W_{75}Re_{25}$ thermocouple, whose junction was placed near the sample. Uncertainties in temperature measurements due to the gradient in the furnace and fluctuation of heating were, within 2 % of the nominal values. Pressure was monitored using measurements of the unit-cell volumes of NaCl and Au. The equations of state of Anderson et al. (1989) and Decker (1971) were employed. Powder X-ray diffraction data from the sample and the pressure markers were collected using an energy-dispersive system at a diffraction angle of 6.04° . A YAG phosphor was placed in the beam path behind the sample to convert the X-ray absorption contrast of the assembly into visible light. A mirror, tilted at 45° with respect to the incident beam, reflects the image signal into an objective lens. An imaging charge-coupled device (CCD) was used to record images for sample length measurement at high-resolution (1 pixel \sim 2 μ m) (**Figure 5.2.2**).

Ultrasonic measurements were conducted while *in situ* X-ray observations were being made, and the travel times of both V_P and V_S were determined with a Tectronix Digital Oscilloscope using the pulse–echo method at three different frequencies (30, 40 and 50 MHz) (Papadakis, 1990), after correction for the effect of the gold-bond between the sample and the buffer rod as described in previous experimental studies (Jackson et al., 1981; Niesler and Jackson, 1989). Data acquisition time at each pressure and temperature point was typically 5 min. The overall uncertainties of the present velocity measurements are within 0.5 % in both V_P and V_S at room temperature. A major contribution to this uncertainty comes from the determination of the sample length, 0.2 to 0.4%, while the uncertainty of the travel-time is only 0.1%. Temperature uncertainty is estimated to be approximately 8% (due to the uncertainties in the temperature measurements) at 1200 K, which would correspond to an equivalent velocity uncertainty of approximately 0.3% in V_P and 0.5% in V_S at 1200K. At 700 K these additional errors will be approximately half.

After the experiments the samples were mounted in epoxy, then sectioned and polished. Electron microprobe analyses were performed on each sample under operating conditions of 15 nA and 15 kV, with standards consisting of enstatite for Mg, andradite for Si, spinel for Al and Fe metal for Fe concentrations (**Figure 5.2.3**). The samples were found to be chemically homogeneous with all Fe reported as FeO,

which gives the formula MgSiO_3 , $(\text{Mg}_{0.95}, \text{Fe}_{0.05})\text{SiO}_3$, $(\text{Mg}_{0.962}, \text{Fe}_{0.038})(\text{Al}_{0.02}, \text{Si}_{0.98})\text{O}_3$ and $(\text{Mg}_{0.932}, \text{Fe}_{0.075})(\text{Al}_{0.049}, \text{Si}_{0.943})\text{O}_3$. All chemical analyses are reported in **Table 5.2.1**. The $\text{Fe}^{3+}/\Sigma\text{Fe}$ ratio of the Fe-bearing samples was determined using a transmission Mössbauer spectrometer fitted with a point source (McCammon et al., 1991). The sample was thinned to 400 μm , which gave an effective thickness of ~ 5 mg Fe/cm². The spectra were collected for 2 days at room temperature, and the data were fitted to Lorentzian lineshapes using the program MossA (Prescher et al., 2012) (**Figure 5.2.4**). The $\text{Fe}^{3+}/\Sigma\text{Fe}$ ratios were calculated from the relative area ratios to be 0.23 ± 0.05 for (Fe, Mg)-Pv, 0.35 ± 0.05 for 2% Fe^{3+} and Al and 0.51 ± 0.03 for 4% Fe^{3+} and Al.

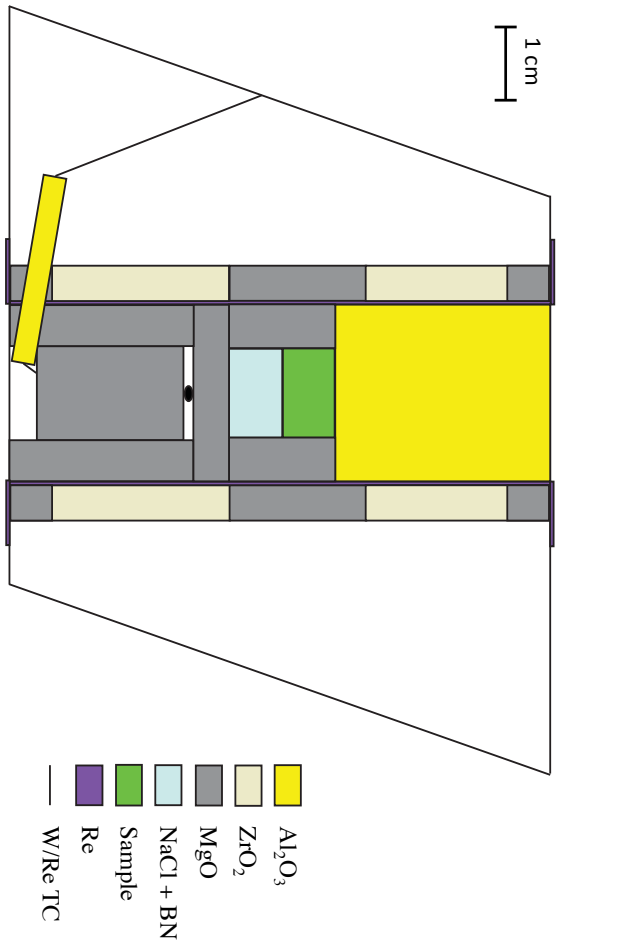
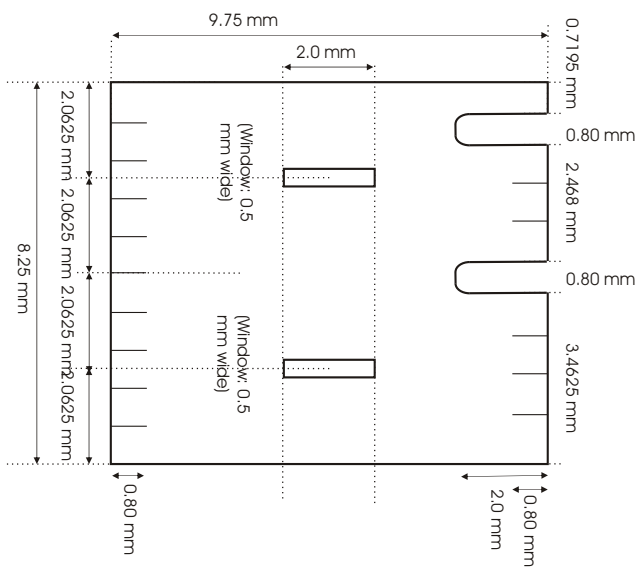


Figure 5.2.1: Design of the cell assembly used for the ultrasonic measurements. Below, is presented the drawing of the laser-cutted rhenium furnace.



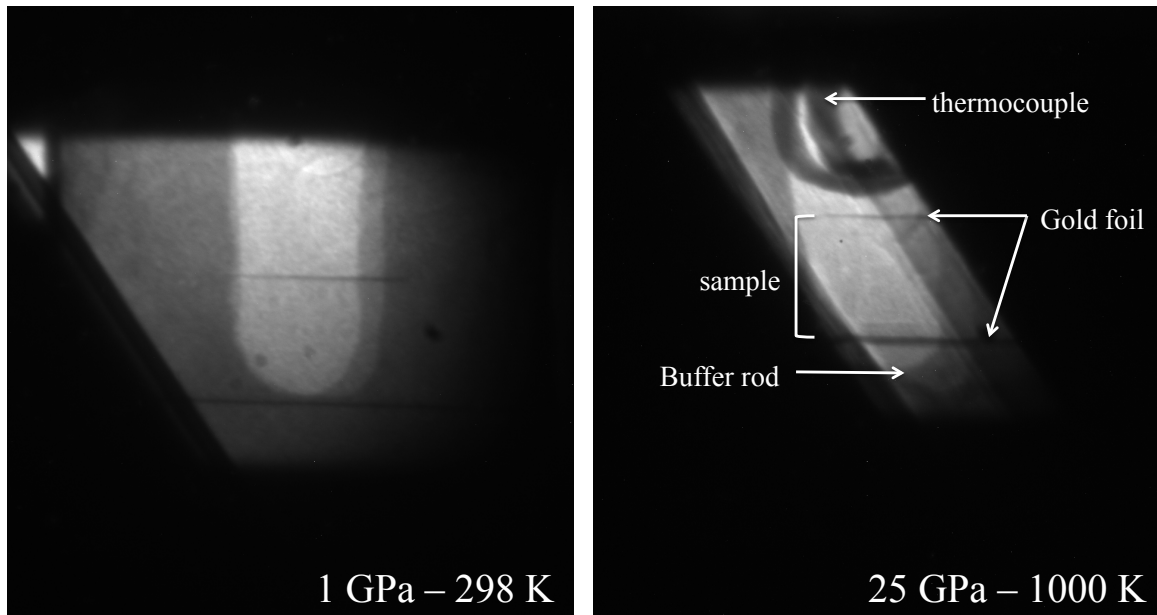
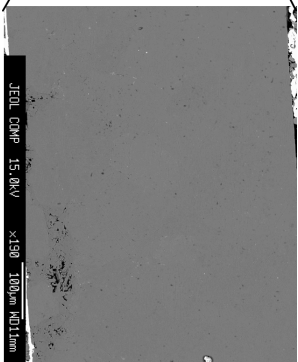
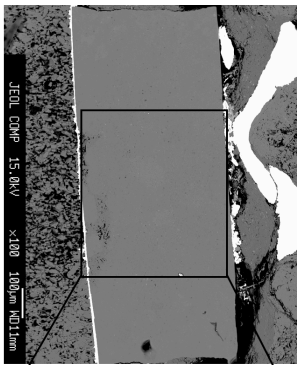
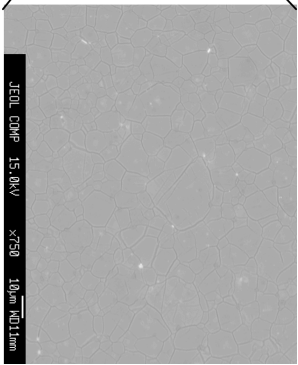


Figure 5.2.2: X-ray radiography of the cell assembly under low and elevated pressure and temperature conditions.

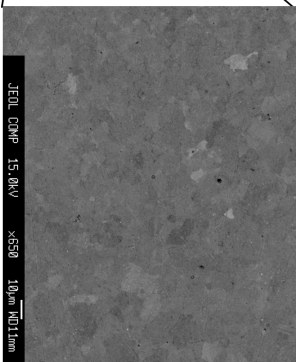
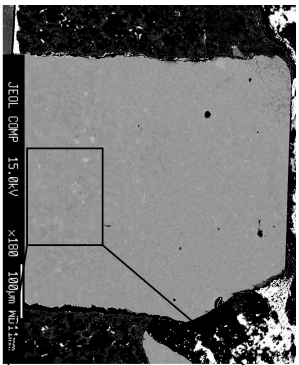
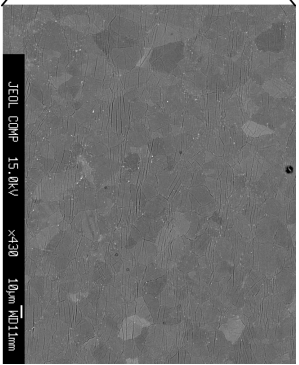
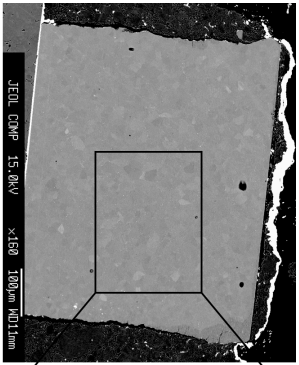
Mg-Pv	SiO ₂	FeO	Al ₂ O ₃	MgO	Total
Average	59.47	0.07	0.35	39.88	99.78
σ	0.66	0.03	0.05	0.46	0.89
(Fe, Mg)-Pv					
Average	58.83	3.48	0.26	37.82	100.39
σ	0.79	0.21	0.06	0.78	1.5
2%Fe ³⁺ and Al					
Average	57.59	2.85	1.29	39.57	101.29
σ	0.64	0.14	0.08	0.52	0.76
4%Fe ³⁺ and Al					
Average	55.28	5.35	2.74	37.53	100.9
σ	0.65	0.23	0.04	0.46	0.69

Table 5.2.1: Electron microprobe analysis of the perovskite samples (reported in wt%).



a: Tl999, Mg-Pv.

b: Tl205, (Fe, Mg)-Pv.



c: Tl282, 2%Fe³⁺ and Al.

d: Tl286, 2%Fe³⁺ and Al.

Figure 5.2.3: Microprobe images of the perovskite samples.

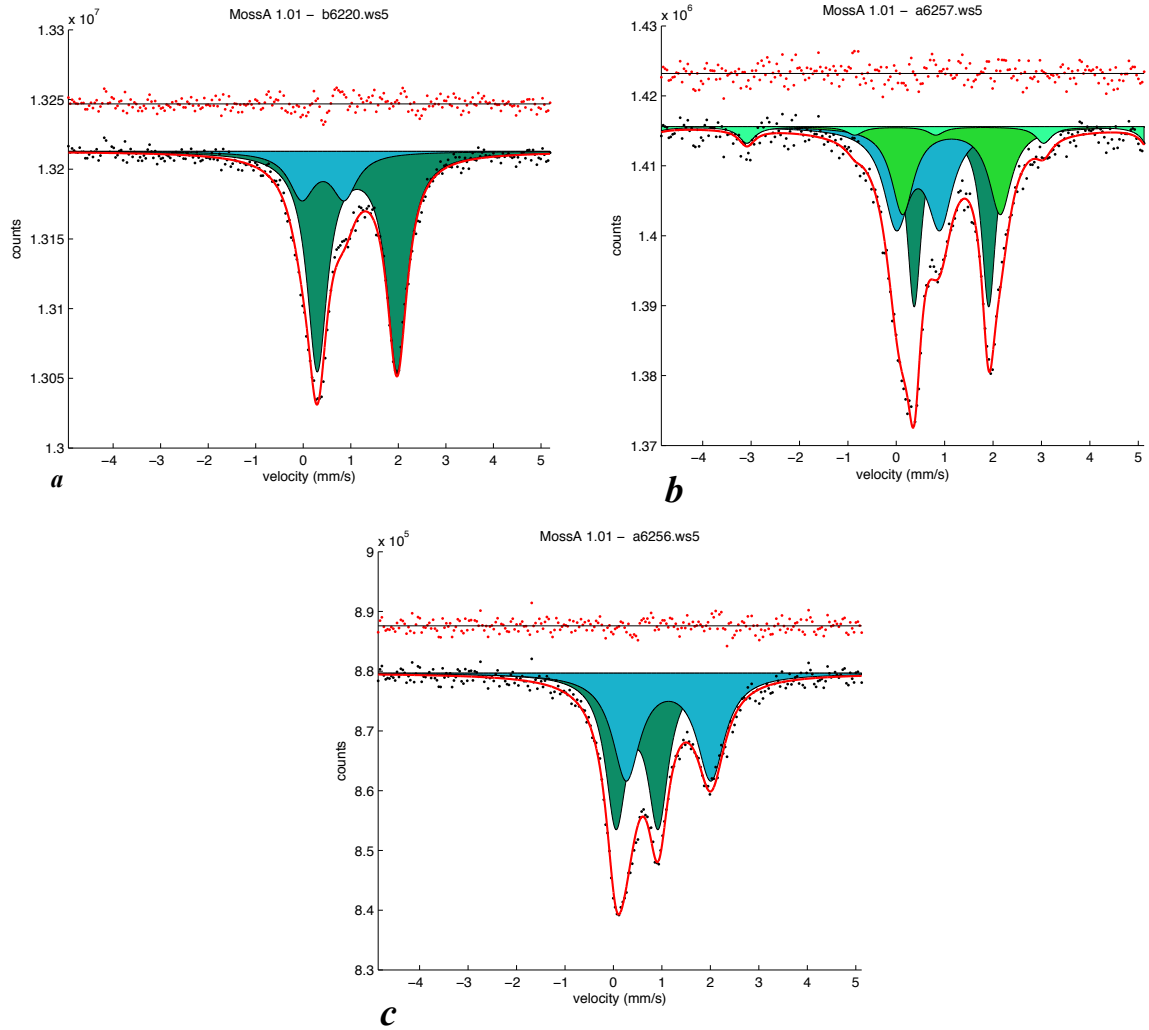


Figure 5.2.4: Mössbauer spectrum of the perovskite samples. **a:** T1205, (Fe, Mg)-Pv, **b:** T1282, 2%Fe³⁺ and Al, **c:** T1286, 4%Fe³⁺ and Al.

5.3 Results and discussion

5.3.1 Effect of the Fe substitution

The chemical formula of the (Mg, Fe)-Pv sample calculated from the electron microprobe analyses combined with the Mössbauer data is $Mg_{0.95}Fe_{0.039}^{2+}Fe_{0.011}^{3+}SiO_3$. The resolution of the Mössbauer spectrum was not sufficient to determine the site distribution of Fe³⁺, and the concentration of Fe³⁺ was too small to be able to discern the substitution mechanism from the electron microprobe data. However based on literature data (e.g., Vanpeteghem *et al.*, 2006b), Fe³⁺ is expected to substitute

predominantly for Mg^{2+} rather than for Si^{4+} . Energy dispersive powder X-ray diffraction patterns were processed using full profile LeBail refinement with *Jana2006* (Petricek *et al.*, 2006). Patterns for both Mg-Pv and (Mg, Fe)-Pv samples, collected over the entire range of pressure and temperature investigated were indexed to the Pbnm perovskite structure. No evidence for decomposition or the presence of additional phases was observed. Corresponding zero pressure densities were $\rho_0 = 4.110(4) \text{ g}\cdot\text{cm}^{-3}$ and $\rho_0 = 4.429(4) \text{ g}\cdot\text{cm}^{-3}$, for the Mg-Pv and the (Fe, Mg)-Pv samples respectively, in good agreement with the bench top measurements of densities determined using the Archimedes' method, 4.11 and 4.43 $\text{g}\cdot\text{cm}^{-3}$, respectively (**Table 5.3.1.1**). Room temperature elastic properties can be extracted from density (ρ) and compressional (V_P) and shear (V_S) velocity data, independently of X-ray pressure determinations, employing 3rd order finite strain equations (Davies and Dziewonski, 1975) described in §4.3.2. Least squares fitting of equations 4.3.2.1, 4.3.2.2 and 4.3.2.3 to the data yield the values are given in **Table 5.3.1.2**. For Mg-Pv, values refined for G and G' are in good agreement with previous studies (Sinogeikin *et al.*, 2004; Murakami *et al.*, 2007) while the determined K_S is slightly lower than the range found in more recent studies (Sinogeikin *et al.*, 2004; Li and Zhang, 2005). As our experimental data are sparse at lower pressures, better constraints were provided by fitting a combined data set from this study and Li and Zhang (2005). The resulting fit, shown by the curves in **Figure 5.3.1.1**, is in excellent agreement with the room pressure value for K_S of Sinogeikin *et al.* (2004).

Pressure (GPa)	Temperature (K)	V_P (km.s ⁻¹)	V_S (km.s ⁻¹)	ρ (g.cm ⁻³)
0	300			4.110(4)
1.32	300	10.91(7)	6.57(4)	4.130(4)
12.47	300	11.44(7)	6.78(4)	4.304(4)
14.22	300	11.49(7)	6.80(4)	4.330(4)
15.68	300	11.61(7)	6.81(4)	4.353(4)
16.99	300	11.67(7)	6.82(4)	4.374(4)
18.99	300	11.75(7)	6.84(4)	4.405(4)
20.5	300	11.86(7)	6.86(4)	4.428(4)
21.52	300	11.86(7)	6.89(4)	4.443(4)
21.22	700	11.67(7)	6.78(4)	4.409(4)
20.29	1200	11.39(7)	6.61(4)	4.368(4)

Table 5.3.1.1a: Experimental conditions and the results for MgSiO₃.

Pressure (GPa)	Temperature (K)	V_P (km.s ⁻¹)	V_S (km.s ⁻¹)	ρ (g.cm ⁻³)
0	300			4.429(4)
0.99	300	10.71(7)	6.49(4)	4.431(4)
3.99	300	10.81(7)	6.53(4)	4.523(4)
7.2	300	10.97(7)	6.58(4)	4.539(4)
9.5	300	11.10(7)	6.63(4)	4.542(4)
12.72	300	11.24(7)	6.66(4)	4.557(4)
16.99	300	11.46(7)	6.71(4)	4.536(4)
18.52	300	11.50(7)	6.74(4)	4.595(4)
21.01	300	11.63(7)	6.74(4)	4.544(4)
22.8	300	11.72(7)	6.78(4)	4.556(4)
24.47	300	11.84(7)	6.84(4)	4.542(4)
22.73	700	11.55(7)	6.69(4)	4.701(4)
24.47	700	11.62(7)	6.73(4)	4.735(4)
24.8	1200	11.41(7)	6.60(4)	4.929(4)

Table 5.3.1.1b: Experimental conditions and the results for (Mg_{0.95},Fe_{0.05})SiO₃.

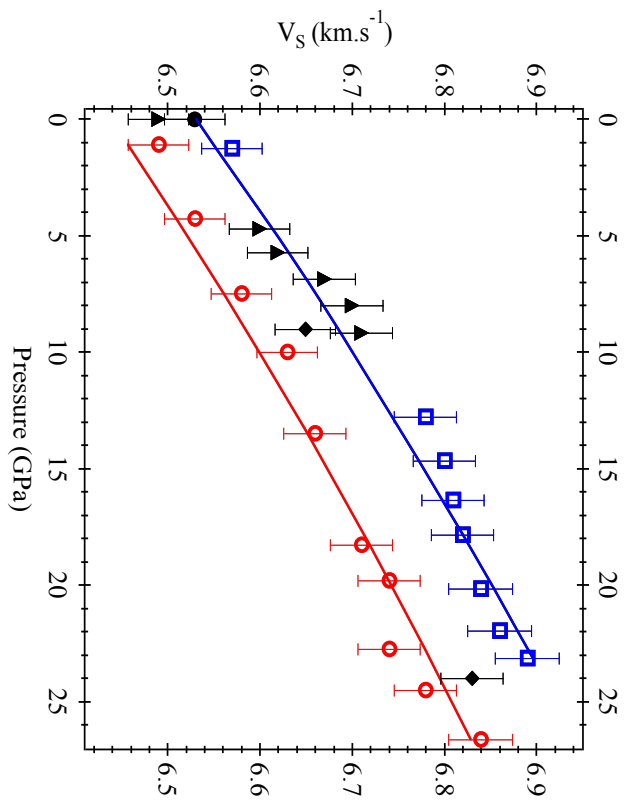
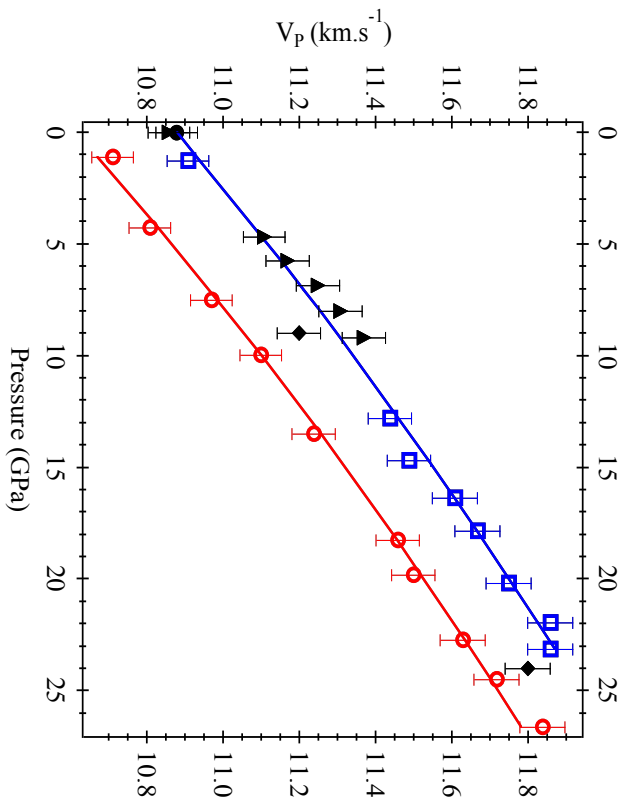


Figure 5.3.1.1: Compressional and shear wave velocities of perovskite samples measured at room temperature. Blue open squares indicate velocities measured in this study for MgSiO_3 perovskite while the red open circles show results for $(\text{Mg}_{0.95}\text{Fe}_{0.05})\text{SiO}_3$ perovskite. Black symbols indicate previous results for MgSiO_3 perovskite, triangles – Li and Zhang (2005), diamonds – Murakami et al. (2007) and circles – Sinogeikin et al. (2004).

MgSiO ₃ perovskite	K_S (GPa)	K'	G (GPa)	G'
This study	247(4)	4.5(2)	176(2)	1.6(1)
This study + <i>Li and Zhang</i> [2005]	252(1)	4.1(1)	175(1)	1.66(6)
<i>Li and Zhang</i> [2005]	253(2)	4.4(1)	173(1)	2.0(1)
<i>Sinogeikin et al.</i> [2004]	253		171-175	
<i>Murakami et al.</i> [2007]			172.9(15)	1.56(4)
MgSiO ₃ compression studies	K_T	K'		
<i>Boffa Ballaran et al.</i> [2012]	251 (2)	4.11 (7)		
<i>Ross and Hazen</i> [1990]	254			
<i>Fiquet et al.</i> [2000]	259.5(9)			
<i>Vanpeteghem et al.</i> [2006a] (K' fixed)	253(1)	4.0		
$(Mg_{0.95}Fe_{0.04}^{2+}Fe_{0.01}^{3+})SiO_3$	K_S	K'		
This study	236(2)	4.7(1)	174(1)	1.56(5)
(Mg,Fe)SiO ₃ compression studies	K_T	K'		
<i>Boffa Ballaran et al.</i> [2012] 0-75 GPa*	253 (2)	3.99 (7)		
<i>Boffa Ballaran et al.</i> [2012] 0-40 GPa*	245 (4)	4.4 (3)		
<i>Boffa Ballaran et al.</i> [2012] 0-25 GPa*	236 (7)	5.6 (8)		
<i>Andrault et al.</i> [2001] (K' fixed)	255.4	4.0		
<i>Mao et al.</i> [1991] (K' fixed)	261(4)	4.0		

* Indicates the range of pressure over which the compression data have been fitted.

Table 5.3.1.2: Elastic parameters for Mg-Pv and (Mg, Fe)-Pv.

The value for K_S refined from the $Mg_{0.95}Fe_{0.039}^{2+}Fe_{0.011}^{3+}SiO_3$ perovskite data is significantly lower than the value derived for Mg-Pv. Although no experimental studies exist with which to compare K_S for (Mg, Fe)-Pv, it can be compared with previous determinations of K_T (the isothermal bulk modulus) obtained from diamond anvil cell compression measurements, which at room temperature should be ~2 GPa lower than K_S . In a recent compression study performed to 75 GPa employing single crystal X-ray diffraction, K_T of $(Mg_{0.96}Fe_{0.04})SiO_3$ perovskite was found to be 253(2) GPa with K' refined to be 3.99 (*Boffa Ballaran et al.*, 2012). This composition is close to that of the sample studied here, $Mg_{0.95}Fe_{0.039}^{2+}Fe_{0.011}^{3+}SiO_3$, although the $Fe^{3+}/\Sigma Fe$ ratio of this previous sample was not measured. This value is 15 GPa lower than the value refined in this study and far outside of the experimental uncertainty. However, *Boffa Ballaran et al.* (2012) noted that if their compression data were fitted over a smaller pressure range, then lower values of K_T were obtained with higher corresponding values of K' . If the data are fitted

using a 3rd order Birch-Murnaghan equation of state between room pressure and 40 GPa, for example, then the corresponding K_T reduces to 245 GPa, while fitting to only 25 GPa, i.e. over a similar pressure range to this study, results in a K_T of 236 GPa, which is in perfect agreement with that determined here. Similarly Saikia *et al.* (2009) reported relatively low values of K_T and high K' for Al- and Fe-bearing perovskite from compression data collected to <10 GPa, whereas Boffa Ballaran *et al.* (2012) reported higher K_T and $K' \sim 4$ for similar a Fe- and Al-bearing perovskite collected to 75 GPa. The observations of Boffa Ballaran *et al.* (2012) combined with the present study seem to point to a lowering of the bulk modulus for Fe-bearing perovskite at lower pressure conditions. As lower room-pressure K_T values found for smaller pressure ranges average out to give higher K_T values in data collected to significantly higher pressure, this seems to indicate that there may be a stiffening of the structure encountered at higher pressure. Boffa Ballaran *et al.* (2012) attribute this behavior to a change in the compression mechanism for Fe-bearing perovskite in the region of 30-40 GPa. If so this is beyond the pressure range accessible to our measurement technique. It should be noted that fitting the (Mg, Fe)-Pv data from our study to a 4th order finite strain equation (Davies and Dziewonski, 1975) results in very little improvement to the fit, implying that any higher order change in the K_S dependence with pressure occurs at pressures higher than our study or is too subtle to be constrained using our data. Further studies will be required to clarify this aspect.

In the current study insufficient data were collected at high temperature to refine thermal parameters for a high temperature equation of state. However the experimental data can be used to test the accuracy of existing thermo-elastic models. In **Figure 5.3.1.2** the experimentally determined velocities are compared with those calculated using the thermodynamically self-consistent model described by Stixrude and Lithgow-Bertelloni (2005). This model employs a 3rd order Eulerian finite strain formulation to describe effects of cold compression while the thermal contribution is obtained through a Mie-Grüneisen type approach. In total 9 parameters are required to describe V_S and V_P as a function of P and T. Parameters that describe the temperature dependence, θ , the Debye temperature, γ , the Grüneisen parameter, q , the volume dependence of γ , and η , the shear strain derivative of γ , are taken from the refinement reported by Xu *et al.* (2008), while

the room temperature parameters V_0 , K_T , K' , G and G' are taken from our data. For the $Mg_{0.95}Fe_{0.039}^{2+}Fe_{0.011}^{3+}SiO_3$ perovskite the temperature dependence parameters are estimated from a linear interpolation of the Fe and Mg perovskite end-member values reported by Xu *et al.* (2008). All parameters employed are given in **Table 5.3.1.2**. As shown in **Figure 5.3.1.2**, the model calculation is in good agreement with the measured V_P and V_S up to 1,200 K. The largest deviation arises for the highest temperature (Mg, Fe)-Pv data, for which the temperature determination is highly uncertain due to the failure of the thermocouple.

		V_0 ($\text{cm}^3 \text{mol}^{-1}$)	K_T (GPa)	K'	G (GPa)	G'	θ (K)	γ	q	η
MgSiO ₃	Perovskite	24.42	252	4.1	175	1.66	901	1.44	1.4	2.6
(Mg _{0.95} Fe _{0.05})SiO ₃	Perovskite	25.50	236	4.7	174	1.56	765	1.44	1.4	2.56
MgO	Oxide	<i>11.24</i>	<i>161</i>	3.8	<i>131</i>	2.1	767	1.36	1.7	2.8
FeO	Oxide	<i>12.26</i>	<i>179</i>	4.9	59	1.4	454	1.53	1.7	-0.1
CaSiO ₃	Perovskite	<i>27.45</i>	<i>236</i>	3.9	<i>157</i>	2.2	796	1.89	0.9	1.3

Values in italics are from Xu *et al.* (2008) all other data are from this study.

Table 5.3.1.3: Properties of lower mantle phases.

Using the data given in **Table 5.3.1.3**, the S and P-wave velocities for a simplified bulk silicate earth (BSE) composition at the top of the lower mantle were also calculated. The calculation assumes a lower mantle comprising 67 mole % (Mg_{0.95}Fe_{0.05})SiO₃ perovskite, 27 % (Mg_{0.86}Fe_{0.14})O and 6 % CaSiO₃ perovskite, with compositions and proportions consistent with an Al-free BSE composition in the lower mantle (McDonough and Sun, 1995; Nakajima *et al.*, 2012). Equation of state data for (Mg,Fe)O ferropericlase and CaSiO₃ perovskite are also taken from Xu *et al.* (2008). The proposed effect of the Fe spin transition in ferropericlase on velocities was not taking into account, which may drive V_S in particular to slightly higher values. The calculation is performed along the geotherm of Brown and Shankland (1981). The propagated error is determined to be 2 %, arising mainly from the temperature extrapolation. In **Figure 5.3.1.3** the calculation is compared with the seismic reference models PREM (Dziewonski and

Anderson, 1981) and AK135 (Kennett et al., 1995). Deviation between the model calculation and the seismic reference models below 800 km likely results from the absence of garnet in the mineralogical model employed. The presence of garnet would lower seismic velocities at the very top of the lower mantle. With increasing pressure, garnet breaks down and becomes absent by 800 km (Dziewonski and Anderson, 1981; Kennett *et al.*, 1995; Weidner and Wang, 2000). The comparison indicates that even given the low values of K_S determined for $(\text{Mg}_{0.95}\text{Fe}_{0.05})\text{SiO}_3$ perovskite, the estimated velocities of our mineralogical model are quite consistent with the seismologically determined lower mantle models. Although Murakami *et al.* (2012) recently suggested that the effect of Al in MgSiO_3 would bring down lower mantle S-wave velocities for a BSE composition mantle to levels incompatible with seismic measurements, this seems not to be the case for Fe substitution in perovskite alone. It remains to be seen, however, what effect Fe and Al have on perovskite shear wave properties.

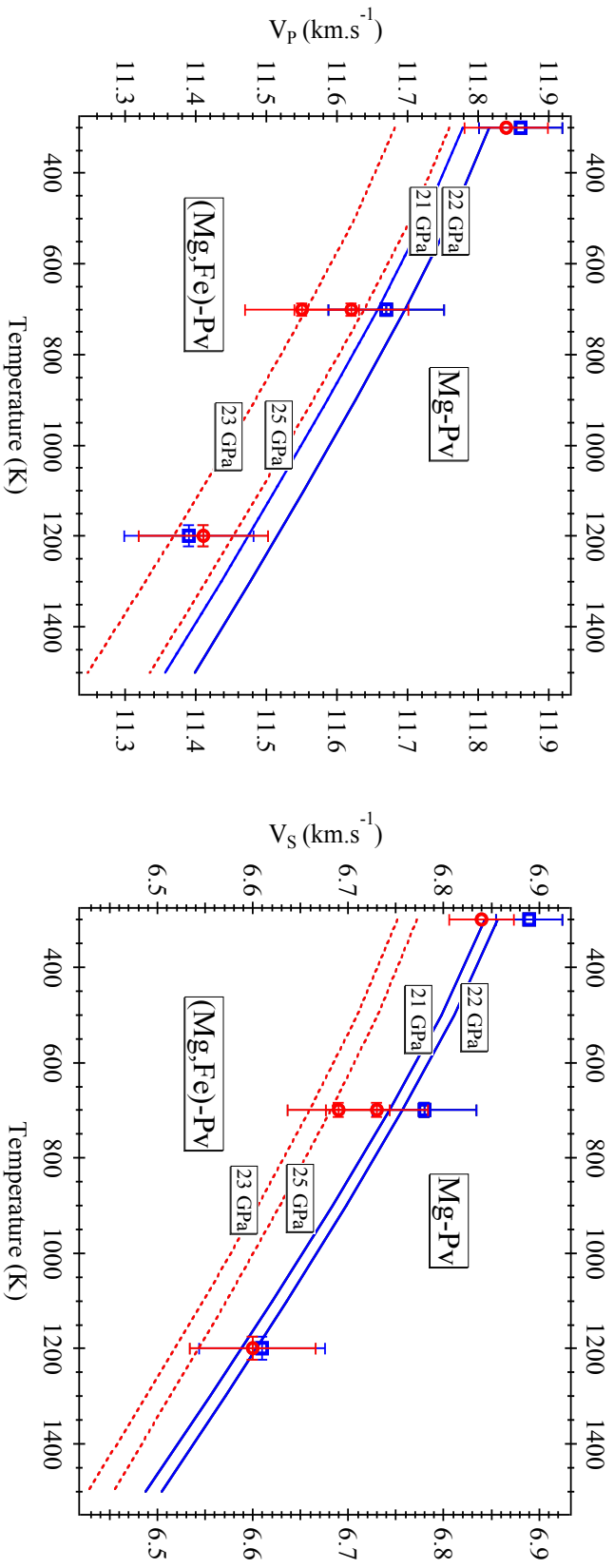


Figure 5.3.1.2: Compressional and shear wave velocities of perovskite at high pressure as a function of temperature. Blue open squares indicate velocities measured in this study for MgSiO_3 perovskite while the red open circles show results for $(\text{Mg}_{0.95}\text{Fe}_{0.05})\text{SiO}_3$ perovskite. The high temperature MgSiO_3 data are collected at pressures between 21 and 22 GPa while data for $(\text{Mg}_{0.95}\text{Fe}_{0.05})\text{SiO}_3$ are collected between 23 and 25 GPa. Curves are calculated from the thermo-elastic model parameters given in Table 5.3.1.3 and taken from Xu et al. (2008), with the blue solid and red dashed curves respectively standing for MgSiO_3 and $(\text{Mg}_{0.95}\text{Fe}_{0.05})\text{SiO}_3$ perovskites.

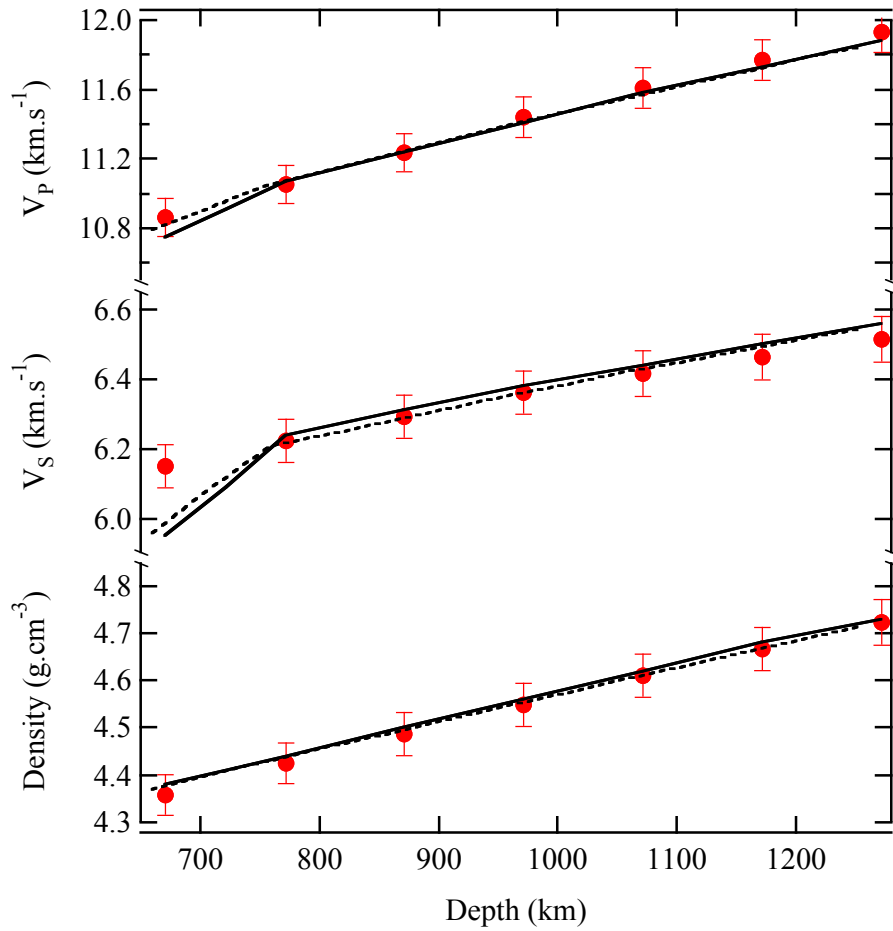


Figure 5.3.1.3: Estimates for V_s and V_p of a BSE bulk composition comprising $(Mg,Fe)SiO_3$ perovskite, $(Mg,Fe)O$ ferropericlae and $CaSiO_3$ perovskite are shown as the red filled circles and their associated errors calculated at the pressures and temperatures corresponding to the lower mantle depths indicated. Data for $(Mg,Fe)SiO_3$ perovskite are taken from the equation of state model determined in this study, while models for the other phases are taken from the literature. The solid and dashed curves show PREM and AK135 seismic reference models for the lower mantle.

5.3.2 Effect of the combined Fe and Al substitutions

From the electron microprobe analysis and the Mössbauer spectroscopy measurements, the chemical formulas for the two Fe and Al bearing perovskite samples are $(Mg_{0.962}Fe_{0.026}^{2+}Fe_{0.014}^{3+})(Al_{0.025}Si_{0.98})O_3$ and $(Mg_{0.94}Fe_{0.037}^{2+}Fe_{0.039}^{3+})(Al_{0.055}Si_{0.954})O_3$. One can generally summarize these two perovskite samples as containing approximately 2% Fe³⁺ and Al and 4% Fe³⁺ and Al, which hence forth will be denoted as 2%Fe-Al and 4%Fe-Al MgPv. In Al and Fe bearing perovskite there are two plausible substitution mechanisms for Fe³⁺ and Al (Frost and Langenhorst 2002). A coupled substitution can occur where all Al on the octahedral Si site is charge balanced by Fe³⁺ on the dodecahedral site. On the other hand 3+ cations on the octahedral site can be charge balanced by the creation of oxygen vacancies. For the 2%Fe-Al sample there appears to be a slight excess of Fe³⁺ for the coupled substitution mechanism, however, within the analytical uncertainties a coupled substitution is quite viable. On the other hand the 4%Fe-Al sample contains 0.016 atoms excess of Al, which might possibly be an indication for the existence of oxygen vacancies in this sample, however, this indication is also on the border of the analytical uncertainties. The analysis of Fe in perovskite using the electron microprobe may well entail larger uncertainties than those apparent, due to differences in nature between perovskite and the analytical standards employed.

The X-ray diffraction data for 2%Fe-Al and 4%Fe-Al were processed using the same procedure as described for the Mg-Pv and (Mg, Fe)-Pv samples. No evidence for decomposition or the presence of additional phases was observed in the recovered samples or from X-ray diffraction measurements made during the experiments. The X-ray density of the perovskite at each pressure and temperature was determined from the volume data combined with the chemical composition of the samples, yielding a zero-pressure density of $\rho_0 = 4.163(1) \text{ g.cm}^{-3}$ for 2%Fe-Al sample and $\rho_0 = 4.201(1) \text{ g.cm}^{-3}$ for 4%Fe-Al sample.

As describe in §5.3.1, energy dispersive powder X-ray diffraction patterns were treated using full profile LeBail refinement with the *Jana2006* software package (Petricek *et al.*, 2006). For both 2%Fe-Al and 4%Fe-Al samples, the patterns collected were

indexed to the Pbnm perovskite structure. The samples are single phase without evidence of decomposition. Density and P and S wave velocity data for 2%Fe-Al and 4%Fe-Al samples are reported in **Table 5.3.2.1** and **Figure 5.3.2.1** with pressure determined from the Au calibrant. The velocities measured for 2%Fe-Al are about 3% lower than for Mg-Pv, for both compressional and shear waves, and about 1% lower than for (Mg, Fe)-Pv. For the 4%Fe-Al sample, the velocities are approximately 5.5% lower than for Mg-Pv and 3.5% lower than for (Mg, Fe)-Pv. The room temperature elastic properties were extracted using the same 3rd finite strain equations as for Mg-Pv and (Mg, Fe)-Pv (Davies and Dziewonski, 1975), described in §4.3.2. The least square fitting of those equations to the experimental data yield the values presented in **Table 5.3.2.2**.

Figure 5.3.2.2 reports the elastic constants of the investigated perovskite samples as a function of the total Fe and Al contents. When the refined values of K_S for the four compositions are plotted as a function of the total Fe concentration they form a trend with a gradual decrease of K_S with increasing total Fe content. K_S for 2%Fe-Al is significantly lower than the value derived for Mg-Pv and slightly higher than (Mg, Fe)-Pv, which appears to be reasonable once the total Fe contents are considered. The 2%Fe-Al sample K_S is approximately 30 GPa below the value for Mg-Pv and considerably lower than the two Fe-poorer compositions. Fe seems, therefore, to have a consistent effect on K_S , strongly lowering it in both Al and Al-free perovskites. On the other hand, **Figure 5.3.2.2** shows that the same trend is not observed for G . The values of G for Mg-Pv, (Mg, Fe)-Pv and 2%Fe-Al are identical, within the errors, 174 to 177 GPa. Only one study exists with which to compare the Al-bearing perovskite results. Murakami *et al.* (2012) determined V_S for MgSiO₃ (+4wt% Al₂O₃) perovskite at high pressure and high temperature using a new Brillouin scattering system. Low contents of Fe and Al appear to not have any effect on the shear modulus. G for the 4%Fe-Al perovskite sample is significantly lower than for the other compositions, 166 GPa, but nevertheless consistent with a decrease in G as observed by Murakami *et al.* (2012), who also reported a value of 166 GPa. For Al content higher than 2 ± 0.5 wt%, there is a dramatic drop in G , without a significant effect on K_S . Both pressure derivatives K_S' and G' for 2%Fe-Al and 4%Fe-Al, respectively 3.9, 4.8 and 1.3, 1.5, are in the same range as the one obtained for Mg-Pv and (Mg, Fe)-Pv (**Table 5.3.2.2**).

Pressure (GPa)	Temperature (K)	V_P (km.s ⁻¹)	V_S (km.s ⁻¹)	ρ (g.cm ⁻³)
2.82	298	10.62	6.49	4.180
7.14	298	10.85	6.55	4.221
9.01	298	10.93	6.57	4.277
12.37	298	11.03	6.62	4.320
15.24	298	11.22	6.66	4.372
18.13	298	11.32	6.68	4.418
20.13	298	11.46	6.71	4.474
22.47	298	11.58	6.74	4.498
25.08	298	11.64	6.77	4.554
25.67	383	11.61	6.75	4.535
24.69	495	11.52	6.72	4.513
22.97	583	11.44	6.69	4.502
22.59	675	11.38	6.68	4.481
27.10	513	11.70	6.79	4.558
26.41	685	11.49	6.71	4.541
24.50	878	11.38	6.67	4.493
23.25	1075	11.30	6.63	4.450
23.09	1345	11.21	6.60	4.420
20.97	1055	11.19	6.61	4.429
21.02	880	11.24	6.63	4.440
20.83	665	11.30	6.66	4.451
20.45	475	11.38	6.69	4.510
19.26	298	11.35	6.69	4.465
13.97	298	11.22	6.65	4.379
8.94	298	11.08	6.61	4.309
4.05	298	10.95	6.58	4.234

Table 5.3.2.1a: Experimental conditions and the results for $(Mg_{0.962}, Fe_{0.038})(Al_{0.02}, Si_{0.98})O_3$.

Pressure (GPa)	Temperature (K)	V_P (km.s ⁻¹)	V_S (km.s ⁻¹)	ρ (g.cm ⁻³)
0.73	298	10.23	6.27	4.190
4.19	298	10.38	6.31	4.241
6.68	298	10.51	6.35	4.295
9.82	298	10.67	6.40	4.361
13.79	298	10.86	6.45	4.414
15.80	298	10.97	6.47	4.457
18.33	298	11.06	6.49	4.493
20.54	298	11.17	6.52	4.523
23.08	298	11.30	6.54	4.561
25.52	298	11.40	6.56	4.593
25.51	298	11.43	6.57	4.592
25.06	487	11.32	6.53	4.579
25.18	715	11.19	6.50	4.555
24.31	885	11.04	6.44	4.522
22.27	1175	10.83	6.36	4.466
21.50	860	10.93	6.41	4.481
20.98	680	11.02	6.46	4.501
20.90	475	11.12	6.49	4.511
20.45	298	11.20	6.54	4.528
18.40	298	11.13	6.51	4.494
15.12	298	10.99	6.48	4.448
11.54	298	10.79	6.43	4.392
8.39	298	10.64	6.38	4.321
5.04	298	10.46	6.34	4.261
3.20	298	10.36	6.31	4.210

Table 5.3.2.1b: Experimental conditions and the results for $(Mg_{0.932}, Fe_{0.075})(Al_{0.049}, Si_{0.943})O_3$.

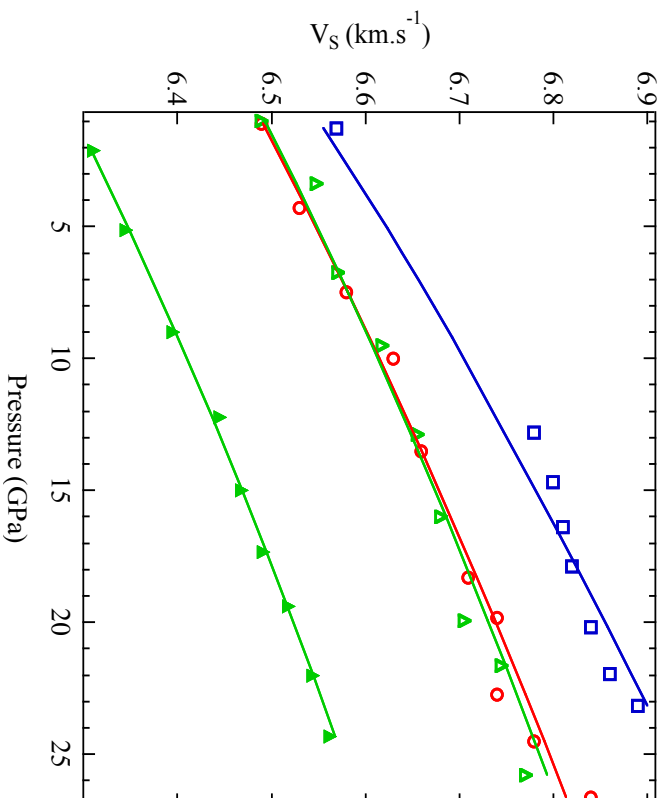
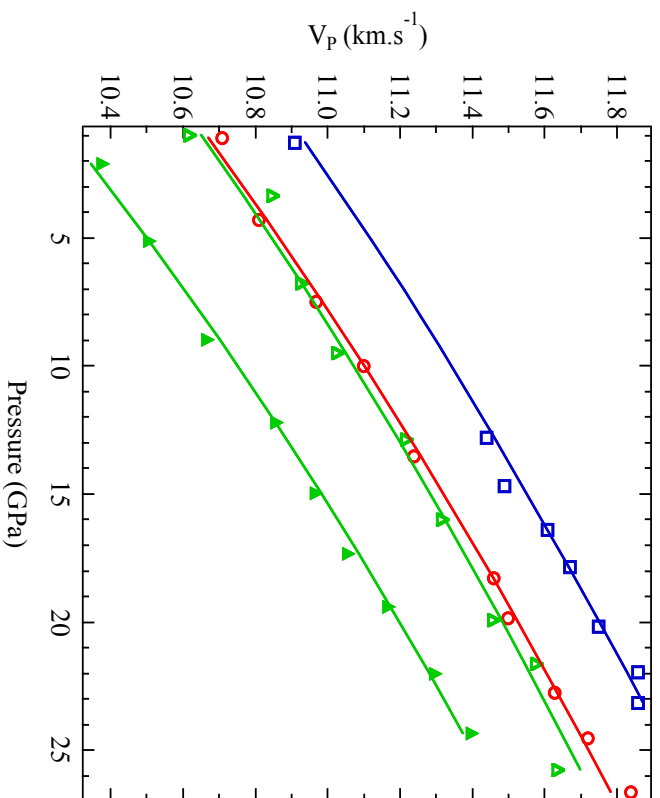


Figure 5.3.2.1: Compressional and shear wave velocities of perovskite samples measured at room temperature. All the symbols stand for the experimentally determined data. Blue open squares indicate velocities measured in this study for MgSiO_3 perovskite while the red open circles show results for $(\text{Mg}_{0.95}\text{Fe}_{0.05})\text{SiO}_3$ perovskite. Open green triangles indicate results for $(\text{Mg}_{0.96}^{2+}\text{Fe}_{0.038}^{2+}\text{Al}_{0.02}^{99}\text{Si}_{0.98}^{88})\text{O}_3$ and filled green triangles results for $(\text{Mg}_{0.93}^{2+}\text{Fe}_{0.07}^{2+}\text{Al}_{0.02}^{99}\text{Si}_{0.94}^{83})\text{O}_3$ perovskite. Curves are calculated from the thermo-elastic model parameters given in Table 5.3.1.3 and taken from Xu et al. (2008).

References	K_S (GPa)	K'	G (GPa)	G'
$MgSiO_3$				
This study	247(4)	4.5(2)	176(2)	1.6(1)
This study + Li and Zhang (2005)	252(1)	4.1(1)	175(1)	1.7(1)
$(Mg_{0.95}Fe_{0.04}^{2+}Fe_{0.01}^{3+})SiO_3$				
This study	236(2)	4.7(1)	174(1)	1.6(1)
$(Mg_{0.962}Fe_{0.026}^{2+}Fe_{0.014}^{3+})(Al_{0.025}Si_{0.98})O_3$				
This study	242(3)	3.9(2)	177(1)	1.3(1)
$(Mg_{0.932}Fe_{0.037}^{2+}Fe_{0.038}^{3+})(Al_{0.049}Si_{0.943})O_3$				
This study	221(2)	4.8(2)	166(1)	1.5(1)
$Mg(Al_{0.078}Si_{0.922})O_3$				
Murakami et al. (2012)			166(1)	1.57(5)

Table 5.3.2.2: Elastic parameters for 2%Fe³⁺ and Al and 4% Fe³⁺ and Al.

G' for 4%Fe-Al, $G' = 1.5$, is in perfect agreement with the value obtained by Murakami *et al.* (2012), 1.57. As stated in §5.3.1, the substitution of Mg by Fe will occur in the A site of the perovskite. The incorporation of Fe appears to affect the longitudinal velocities and as a result affects K_S and K_S' . The A site appears to control the bulk elastic properties of the perovskite since the Fe contents in the composition of the samples do not have any noticeable effect on the shear elastic properties. Fe substitution decreases K_S and increases K_S' , which corresponds to lower values of V_P . One might theorize that Fe substituting for Mg causes the compressibility of the A site to increase.

On the other hand, the substitution of Si by Al takes place in the B site of the perovskite. Silica octahedra form the framework of the perovskite structure. By substituting Al into the Si octahedral site the rigidity of this framework is being disrupted which clearly has an influence on the shear modulus G. One can observe on the **Figure 5.3.2.2** that G of the Al-bearing perovskites is obviously controlled by the Al content in the structure; a fact that is in reasonable agreement with the value of G determined by Murakami *et al.* (2012). The substitution mechanism of Al in the perovskite of Murakami *et al.* (2012) is difficult to determine as no analyses are provided, however, it is most

likely a coupled substitution. In **Figure 5.3.2.2** the magnitude of the drop in G for the Murakami et al. data is smaller than when the data from this study are plotted simply against Al, however as Al and Fe^{3+} are in coupled substitution in the perovskite from this study it is more appropriate to compare the Murakami et al. data as a function of total Fe^{3+} and Al i.e. total 3+ cations. In this case the results from this study show a smaller dependence on the total 3+ cations than in the Murakami et al. study. This would imply that substitution of Al into the B site of perovskite has a smaller effect on G when it is coupled by Fe^{3+} substitution on the A site rather than Al on the A site.

During the experiments on 2%Fe-Al and 4%Fe-Al perovskite samples, high temperature data were collected. Then, following the same procedure as in **§5.3.1**, velocities were calculated, for those two compositions, using the thermodynamically self-consistent model of Stixrude and Lithgow-Bertelloni (2005). In this model, the room temperature parameters V_0 , K_T , K' , G and G' are taken from our data (**Table 5.3.2.2**), while the high temperature terms, θ , γ , q , and η , are refined within the range of their uncertainties to fit the experimental data. The experimental and calculated sets of velocities data are compared in the **Figure 5.3.2.3**. All parameters used in this model are given in **Table 5.3.2.3**.

Figure 5.3.2.3 shows that the model calculations and the measured velocities, up to temperatures of 1345K for 2%Fe-Al and 1175K for and 4%Fe-Al, are in excellent agreement. The maximum deviation is about 1 % between the two sets of data, and remains within the uncertainties. As stated in **§5.3.1** and shown in **Figure 5.3.1.2**, V_P and V_S of $Mg_{0.95}Fe_{0.04}^{2+}Fe_{0.01}^{3+}SiO_3$ are respectively about 2 % and 1 % slower than $MgSiO_3$. Comparing the high temperature data of 2%Fe-Al and 4%Fe-Al (**Figure 5.3.2.3**) to the curves calculated for $MgSiO_3$ from the thermo-elastic model parameters given in **Table 5.3.1.3** and taken from Xu *et al.* (2008), one observes that V_P and V_S have different behaviors. V_P of 2%Fe-Al and 4%Fe-Al are respectively about 2 and 4% slower than $MgSiO_3$ at 500K and 5 and 7% at 1200K. On the other hand, the variations of V_S of 2%Fe-Al and 4%Fe-Al relative to $MgSiO_3$ are 1 and 5% slower respectively but this difference is constant over the full temperature range,. V_S measured by Murakami *et al.*

(2012) on MgSiO_3 (+4 wt% Al_2O_3) at high temperature are consistent with our data, within the error, where the main errors are those of the temperature measurements. However, from room temperature up to the high temperatures measurements, both V_P and V_S of 2%Fe-Al remain about 4% slower than the V_P and V_S of 4%Fe-Al.

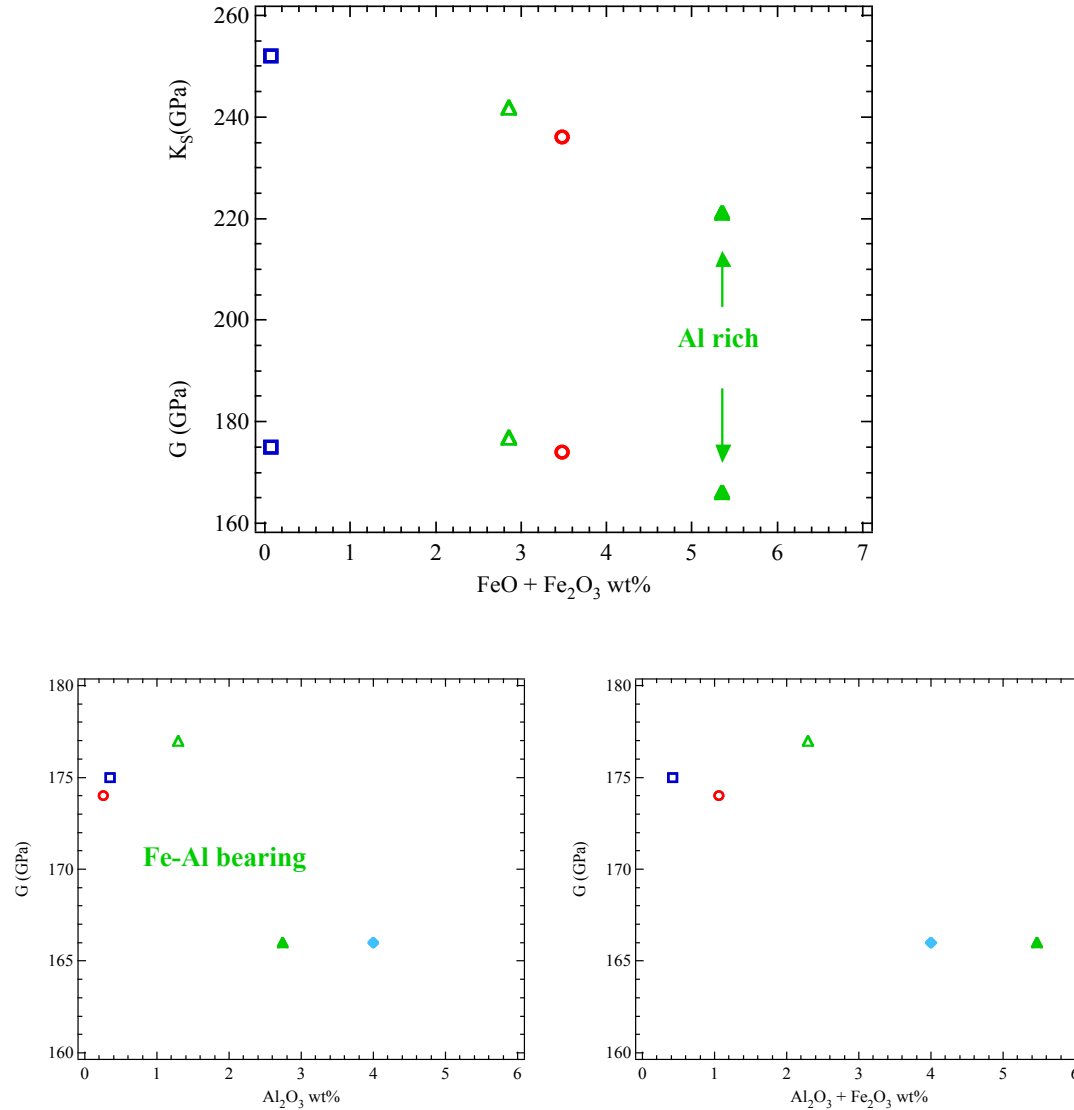


Figure 5.3.2.2: Bulk and shear moduli of perovskite samples measured at room temperature. Blue open squares indicate this study for MgSiO_3 perovskite while the red open circles show results for $\text{Mg}_{0.95}\text{Fe}_{0.04}^{2+}\text{Fe}_{0.01}^{3+}\text{SiO}_3$ perovskite. Open green triangles indicate results for $(\text{Mg}_{0.962}\text{Fe}_{0.026}^{2+}\text{Fe}_{0.014}^{3+})(\text{Al}_{0.025}\text{Si}_{0.98})\text{O}_3$ perovskite, filled green triangles results for $(\text{Mg}_{0.94}\text{Fe}_{0.037}^{2+}\text{Fe}_{0.039}^{3+})(\text{Al}_{0.055}\text{Si}_{0.954})\text{O}_3$ perovskite. Filled light blue diamond stand for $\text{Mg}(\text{Al}_{0.078}\text{Si}_{0.922})\text{O}_3$ from Murakami et al. (2012).

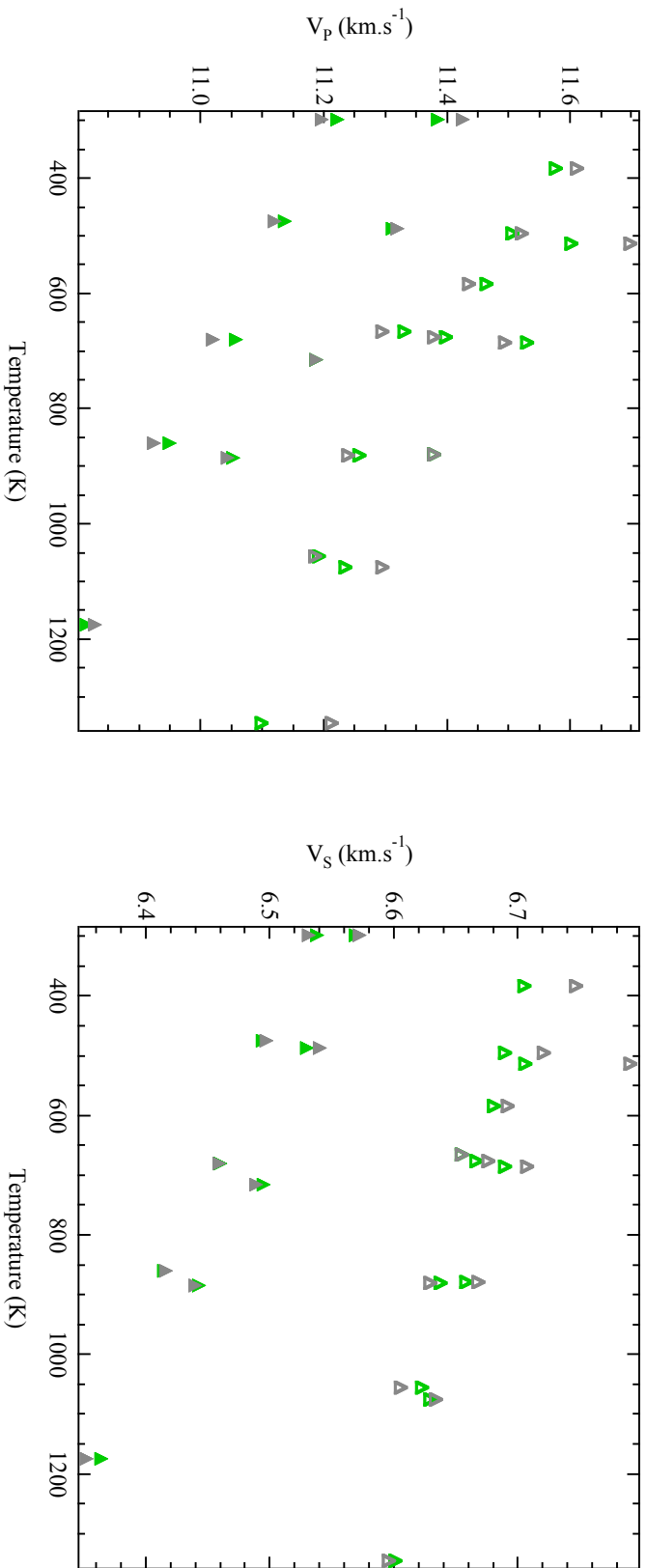


Figure 5.3.2.3: Compressional and shear wave velocities of perovskite at high pressure as a function of temperature. Green open triangles indicate velocities measured in this study for $(Mg_{0.962}, Fe_{0.038})(Al_{0.02}, Si_{0.98})O_3$ perovskite while the green filled triangles show results for $(Mg_{0.932}, Fe_{0.075})(Al_{0.049}, Si_{0.943})O_3$ perovskite. The high temperature data are collected at pressures between 20 and 25 GPa. Grey symbols are calculated from the thermo-elastic model parameters given in Table 5.3.1.3 and taken from Xu et al. (2008). With the open and filled triangles respectively standing for $(Mg_{0.962}, Fe_{0.038})(Al_{0.02}, Si_{0.98})O_3$ and $(Mg_{0.932}, Fe_{0.075})(Al_{0.049}, Si_{0.943})O_3$ perovskites.

	V_0 ($\text{cm}^3\text{mol}^{-1}$)	K_T (GPa)	K'	G (GPa)	G'	θ (K)	γ	q	η
$\text{Mg}_3\text{Al}_2\text{Si}_3\text{O}_{12}$	11.31	165	4	93	1.1	823	0.8	1.9	1.1
$\text{Fe}_3\text{Al}_2\text{Si}_3\text{O}_{12}$	11.54	172	4.1	96	1.5	741	0.8	2.6	2.9
$\text{Ca}_3\text{Al}_2\text{Si}_3\text{O}_{12}$	12.51	163	3.2	109	1.2	823	0.8	2.4	1.8
$\text{Mg}_4\text{Si}_4\text{O}_{12}$	11.43	160	3.8	81	1.3	835	0.8	2.6	2.4
Mg_2SiO_4	3.95	185	4.2	123	1.4	891	1.11	2.4	2.3
Fe_2SiO_4	4.19	213	4.2	92	1.4	652	1.26	2.4	1.8
$\text{Mg}_4\text{Si}_4\text{O}_{12}$	12.15	116	6.2	88	1.8	823	1.12	0.2	2.1
$\text{Fe}_4\text{Si}_4\text{O}_{12}$	12.77	116	6.2	68	1.8	690	1.12	0.2	0.7
Mg_2SiO_3	24.42	252	4.1	175	1.7	901	1.44	1.4	2.6
2% Fe^{3+} and Al	24.44	242	3.9	177	1.3	900	1.77	5.2	0.4
4% Fe^{3+} and Al	24.57	221	4.8	166	1.5	893	2.13	4.6	1.9
MgO	11.24	161	3.8	131	2.1	767	1.36	1.7	2.8
FeO	12.26	179	4.9	59	1.4	454	1.53	1.7	-0.1
CaSiO_3	27.45	236	3.9	157	2.2	796	1.89	0.9	1.3

Values in italics are from Xu *et al.* (2008) all other data are from this study.

Table 5.3.2.3: Properties of mantle phases.

Conditions	Mineral proportions (in mol fractions)							
	P (GPa)	Temp. (K)	Garnet	HP-olivine	HP-clinopyroxene	CaSiO_3 -pv	Ferropericlase	(Al, Fe)Mg-pv
634	22	1773	0.38	0.57	0.05	-	-	-
645	23	1773	0.38	0.57	0.05	-	-	-
674	24	1773	0.15	0.10	-	0.08	0.15	0.52
695	25	1773	0.08	-	-	0.08	0.16	0.68
765	28	1873	-	-	-	0.10	0.16	0.74

Table 5.3.2.4: Proportion in the 660 km discontinuity region.

5.3.2.1 Implications for the velocity jump at the 660 km discontinuity.

Model calculations for P- and S- waves velocities for a pyrolitic composition in the 660 km discontinuity region have been performed using the data given in **Table 5.3.2.3**. The calculations were performed between 634 km and 765 km in order to determine the velocity variations related to the changes in the mineralogy and phase proportions, **Table 5.3.2.4**. The proportion and the chemical composition of each phase have been calculated from a pyrolite mantle composition (Irifune, 1994). Equations of state data for $(\text{Mg,Fe})_2\text{SiO}_4$ ringwoodite, $(\text{Mg,Fe})_2(\text{Si,Al})_2\text{O}_6$ high pressure clinopyroxene (hereafter referred as HP-clinopyroxene), $(\text{Mg,Fe})\text{O}$ ferropericlaase and CaSiO_3 perovskite were taken from Xu *et al.* (2008). For the $(\text{Mg,Fe,Ca})_3(\text{Si,Al})_2\text{Si}_3\text{O}_{12}$ garnet and $(\text{Mg,Fe})(\text{Si,Al})\text{O}_3$ perovskite, the properties have been taken from this study, **Table 5.3.2.3**. The calculations are performed following the geotherm of Brown and Shankland (1981).

In **Figure 5.3.2.1.1**, the modeled velocities are compared with the seismic reference models PREM (Dziewonski and Anderson, 1981) and Ak135 (Kennett *et al.*, 1995). In the model calculation velocities are lower than the seismic reference models between 660-670 km. Reference models, however, may not fit absolute velocities accurately in the transition zone. This arises because there is high correlation between velocity gradients and velocity discontinuities in the transition zone and the reference models do not have sufficient constraints to partition velocity changes accurately between these two features. This is shown clearly in the study of Cammarano *et al.* (2005) who found a significant range of velocity models, with differing gradients and discontinuity magnitudes could still be refined to the same seismic observations used in seismic reference models. The PREM model, for example, does not include the occurrence of a discontinuity at 520 km due to the transformation of wadsleyite to ringwoodite. For this reason the magnitude of the PREM velocity gradient has to be much steeper in the transition zone to make up for the absence of this sharper velocity increase. Seismic reference models are also insensitive to the structure of discontinuities. Phase transformations are not instantaneous increase in velocity, as in the reference models, but occur over depth intervals caused by multivariant partitioning of major elements.

Reference models do not have sufficient constraints to resolve this detailed structure.

As shown in **Figure 5.3.2.1.1**, V_S presents a profile similar to the seismic reference model with a sharp discontinuity between 660 and 670 km depth. The jump observed at the 660 km discontinuity in the seismic reference models is larger than in the V_S from the model derived in this study. In the model derived here, the mineralogy of the assemblage and the composition of each phases evolve with the elevation of the pressure and temperature conditions (Irifune, 1994). Reaching 660 km depth, ringwoodite and HP-clinopyroxene break down; the garnet proportion decreases until 800 km depth (Weidner and Wang, 2000), while ferropericlase and Ca- and Mg- perovskites appear and their proportions increase. This gradual change in the phase proportions results, in terms of V_S , in a smaller jump at the 660 km, mainly due to the sudden change of the major phase, ringwoodite to Mg-perovskite. In **Figure 5.3.2.1.1**, however, the model predicts a much greater increase in V_S after the 660 velocity jump up to around 770 km. This occurs due to the transformation of garnet in the rock to perovskite and at depths above 800 km where this transformation is complete the model determined here returns to be in good agreement with reference models in the lower mantle. Therefore the model presented here implies a different structure in the V_S velocity of the transition zone in comparison to reference models. The jump at the 660 km discontinuity in V_S is smaller but the gradient below the 660 in the top of the lower mantle is much larger than in reference models. Given the play-off between gradients and discontinuities it is unlikely that the reference models can differentiate between models where more complexity exists in the velocity gradient. This has been clearly demonstrated by the analysis of Cammarano *et al.* (2005) where many different minerals models are fitted to the same seismic data using to determine the PREM model.

On the other hand the model for V_P determined here predicts no 660 km velocity jump. This is due to the low bulk modulus determined for Fe and Al bearing perovskite. Even after the 660 km depth the V_P of the mantle is predicted to remain significantly below the PREM model prediction and only when extrapolated to greater depths would V_P in the lower mantle be compatible with reference models.

Reflection seismology studies provide far more information on the structure of discontinuities than seismic reference models. In reference models the position of a

discontinuity is constrained and not part of the refinement, where as the magnitude of the discontinuity is refined but is highly correlated with the local velocity gradient both before and after the discontinuity. Shear and compressional waves that are reflected from transition zone discontinuities, however, appear as precursors of the seismic phases *SS* and *PP*, which can be examined to provide accurate estimates of the depth and impedance contrast at the discontinuities. Using *SS* precursors studies have established that there are two major transition zone discontinuities at approximately 410 and 660 km depth in the Earth, and a slightly weaker discontinuity at 520 km (Deuss *et al.*, 2006; Flanagan and Shearer, 1998; Houser *et al.*, 2008; Shearer and Flanagan, 1999). However, stacks of phases that precede the *PP* phase show that the reflection from 410 km is present, but the reflection from 660 km is not observed (Estabrook and Kind, 1995). The reflection coefficients at each discontinuity are sensitive to the change in V_P and V_S . The low visibility of underside *PP* reflections from 660 km discontinuity means that the velocity contrasts at the 660 km depth are much lower than expected from PREM (Dziewonski and Anderson, 1981) and Ak135 (Kennett *et al.*, 1995). This has in the past caused controversy as many seismic studies have attempted to image or explain the lack of underside *PP* reflections from the 660 km discontinuity.

To explain the absence of *P660P*, Estabrook and Kind (1995) proposed the EK1 model, which has considerably smaller velocity and density jumps than PREM. Estabrook and Kind (1995) hypothesized that the change in bulk modulus across the 660 km discontinuity is small. It was supported by the study of Shearer and Flanagan (1999), who predicted zero change in bulk modulus. The experimental data and model derived in this study results in an estimate for the perovskite bulk modulus $K_S = 221$ GPa, which is low in comparison to previous experimental estimates (**Table 5.3.2.2**) but does result in virtually zero change in the bulk modulus at the transformation of ringwoodite to perovskite plus magnesiowüstite.

Deuss *et al.* (2006) suggested that the null results in other studies of *PP* precursors are probably due to the fact that the discontinuity is highly variable on a regional scale, causing reflections to cancel out when large areas are stacked together. Their observations of *P660P* imply nonzero changes in bulk modulus and larger changes in density, as compared with previous studies (Estabrook and Kind, 1995; Shearer and

Flanagan, 1999). The bulk modulus and density jumps at a 660 km depth must vary laterally with lower values in regions where the 660 km discontinuity is not seen in *PP* and with larger values in areas where observations are made. If lateral variations in temperature were the only cause of lateral variations in the properties of the 660 km discontinuity, it should be deeper in colder areas (i.e., subduction zones) and shallower in hotter areas (i.e., mantle plumes), and one should see the same effect in both *PP* and *SS* precursors. However, *PP* and *SS* show different behavior in the same location. Thus, the regional variation in the 660 km discontinuity cannot be explained by lateral temperature variations on the post-spinel phase transition only and implies the presence of additional phase transitions and lateral differences in mantle composition. The appropriate candidates for the source of multiple discontinuities are phase changes in the non-olivine mantle components. Majorite garnet coexists with perovskite over a relatively large pressure and temperature range (Helffrich and Wood, 1996; Stixrude, 1997), and the transition occurs over a considerable depths range, resulting in a smaller seismic discontinuity at a 660 km depth followed by a strong gradient in seismic properties across a 660 to 720 km depth (**Figure 5.3.2.1.1**). Subducted basaltic crust at the bottom of the transition zone is mainly composed of mid-oceanic ridge basalt (MORB), which has a phase transition to perovskite at 720 km depth and could be invoked to explain some of the reflections up to this depth observed by Deuss *et al.* (2006).

In **Figure 5.3.2.1.2**, the compressional wave acoustic impedance Z has been calculated using the same model parameters as described previously and assuming a BSE bulk composition; with phase compositions determined from previous experiments (Irifune, 1994). Equations of state data and properties are referred in **Table 5.3.2.3**. The calculations are performed following the geotherm of Brown and Shankland (1981). The V_p acoustic impedances were calculated from the modeled velocities V_p and densities ρ :

$$Z = V_p \rho \quad (5.3.2.2)$$

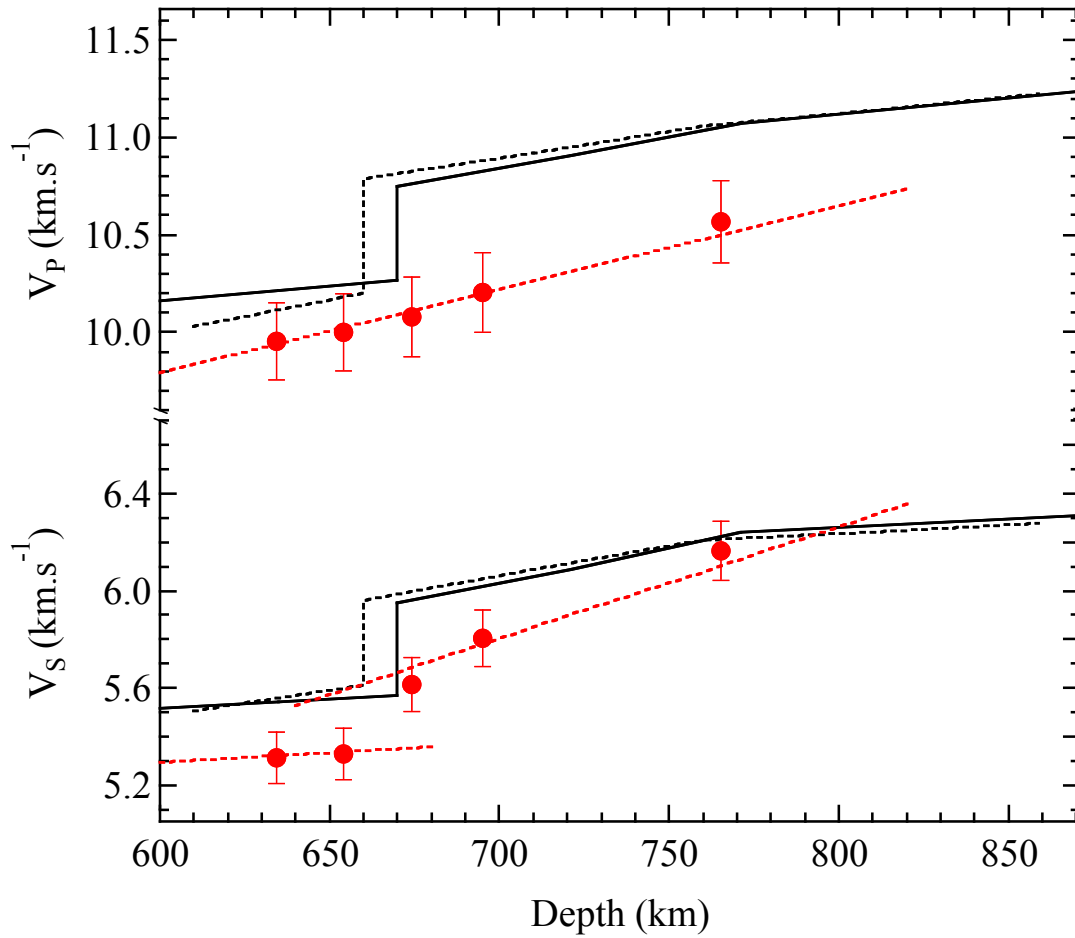


Figure 5.3.2.1.1: Estimates for V_s and V_p of a BSE bulk composition around the 660km discontinuity. Modeled compositions are shown as the red dot calculated at the pressures and temperatures corresponding to the 600-800km depths indicated. Data for $(Mg,Fe)(Al,Si)O_3$ perovskites and garnets are taken from the equation of state model determined in this study, while models for the other phases are taken from the literature. The continuous and dashed black curves show respectively PREM and AK135 seismic reference models for this region.

In **Figure 5.3.2.1.2**, a gradual change in the values of acoustic impedance between the transition zone (<660 km) and the upper part of the lower mantle (>660 km) is observed rather than a sharp discontinuity. However the sharp discontinuity predicted by the seismic reference models at 660 km depth is not present in term of acoustic

impedance. For the 660 km discontinuity, the shear impedance contrasts range from 9.1 to 14.9%, roughly consistent with earlier studies of *ScS* reverberations (Revenaugh and Jordan, 1991) and *SS* precursors (Estabrook and Kind, 1995), which suggested shear impedance changes at 660 km of $14.4 \pm 2\%$ and $9.9 \pm 1.5\%$, respectively. The absence of a jump in the V_p acoustic impedance values will result in the lack of underside reflections of the compressional seismic waves at this depth. This estimation is perfectly in agreement with the seismic observations (Estabrook and Kind, 1995; Flanagan and Shearer, 1998; Houser *et al.*, 2008; Shearer and Flanagan, 1999). V_p jump at 660 km predicted in previous pyrolite mantle models (Weidner and Wang, 1998) are substantially larger than our calculated values, but would be in poor agreement with the observed lack of *PP* underside reflections.

High temperature thermo-elastic properties have been refined for the Fe-Al perovskite samples studied here, using the thermodynamically consistent formulation of Stixrude and Lithgow-Bertelloni (2005) described in §2.5. Two of the refined high temperature parameters are quite different to previous estimates and have important influences on V_p and V_s . Although the data presented here provide the first opportunity to refine these terms for Fe-Al perovskites, they can only be refined over the relatively narrow range of pressures over which the high temperature data were collected (22-24 GPa). Changes in the magnitude of these terms at higher pressures would have significant effect on the modeled velocities.

Of the refined parameters, high-temperature measurements of the bulk modulus are sensitive to q_0 (equation 2.5.13) as a result, V_p is much more sensitive to the refined values of q_0 than V_s . Values of $q_0 > 2$ have been found in static *P-V-T* data for MgSiO_3 perovskite (Stixrude *et al.*, 1992; Shim and Duffy, 2000), but the values refined here for this term are in the range 4-5. As an example of the importance of this term if the current model, were recalculated with a lower value of $q_0 = 2$, V_p of 4% Fe-Al perovskite at 660 km will increase by about 4% while the effect on V_s will be negligible (<1% increase). On the other hand, η_{s_0} influences only the shear elasticity (equation 2.5.14). In this study, for the 4% Fe^{3+} and Al perovskite, was found a refined value of $\eta_{s_0} = 1.9$. Stixrude and Lithgow-Bertelloni (2005) compiled $\eta_{s_0} = 2.6$ and 2.1, respectively for the perovskite

end-members MgSiO_3 and FeSiO_3 . If one uses $\eta_{s_0} = 1.9$ in our model, then, V_S decreases by 2% and V_P only by less than 1%.

In the model calculation shown in **Figure 5.3.2.1.1**, the calculated V_P exhibits a trend without a jump at 660 km depth, related to the behavior of the Fe- and Al- bearing magnesium silicate perovskite, which is the main component. The breakdown of phases and appearance of new ones in the 660 km discontinuity region have little influence on V_P in the model proposed here. The low values for V_P of 4% Fe-Al perovskite are due to the low bulk modulus $K_S = 221$ GPa, however, the higher refined K' causes the K to increase more rapidly with pressure. As described previously, the bulk modulus is sensitive to q_0 and the low values of V_P calculated at 660 km are mainly a consequence of the refined magnitude of q_0 , i.e. it is the large temperature dependence of the perovskite V_P which mainly accounts for the low determined values of V_P at 660 km. Due to the magnitude of q_0 , the higher the temperature the lower V_P will be in comparison to, for example, PREM. For this reason models calculated at lower temperatures do result in the appearance of a 660 km discontinuity, although not at temperatures considered compatible with the an average mantle adiabat at these conditions.

Deuss *et al.* (2006) also found that the variations in $S660S/SS$ and $P660P/PP$ amplitudes they observed, and even the absence of $P660P$ in certain regions, might be explained by changes in temperature or Al content for a pyrolite mantle composition (Weidner and Wang, 1998). This is also in agreement with the model presented here as low Fe-Al bearing perovskite is predicted to have a higher V_P at 660 km. In regions where they found reflections from the 660 km discontinuity in PP , the amplitudes correspond very well with amplitudes predicted by a model with 5% Al and a 1700 K geotherm. Increasing the temperature to a 1900 K geotherm explains regions where reflections from the 660 km discontinuity are not found in PP .

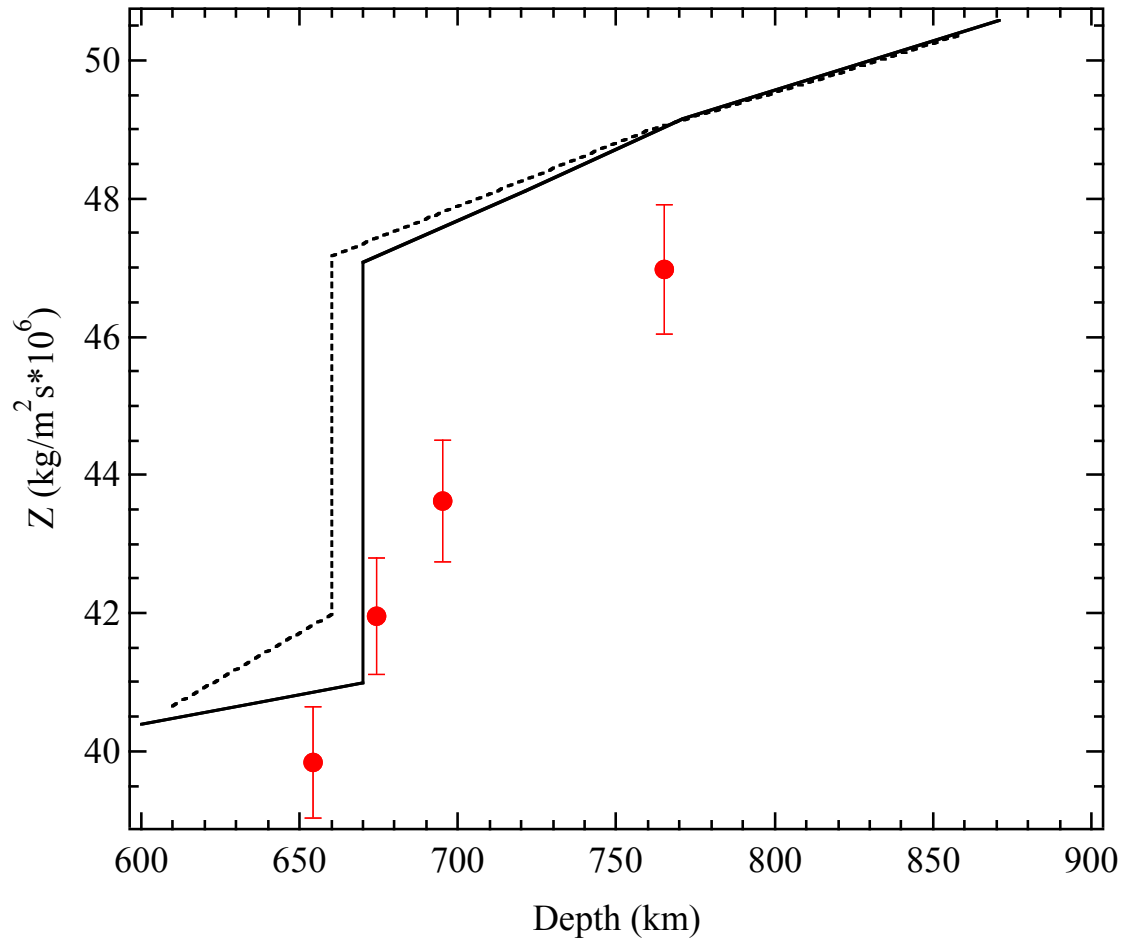


Figure 5.3.2.1.2: Estimates for Z of the same BSE bulk composition as in Figure 5.3.2.2.1. The solid and dashed curves show PREM and Ak135 seismic reference models for the 660km discontinuity.

5.3.2.2 Implications for the lower mantle

///

The modeled P- and S- waves velocities of §5.3.2.1 have been extrapolated further for the same composition in the upper part of the lower mantle using the same data (Table 5.3.2.3). The calculations were performed from 771 km to 1071 km to compare the model estimates of the seismic wave velocities with the seismic reference models. The model is not extended to greater depth than this because of the anomalous velocity change observed for $(\text{Mg}_{0.92}\text{Fe}_{0.08})\text{O}$ ferropericlase at around 40–60 GPa, which is

attributed to the iron spin crossover (Murakami *et al.*, 2012). The chemical composition of each phase is still based on the same pyrolite mantle composition (Irifune, 1994). Equations of state data and properties are listed in **Table 5.3.2.3**. The calculations are performed following the geotherm of Brown and Shankland (1981). In **Figure 5.3.2.2.1**, the modeled velocities are compared with the seismic reference models PREM (Dziewonski and Anderson, 1981) and Ak135 (Kennett *et al.*, 1995). The model calculation for V_S are in a perfect agreement with the seismic reference models at 770 km depth and remain consistent with it up to depth as great as 1071 km. It appears as if it is gradually deviating from the lower mantle values at depths greater than 1000 km. Along the whole calculated range, V_P remains 3 to 4% slower than the seismic reference models.

The lower mantle has been conventionally been considered to be peridotitic in composition, with an Mg/Si ratio of 1.3. The same ratio is found in the upper mantle, which is dominated by $(\text{Mg,Fe})_2\text{SiO}_4$ olivine (Ringwood, 1975). However, this Mg/Si ratio is significantly higher than that of chondritic meteorites ($\text{Mg/Si} < 1.0$), which are usually assumed to be similar in composition to the materials from which Earth formed. The apparent depletion of silicon in the mantle (the ‘missing silicon’ problem) has provoked much debate that the shortfall is balanced by the presence of silicon in the core or relative silicon enrichment in the lower mantle (Allegre *et al.*, 1995). Such chemical stratification in the mantle should have occurred during the solidification of the massive magma ocean at the very beginning of Earth’s history. Subsequent solid-state convection tends to homogenize the mantle, but the primordial chemical stratification may still be preserved today. This issue is strongly related to the sort of convection that took place in the mantle throughout Earth’s history (Tonks and Melosh, 1993). It has also been proposed that Earth formed preferentially from meteorites with higher Mg/Si ratios owing to the possible radial chemical zonation in the Solar System (Ringwood, 1989).

Murakami *et al.* (2012) results indicate that the conventional peridotitic mantle model is not compatible with the seismic properties of the lower mantle, and strongly suggest that the lower mantle is dominated by perovskite (93 vol%) and would therefore be silica-rich by comparison with the upper mantle. Following this model, the lower mantle would be chemically distinct, with a near-chondritic Mg/Si ratio (1.0), which reasonably explains the ‘missing silicon’ problem. Using Murakami *et al.* (2012)

estimated phase proportions; our modeled V_P and V_S remain on the same trend as the one reported in **Figure 5.3.2.1.2** within $<0.1\%$ changes. When considering a lower mantle fully composed of perovskite, V_P and V_S remain unchanged. There is a lack of high pressure and high temperature data for CaSiO_3 perovskite at lower mantle conditions (**Table 5.3.2.3**). However the thermo-elastic parameters defining this mineral allow predicting its V_P and V_S under elevated P - T conditions. In addition to that, the proportion of CaSiO_3 perovskite predicted never exceed 10 vol%, and such proportion would have a negligible effect on modeled mantle velocities. Following the model developed here, the variations in the volume proportions of Mg-Pv, ferropericlase, and CaSiO_3 perovskite, in the range of the different mineralogical models (e.g. Irifune, 1994; Murakami et al. 2012), cannot explain the observed discrepancy in V_P between the model and the seismic reference models.

The Fe and Al contents of Mg-Pv increase with increasing pressure to 30 GPa, whereas the Mg and Si contents of Mg-Pv decrease concomitantly. Both Mg and Fe in ferropericlase were found to decrease with increasing pressure in this range. Considering an earlier study using the quench methods at pressures up to 28 GPa (Irifune, 1994), the volume proportions of Mg-Pv, ferropericlase, and CaSiO_3 perovskite do not change with pressure and remain at $\sim 74\%$, 16%, and 10%, respectively. A large zero-pressure thermal expansion coefficient obtained on $(\text{Fe,Mg})\text{SiO}_3$ perovskite by Zhang and Weidner (1999), would suggest a layered mantle, with a lower mantle that is either more Fe-rich (Knittle *et al.*, 1986) or more Si-rich (Stixrude *et al.*, 1992) than a pyrolitic upper. Our data suggest that the bulk modulus of Al and Fe-enriched perovskite would be significantly lower at lower mantle conditions than that of the pure Mg-Pv. As a result, V_P and V_S of perovskite will be lower as well. Lower contents of Fe and/or Al would be a possible explanation for the misfit between V_P of the model developed here and the seismic reference models in the lower mantle. A smaller substitution of Fe and Al, in the perovskite structure will raise V_P to higher values, and as a consequence, the model will match better with the seismic reference models. This hypothesis is supported by the study of Saikia *et al.* (2009), which reported that for lower mantle perovskite there will be a strong compositional dependence to density in upper regions of the lower mantle, with perovskites formed from basaltic material being significantly denser than those formed in

the primitive mantle but a substantial decrease in this contrast occurs with increasing depth. A strong increase in bulk sound velocity is also predicted with increasing depth, which would make V_P faster and in this case again, getting closer to the seismic reference models.

The model contains eight material-specific parameters that are required to compute physical properties. As discussed previously, one of these parameters, q_0 , has a considerable effect on V_P , while this effect is much more moderated on V_S . Previous theoretical and experimental studies have also found that q_0 decreases significantly with compression (Agnon and Bukowinski, 1990; Speziale *et al.*, 2001). Values of $q_0 > 2$ have been found in static P - V - T data for MgSiO_3 perovskite (Stixrude *et al.*, 1992; Shim and Duffy, 2000), and Xu *et al.* (2008) use $q_0 = 1.4$. However, in this study q is refined for pressure and temperature conditions encompassing only the upper part of the lower mantle, where the magnesium silicate perovskite starts to be stable. The thermal properties of this mineral might evolve from the conditions at the edge of the stability field to the stability field of the perovskite itself. One might, therefore, imagine that q_0 has a much higher value at the edge of the stability field of perovskite, as calculated in this study ($q_0 = 4.6$), than in the rest of the lower mantle (Stixrude *et al.*, 1992; Shim and Duffy, 2000; Xu *et al.*, 2008). A decrease in q_0 , with the increasing pressure, would result in a significant increase of V_P of the 4% Fe^{3+} and Al perovskite and a slight increase of V_S . For both V_P and V_S , those evolutions would bring the modeled pyrolite mantle composition closer to the seismic reference models. However to check this assertion would require data to be collected on Fe-Al perovskite at high temperatures but at pressures significantly greater than 25 GPa. This would be possible for example if sintered diamond cubes could be used in a multianvil in conjunction with ultrasonic travel time measurements.

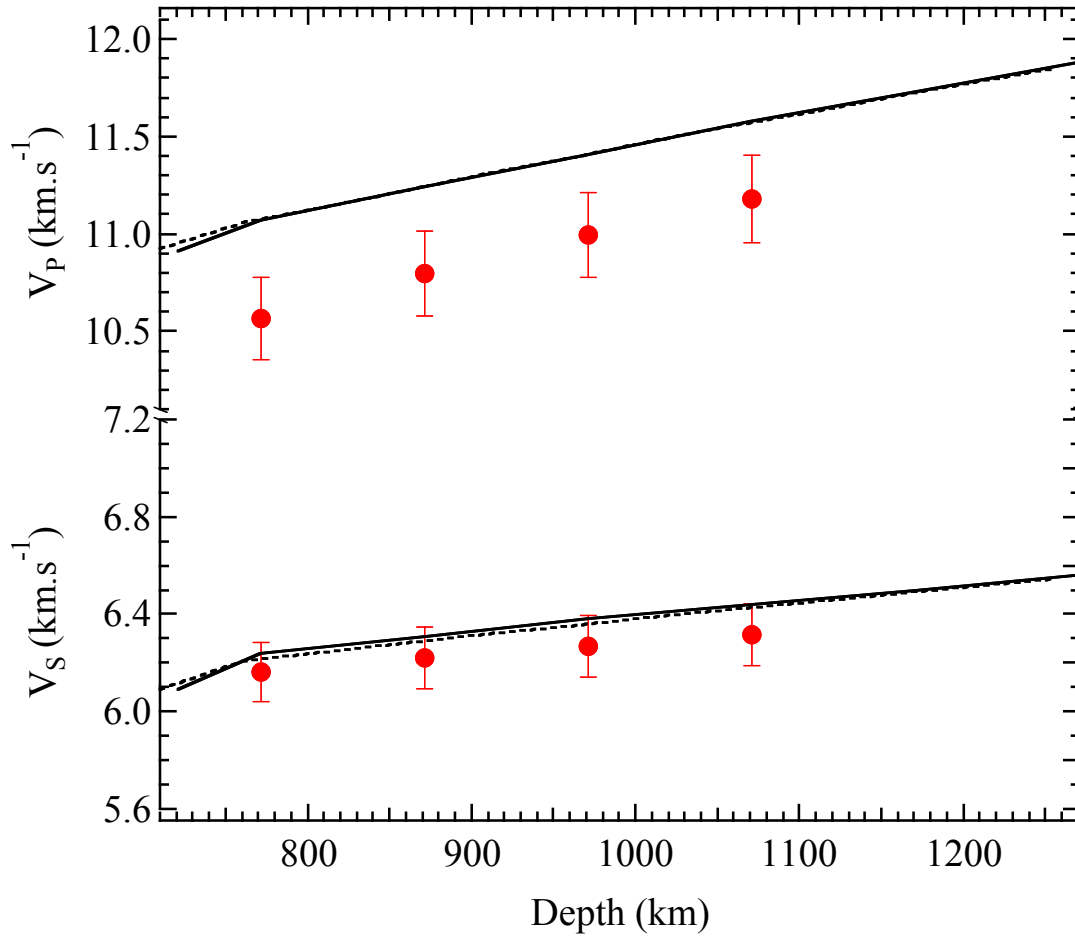


Figure 5.3.2.2.1: Estimates for V_s and V_p of a BSE bulk composition comprising $(Mg,Fe)(Si,Al)O_3$ perovskite, $(Mg,Fe)O$ ferropericlase and $CaSiO_3$ perovskite are shown as the red filled circles and their associated errors calculated at the pressures and temperatures corresponding to the lower mantle depths indicated. Data for $(Mg,Fe)(Si,Al)SiO_3$ perovskite are taken from the equation of state model determined in this study, while models for the other phases are taken from the literature. The solid and dashed curves show PREM and AK135 seismic reference models for the lower mantle.

6. Conclusion and perspectives

During this study, the elastic properties of lawsonite, the garnet group and Fe- and Al-bearing magnesium silicate perovskite have been investigated under Earth's mantle relevant pressure and temperature conditions.

1. A MHz ultrasonic interferometer with both compressional and shear-waves capabilities has been adapted for high-pressure and high-temperature elasticity measurements in a multi-anvil apparatus. The phase comparison method was used for measurements at room temperature at the Bayerisches Geoinstitut and the European Synchrotron Radiation Facility (ESRF). The pulse echo overlap method was employed during the experiments at high temperatures in conjunction with synchrotron radiation at the Advanced Photon Source (APS).

By combining ultrasonic measurements with the x-ray diffraction and x-radiography techniques now available at synchrotron facilities (APS and recently at ID06, ESRF), simultaneous measurements of travel times, sample length and unit-cell volume, temperature, and pressure were obtained. It is now possible to perform high-frequency (10- to 70-MHz) measurements of both P and S wave velocities with a precision of 0.3% on millimetre-sized polycrystalline samples to pressures of 25 GPa and simultaneous temperatures 1200 K (Chantel *et al.*, 2012b).

2. High-pressure ultrasonic interferometric measurements have been conducted to gain insight into the elastic properties of lawsonite $[\text{CaAl}_2(\text{Si}_2\text{O}_7)(\text{OH})_2 \cdot \text{H}_2\text{O}]$, a hydrous mineral phase stabilized under cold subduction zone conditions. Lawsonite was found to have an unusually low shear modulus at high pressure and its formation in subducted oceanic crust can explain some seismic evidence for LVL at depths exceeding 100 km.

To approach estimated LVL velocities requires lawsonite to form in the subducting crust as a result of a fluid influx due to the breakdown of other hydrous minerals such as serpentine. The formation of lawsonite additionally lowers seismic velocities because it forms at the expense of garnet, a mineral with relatively fast seismic velocities. LVL observations may therefore be used to place constraints on the amount of

H₂O subducted into the deep mantle (Chantel *et al.*, 2012a).

3. It seems that garnet elastic properties can be determined from the end members with an accuracy that is generally within experimental uncertainties. There seems to be no evidence that large excess properties exist that cause non-linear contributions to multicomponent elastic properties for the mineral garnet.

Deviation between the two calculated mantle models is about 3% for both V_P and V_S , with the modeled slab composition being slower. Within the uncertainties of the seismic data therefore a pyrolite mantle composition is quite consistent with velocities at the base of the transition zone. Relatively low temperatures and olivine-rich nature of the stagnant slab support that there would be few grounds for arguing that significant accumulation of MORB composition material occurs at the base of the transition zone.

4. Data for Mg-Pv are consistent with previous studies and the (Mg, Fe)-Pv sample has almost identical shear properties to Mg-Pv. The adiabatic bulk modulus, K_S , for (Mg, Fe)-Pv, however, is found to be substantially lower than for Mg-Pv, with a refined value of 236 GPa and a pressure derivative of 4.7. It is proposed that low K_S values result from a change in the elasticity of Fe-bearing perovskite at low pressures <30-40 GPa. High temperature data are in agreement with recent models and it is shown that the obtained elastic properties of (Mg, Fe)-Pv are not inconsistent with a lower mantle of bulk silicate Earth composition (Chantel *et al.*, 2012b).

The low visibility of underside PP reflections from 660 km discontinuity means that the velocity contrasts at this depth are much lower than expected for the seismic reference models. This leads to the proposition that there is only a small change in bulk modulus across the 660 km boundary as shown in this study.

The model calculation for V_S is in a perfect agreement with the seismic reference models to depth as great as 1071 km, while V_P remains 3 to 4% lower at lower mantle conditions. A possible explanation for the discrepancy observed between the modeled V_P and the seismic reference models is q , the volume dependence of the Grüneisen parameter. The thermal properties of magnesium silicate perovskite might evolve when considered at the edge of its stability field and within the stability field of the perovskite. The variations in the thermal properties of perovskite may result in the observed gradual change in the modeled V_P at the 660km discontinuity and in the upper part of the lower

mantle.

To further pursue this study, I will study elastic properties of magnesium silicate perovskite with a BSE composition representing the bulk silicate Earth and investigate the effect of various Fe and Al contents in the perovskite composition, which can be attributed as a source of geochemical variability in the lower mantle. The aim is to understand whether Fe and Al have an effect on lowering perovskite velocities and to examine the role of the cation substitution mechanism in this effect.

First, a double-stage pressure generation configuration and 6/2 (i.e., 6 mm octahedral edge length and 2 mm anvil truncation edge length) multianvil assembly will be employed, which can be capable of reaching P-T conditions of 30 GPa and 1800K using WC anvils and then extend the pressure and temperature conditions up to 50 GPa and 2000K using sintered diamond anvils.

The acquired S and P-wave velocities and density data will be used to model the effects of chemical variations on seismic variability in the lower mantle relative to 1-D seismological models. Analysis of these new data will allow us to determine if S and P velocities of a pyrolitic mantle are too low to account for lower mantle velocities and to examine whether the lower mantle may in fact be composed mainly of perovskite.

References

- Abers, G.A., Sarker, G., 1996. Dispersion of regional body waves at 100-150 km depth beneath Alaska: in situ constraints on metamorphism in the subducted crust. *Geophys. Res. Lett.* **23**, 1171-1174.
- Abers, G.A., 2000. Hydrated subducted crust at 100-250 km depth. *Earth Planet. Sci. Lett.* **176**, 323-330.
- Abramson, E.H., Brown, J.M., Slutsky, L.J., 1999. Application of impulsive stimulated scattering in the Earth and planetary sciences. *Annu. Rev. Phys. Chem.* **50**, 279-313.
- Agnon, A., Bukowinski, M.S.T., 1990. Thermodynamic and elastic properties of a many-body model for simple oxides, *Phys. Rev. B*, 41(11), 7755–7766.
- Akaogi, M., Akimoto, S., 1997. Pyroxene-garnet solid solution equilibria in the system $Mg_4Si_4O_{12}$ – $Mg_3Al_2Si_3O_{12}$ and $Fe_4Si_4O_{12}$ – $Fe_3Al_2Si_3O_{12}$ at high pressures and temperatures. *Phys. Earth Planet. Inter.* **15**, 90-106.
- Allegre, C.J., Poirier, J.P., Humler, E., Hofmann, A.W., 1995. The chemical composition of the earth. *Earth Planet. Sci. Lett.* **134**, 515–526.
- Anderson, O.L., Issak, D.G., Yamamoto, S., 1989. Anharmonicity and the equation of state for gold. *J. Appl. Phys.* **65**, 1534–1543.
- Andraut, D., Bolfan-Casanova, N., Guignot, N., 2001. Equation of state of lower mantle (Al,Fe)- $MgSiO_3$ perovskite. *Earth Planet. Sci. Lett.* **193**, 501-508.
- Aoki, I., Takahashi, E., 2004. Density of subducted oceanic crust (MORB) in the upper mantle. *Phys. Earth Planet. Int.*, 143–144, pp. 129–143
- Bina, C. R., Kawakatsu, H., 2010. Buoyancy, bending, and seismic visibility in deep slab stagnation, *Physics of the Earth and Planetary Interiors*, **183**, 330-340, doi:10.1016/j.pepi.2010.04.010.
- Birch, F., 1952. Elasticity and constitution of the Earth's interior, *J. Geophys. Res.*, **57**, 227-286.
- Bascou, J., Barruol, G., Vauchez, A., Mainprice, D., Egydio-Silva, M., 2001. EBSD-measured lattice-preferred orientations and seismic properties of eclogites. *Tectonophysics* **342** (1-2), 61-80.
- Bass, J.D., Parise, J.B., 2008. Deep Earth and recent developments in mineral physics. *Elements*, **4**, 157-163.
- Bassett, W.A. & Brody, E.M., 1977. Brillouin Scattering: A new way to Measure Elastic Moduli at High Pressures. In: Manghnani, M.H. & Akimoto, S. (Eds.) *High Pressure Research - Applications in Geophysics*, New York, 519-532.
- Bezacier, L., Reynard, B., Bass, J.D., Wang, J., Mainprice, D., 2010. Elasticity of glaucophane, seismic velocities and anisotropy of the subducted oceanic crust. *Tectonophysics* **494** (3-4), 201-210.
- Birch, F., 1978. Finite strain isotherm and velocities for single-crystal and polycrystalline NaCl at high-pressure and 300 K. *J. Geophys. Res.* **83**, 1257-1268.

- Boffa Ballaran, T., Angel, R.J., 2003. Equation of state and high-pressure phase transitions in lawsonite. *Eur. J. Mineral.* **15**, 241-246.
- Boffa Ballaran, T., Kurnosov, A., Glazyrin, K., Frost, D.J., Merlini, M., Hanfland, M., Caracas, R., 2012. Effect of chemistry on the compressibility of silicate perovskite in the lower mantle. *Earth Planet. Sci. Lett.* 333-334, 181-190.
- Brown, J.M., Shankland, T.J., 1981. Thermodynamic parameters in the Earth as determined from seismic profiles. *Geophys. J. R. Astron. Soc.*, 66, 579–596.
- Cammarano, F., Deuss, A., Goes, S., Giardini, D., 2005. One-dimensional physical reference models for the upper mantle and transition zone: Combining seismic and mineral physical constraints. *Journal of Geophysical Research* **110**, B01306, doi:10.1029/2004JB003272
- Chai, M., Brown, J.M., Slutsky, L.J., 1997. The elastic constants of a pyrope - grossular - almandine garnet to 20 GPa. *Geophys. Res. Lett.* **24**, 523-526.
- Chantel J., Mookherjee M., Frost D.J., 2012a. The elasticity of lawsonite at high pressure and the origin of low velocity layers in subduction zones. *Earth Planet. Sc. Lett.* doi:10.1016/j.epsl.2012.06.034.
- Chantel, J., Frost, D. J., McCammon, C. A., Jing, Z., Wang, Y., 2012b. Acoustic velocities of pure and iron-bearing magnesium silicate perovskite measured to 25 GPa and 1200K, *Geophys. Res. Lett.*, doi:10.1029/2012GL053075, in press.
- Chen, G., Cooke, G.D., Gwanmesia, G.D., Liebermann, R.C., 1999. Elastic wave velocities of $Mg_3Al_2Si_3O_{12}$ -pyrope garnet to 10 GPa. *Am. Mineral.* **84**, 384-388.
- Chinnery, N., Pawley, A.R., Clark, S.M., 2000. The equation of state of lawsonite to 7 GPa and 873 K, and calculation of its high-pressure stability. *Am. Min.* **85**, 1001-1008.
- Christensen, N.I., 1972. Compressional and shear wave velocities at pressures to 10 kilobars for basalts from the East Pacific rise. *Geophys. J. R. Astr. Soc.* **28**, 425-429.
- Christensen, U.R., Yuen D.A., 1985. Layered convection induced by phase transitions, *J. Geophys. Res.*, 90(B12), 10,291–10,300.
- Christensen, U.R., Hofmann, A.W., 1994. Segregation of subducted oceanic crust in the convecting mantle. *J. Geophys. Res.* 99, 19867–19884.
- Cook, R.K., 1957. Variation of elastic constants and static strains with hydrostatic pressure: a method for calculation from ultrasonic measurements. *J. Acoust. Soc. Am.* **29**, 445-449.
- Creager, K.C., Jordan, T.H., 1984. Slab penetration into the lower mantle. *J. Geophys. Res.* **89**, 3031-3049.
- Creager, K.C., Jordan, T.H., 1986. Slab penetration into the lower mantle beneath the Mariana and other island arcs of the Northwest Pacific. *J. Geophys. Res.* **91**, 3573-3589.
- Daniel, I., Fiquet, G., Gillet, P., Schmidt, M.W., Hanfland, M., 1999. P-V-T equation of state of lawsonite. *Phys. Chem. Minerals.* **26**, 406-414.
- Davies, D., McKenzie, D.P., 1969. Seismic travel-time residuals and plates. *Geophys. J. R. Astr. Soc.* **18**, 51-63.
- Davies, G. F., Dziewonski, A. M., 1975. Homogeneity and constitution of the Earth's lower mantle and

- outer core, *Phys. Earth Planet. Inter.*, 10, 336 – 343.
- Davies, G.F., O'Connell, R.J., 1977. Transducer and bond phase shifts in ultrasonics and their effects on measured pressure derivatives of elastic moduli. In: M. Manghnani and S. Akimoto (Eds.), *High Pressure Research: Application in Geophysics*. Academic Press, New York, 533-562.
- Deschamps, F., Trampert, J., 2004. Towards a lower mantle reference temperature and composition, *Earth Planet. Sci. Lett.* 222, 161–175.
- Decker, D.J., 1971. High-pressure equation of state for NaCl, KCl, and CsCl. *J. Appl. Phys.* 42, 3239–3244.
- Deuss, A., Redfern, S.A.T., Chambers, K., Woodhouse, J.H., 2006. The Nature of the 660-Kilometer Discontinuity in Earth's Mantle from Global Seismic Observations of PP Precursors, *Science*, 311 (5758), 198-201.
- Weidner, D., Swyler, K. and Carleton, H. 1975. Elasticity of Microcrystals. *Geophysical Research Letters*, 2, 189-192.
- Dziewonski, A.M., Anderson, D.L., 1981. Preliminary reference Earth model. *Phys. Earth Planet. Inter.* **25**, 297-356.
- Estabrook, C.H., Kind, R., 1995. The Nature of the 660-Kilometer Upper-Mantle Seismic Discontinuity from Precursors to the PP Phase. *Science* 274, pp. 1179-1182.
- Faul, U.H., Toomey, D.R., Waff, H.S., 1994. Intergranular basaltic melt is distributed in thin, elongated inclusions. *Geophys. Res. Lett.* **21**, 29-32.
- Fiquet, G., Dewaele, A., Andrault, D., Kunz, M., Le Bihan, T., 2000. Thermoelastic properties and crystal structure of MgSiO₃ perovskite at lower mantle pressure and temperature conditions. *Geophys. Res. Lett.* 27, 21–24.
- Fischer, K.M., Creager, K.C., Jordan, T.H., 1991. Mapping the Tonga slab. *J. Geophys. Res.* **96**, 14 403-14 427.
- Flanagan, M.P., Shearer, P.M., 1998. Global mapping of topography on transition zone velocity discontinuities by stacking SS precursors, *J. Geophys. Res.*, 103, 2673-2692.
- Fuis, G.S., Elizabeth, L.A., Mooney, W.D., Christensen, N.I., Geist, E., 1991. Crustal structure of accreted terranes in southern Alaska, Chugach mountains and Copper River, from seismic refraction results. *J. Geophys. Res.* **96**, 4187-4227.
- Fujimoto, Y., Kono, Y., Hirajima, T., Kanagawa, K., Ishikawa, M., Arima, M., 2010. P-wave velocity and anisotropy of lawsonite and epidote blueschists: Constraints on water transportation along subducting oceanic crust. *Phys. Earth. Planet. Inter.*, **183**, 219-228.
- Ganguly, J., Cheng, W., Tirone, M., 1996. Thermodynamics of aluminosilicate garnet solid solution : new experimental data, an optimized model, and thermometric applications. *Contrib. Miner. Petrol.* 126, 137-151.
- Goto, T., Anderson, O.L., Ohno, I., Yamamoto, S., 1989. Elastic constants of corundum up to 1825 K. *J. Geophys. Res.* **94**, 7588-7602.

- Gubbins, D., Snieder, R., 1991. Dispersion of P waves in subducted lithosphere: evidence for an eclogite layer. *J. Geophys. Res.* **96**, 6321-6333.
- Gubbins, D., Barnicoat, A., Cann, J., 1994. Seismological constraints on the gabbro-eclogite transition in subducted oceanic crust. *Earth Planet. Sci. Lett.* **122**, 89-101.
- Gwanmesia, G.D., Chen, G., Liebermann, R.C., 1998. Sound velocities in MgSiO_3 -garnet to 8 GPa. *Geophys. Res. Lett.* **25**, 4553-4556.
- Gwanmesia, G.D., Zhang, J., Darling, K., Kung, J., Li, B., Wang, L., Neuville, D.R., Liebermann, R.C., 2006. Elasticity of polycrystalline pyrope ($\text{Mg}_3\text{Al}_2\text{Si}_3\text{O}_{12}$) to 9 GPa and 1000 C. *Phys. Earth Planet. Inter.* **155**, 179-190.
- Gwanmesia, G.D., Wang, L., Triplett, R., Liebermann, R.C., 2009. Pressure and temperature dependence of the elasticity of pyrope-majorite [$\text{Py}_{60}\text{Mj}_{40}$ and $\text{Py}_{50}\text{Mj}_{50}$] garnets solid solution measured by ultrasonic interferometry technique. *Phys. Earth and Planet. Interiors*, **174**, 105-112.
- Hacker, B.R., 1996. Eclogite formation and the rheology, buoyancy, seismicity, and H_2O content of oceanic crust, in: G.E. Bebout, D.W., Scholl, S.H., Kirby, J.P., Platt (Eds.), *Subduction Top to Bottom*. *Geophys. Monogr.* **96**, American Geophysical Union, 337-346.
- Hacker, B.R., Abers, G.A., 2004. An Excel worksheet and macro for calculating the densities, seismic wave speeds, and H_2O contents of minerals and rocks at pressure and temperature, *Subduction Factory 3*. *Geochem. Geophys. Geodyn. (G3)*, **5**, Q01005, doi:10.1029/2003GC000614.
- Helffrich, G., Stein, S., 1993. Study of the structure of the slab mantle interface using reflected and converted seismic waves. *Geophys. J. Int.* **115**, 14-40.
- Helffrich, G., 1996. Subducted lithospheric slab velocity structure: observations and mineralogical inferences, in: G.E. Bebout, D.W., Scholl, S.H., Kirby, J.P., Platt (Eds.), *Subduction Top to Bottom*. *Geophys. Monogr.* **96**, American Geophysical Union, 215-222.
- Helffrich, G., Abers, G.A., 1997. Slab low-velocity layer in the eastern Aleutian subduction zone. *Geophys. J. Int.* **130**, 640-648.
- Helffrich, G., Wood, B., 1996. 410 km discontinuity sharpness and the form of the olivine - phase diagram: Resolution of apparent seismic contradictions, *Geophys. J. Int.*, v.126, F7-F12.
- Hirose, K., Fei, Y., 2002. Subsolvus and melting phase relations of basaltic composition in the uppermost lower mantle. *Geochim. Cosmochim. Acta* **66**, 2099.
- Houser, C., G. Masters, M. Flanagan, and P. Shearer, 2008. Determination and analysis of long-wavelength transition zone structure using SS precursors, *Geophys. J. Int.*, **174**, 178-194, doi: 10.1111/j.1365-246X.2008.03719.x.
- Irifune, T., 1987. Experimental investigation of the pyroxene-garnet transformation in a pyrolite composition and its bearing on the constitution of the mantle. *Earth Planet. Sci. Lett.* **177**, 101-110.
- Irifune, T., Ringwood, A.E., 1987. Phase transformation in primitive MORB and pyrolite compositions to 25 GPa and some geophysical Implications. In: Manghnani, M.H., Syono, Y. (Eds.), *High Pressure*

- Research in Mineral Physics, **39**. TERRAPUB Tokyo/American Geophysical Union, Washington, DC, 235-246.
- Irifune, T., 1994. Absence of an aluminous phase in the upper part of the Earth's lower mantle. *Nature* **382**, pp 131-133.
- Irifune, T., Higo, Y., Inoue, T., Kono, Y., Ohfuji, H., Funakoshi, K., 2008. Sound velocities of majorite garnet and the composition of the mantle transition zone. *Nature*, **451**, 814-817.
- Irifune, T., Shinmei, T., McCammon, C.A., Miyajima, N., Rubie, D.C., Frost, D.J., 2010. Iron partitioning and density changes in pyrolite in Earth's lower mantle. *Science*, **327**, 193-195.
- Isaak, D.G., Anderson, O.L., Goto, T., 1989. Measured elastic moduli of single-crystal MgO up to 1800 K. *Phys. Chem. Miner.* **16**, 704-713.
- Jackson, I., Niesler, H. and Weidner, D.J., 1981. Explicit correction of ultrasonically determined elastic wave velocities for transducer-bond phase shift. *J. Geophys. Res.* **86**, 3736-3748.
- Jacobsen, S.D., Smyth, J.R., Spetzler, H.A., Holl, C.A., Frost, D.J., 2004. Sound velocities and elastic constants of iron-bearing hydrous ringwoodite. *Phys. Earth Planet. Interiors* **143–144**, 47-56.
- Jacobsen, S.D., Reichmann, H.J., Kantor, A., Spetzler, H., 2005. A gigahertz ultrasonic interferometer for the diamond-anvil cell and high-pressure elasticity of some iron-oxide minerals. *In: J. Chen et al. (Eds.) Advances in High-Pressure Technology for Geophysical Applications*, 25-48, Elsevier, Amsterdam.
- Jiang, F.M., Speziale, S., Duffy T.S. 2004. Single-crystal elasticity of grossular- and almandine-rich garnets to 11 GPa by Brillouin scattering *J. Geophys. Res.*, **109** (B10), p. B10210
- Kantor, A., Jacobsen, S.D., Kantor, I.Y., Dubrovinsky, L.S., McCammon, C.A., Reichmann, H.J., Goncharenko, I.N., 2004. Pressure-induced magnetization in FeO: evidence from elasticity and Mossbauer spectroscopy. *Phys. Rev. Lett.* **93**, 215502, doi: 10.1103/PhysRevLett.93.215502.
- Karason, H., van der Hilst, R.D., 2001. Improving global tomography models of P-wavespeed I: incorporation of differential travel times for refracted and diffracted core phases (PKP,Pdiff). *J. Geophys. Res.* **106**, 6569-87.
- Kawakatsu, H., Watada, S., 2007. Seismic evidence for deep water transportation in the mantle. *Science*. **316**, 1468-1471.
- Kellogg, L.H., Hager, B.H., van der Hilst, R., 1999. Compositional stratification in the deep mantle. *Science* **283**, 1881-1884.
- Kennett B.L.N., Engdahl E.R., Buland R., 1995. Constraints on seismic velocities in the earth from travel times. *Geophys. J. Int.* **122**, 108-124.
- Keppler, H., Frost D.J., 2005. Introduction to minerals under extreme conditions, in: Miletich, R., (Ed.), *Mineral Behaviour at Extreme Conditions*. EMU Notes in Mineralogy, **7**, Eötvös University Press, Budapest, 1-30.
- Knittle, E., Jeanloz, R., Smith, G.L., 1986. Thermal Expansion of Silicate Perovskite and Stratification of the Earth's Mantle, *Nature* **319**, 214–215.

- Kono, Y., Gréaux, S., Higo, Y., Ohfuji, H., Irifune, T. 2010. Pressure and temperature dependences of elastic properties of grossular garnet up to 17 GPa and 1650 K, *J. Earth Sci.*, 21, 782–791, doi:10.1007/s12583-010-0112-2.
- Le Bail, A., Duroy, H., Fourquet, J.L., 1988. Ab Initio Structure Determination of LiSbWO_6 by X-ray Powder Diffraction. *Materials Research Bulletin* 23(3), 447-52.
- Li B., Jackson I., Gasparik T., Liebermann R.C., 1996. Elastic wave velocity measurement in multi-anvil apparatus to 10 GPa using ultrasonic interferometry. *Phys Earth Planet. Int.* 98, 79-91.
- Li B., Chen G., Gwanmesia G.D., Liebermann R.C., 1998. In *Properties of Earth and Planetary Materials at High Pressure and Temperature*, eds. Manghnani M, Yagi T (Am. Geophys. Union, Washington, DC), 41-61.
- Li, B., Zhang, J., 2005. Pressure and temperature dependence of elastic wave velocity of MgSiO_3 perovskite and the composition of the lower mantle. *Phys. Earth Planet. Int.* 151, 143-154.
- Libowitzky, E., Armbruster, T., 1995. Low-temperature phase transitions and the role of hydrogen in lawsonite. *Am. Min.* 80, 1277-1285.
- Liebermann, R.C., Ringwood, A.E., Mayson, D.J., Major A., 1975. Hot-pressing of polycrystalline aggregates at very high pressure for ultrasonic measurements. *Proceedings of the 4th International Conference on High Pressure, Kyoto*, 495-502.
- Lin, C.H., Huang, B.S., Rau, R.J., 1999. Seismological evidence for a low-velocity layer within the subducted slab of southern Taiwan. *Earth Planet. Sci. Lett.* 174, 231-240.
- Liu, J., Chen, G., Gwanmesia, G.D., Liebermann, R.C., 2000. Elastic wave velocities of pyrope-majorite garnets ($\text{Py}_{62}\text{Mj}_{38}$ and $\text{Py}_{50}\text{Mj}_{50}$) to 9 GPa, *Phys. Earth Planet. Inter.*, 120, 153–163.
- Mainprice, D., Le Page, Y., Rodgers, J., Jouanna, P., 2008. Ab initio elastic properties of talc from 0 to 12 GPa: Interpretation of seismic velocities at mantle pressures and prediction of auxetic behaviour at low pressures. *Earth Planet. Sci. Lett.* 274, 327-338.
- Mao, H.K., Hemley, R.J., Fei, Y., Shu, J.F., Chen, L.C., Jephcoat, A.P., Wu, Y., Basset, W.A., 1991. Effect of pressure, temperature and composition on the lattice parameters and density of three (Fe,Mg)SiO₃ perovskites up to 30 GPa, *J. Geophys. Res.* 96. B8069-B8079.
- Mao, Z., Lin, J.F., Scott, H.P., Watson, H.C., Prakapenka, V.B., Xiao, Y., Chow, P., McCammon, C., 2011. Iron-rich perovskite in the Earth's lower mantle. *Earth Planet. Sci. Lett.* 309, 179–184.
- Matsuzawa, T., Umino, N., Hasegawa, A., Takagi, A., 1986. Upper mantle velocity structure estimated from PS-converted wave beneath the north-eastern Japan Arc. *Geophys. J. R. Astron. Soc.* 86, 767-787.
- Matsuzawa, T., Umino, A., Hasegawa, A., Takagi, A., 1987. Estimation of the thickness of the low velocity layer at the surface of the descending oceanic plate beneath the Northeastern Japan arc by using synthesized PS-wave. *Tohoku. Geophys. J.* 31, 19-28.
- McCammon, C.A., Chaskar, V., Richards, G.G., 1991. A technique for spatially resolved Mössbauer spectroscopy applied to quenched metallurgical slags, *Meas. Sci. Tech.*, 2, 657-662.

- McCammon, C.A., 1998. The crystal chemistry of ferric iron in Fe_{0.05}Mg_{0.95}SiO₃ perovskite as determined by Mössbauer spectroscopy in the temperature range 80-293 K. *Phys Chem Minerals* **25**:292–300.
- McDonough, W.F., Sun, S.S., 1995. Composition of the Earth. *Chemical Geology* **120**: 223-253. doi: 10.1016/0009-2541(94)00140-4.
- Mutter, C., Mutter, J., 1993. Variations in thickness of layer 3 dominate oceanic crustal structure. *Earth Planet. Sci. Lett.* **117**, 295-317.
- Murakami, M., Sinogeikin, S.V., Bass, J.D., Sata, N., Ohishi, Y., Hirose K., 2007. Sound velocity of MgSiO₃ post-perovskite phase: A Constraint on the D'' discontinuity. *Earth Planet. Sci. Lett.* **259**, 18-23.
- Murakami, M., Sinogeikin V.S., Litasov K., Ohtani E., Bass D.J., 2008. Single-crystal elasticity of iron-bearing majorite to 26 GPa: Implications for seismic velocity structure of the mantle transitions zone. *Earth Planet. Sci. Lett.* **274**, 339-345.
- Murakami, M., Ohishi, Y., Hirao, N., Hirose, K., 2012. A perovskitic lower mantle inferred from high-pressure, high-temperature sound velocity data. *Nature*, **485**, 90-94.
- Nakajima, J., Tsuji, Y., Hasegawa, A., 2009. Seismic evidence for thermally-controlled dehydration reaction in subducting oceanic crust. *Geophys. Res. Lett.* **36**, L03303, doi:10.1029/2008GL036865.
- Nakajima, Y., Frost, D.J., Rubie D.C., 2012. Ferrous iron partitioning between magnesium silicate perovskite and ferropericlae and the composition of perovskite in the Earth's lower mantle, *J. Geophys. Res.*, doi:10.1029/2012JB009151.
- Newton, R.C., Wood, B.J., 1980. Volume behavior of silicate solid-solutions. *Am. Mineral.* Vol. 65, pp. 733-745.
- Niesler, H. and Jackson, I., 1989. Pressure derivatives of elastic wave velocities from ultrasonic interferometric measurements on jacketed polycrystals. *J. Acoust. Soc. Am.* **86**, 1573-1585.
- Okamoto, K., Maruyama, S., 1999. The high pressure stability limits of lawsonite in the MORB + H₂O system. *Am. Miner.* **84**, 362-373.
- Papadakis, E.P., 1990. Ultrasonic Measurement Methods (Physical Acoustics vol XIX) eds. R.N. Thurston and A.D. Pierce (San Diego: Pierce Academic Press) 81-123.
- Petricek, V., Dusek, M., Palatinus, L., 2006. Jana2006. The crystallographic computing system. Institute of Physics, Praha, Czech Republic.
- Pawley, A.R., Holloway, J.R., 1993. Water sources for subduction zone volcanism: New experimental constraints. *Science.* **260**, 664-667.
- Pawley, A.R., Redfern, S.A.T., Holland, T.J.B., 1996. Volume behavior of hydrous minerals at high pressure and temperature: I. Thermal expansion of lawsonite, zoisite, clinozoisite, and diaspore. *Am. Min.* **81**, 335-340.
- Peacock, S. M., 1993. The importance of blueschist-eclogite dehydration in subducting oceanic crust. *Geol. Soc. Am. Bull.* **105**, 684-694.

- Peacock, S.M., and Wang, K., 1999. Seismic consequences of warm versus cool subduction metamorphism: Examples from Southwest and Northeast Japan. *Science*. **289**, 937-939.
- Poirier, J.P., 1991. *Introduction to the Physics of the Earth's Interior*, Cambridge University Press.
- Revenaugh, J. S., Jordan, T. H., 1991. Mantle layering from ScS reverberations: 2. The transition zone, *J. Geophys. Res.*, 96, 19,763 – 19,780.
- Rigden, S.M., Jackson, I., Niesler, H., Liebermann, R.C., Ringwood, A.E., 1988. Pressure dependence of the elastic wave velocities for Mg₂GeO₄ spinel up to 3 GPa. *Geophys. Res. Lett.*, **15**, 604-608.
- Rigden, S.M., Gwanmesia, G.D., Jackson, I., Liebermann, R.C., 1992. Progress in high-pressure ultrasonic interferometry, the pressure dependence of elasticity of Mg₂SiO₄ polymorphs and constraints on the composition of the transition zone of the Earth's mantle. In: Y. Syono and M. Manghnani (Eds.), *High Pressure Research: Application to Earth and Planetary Sciences*. Terra Scientific Publishing Co. and American Geophysical Union, Tokyo and Washington, DC, 167-182.
- Rigden, S.M., Gwanmesia, G.D., Liebermann, R.C., 1994. Elastic wave velocities of a pyrope-majorite garnet to 3 GPa. *Physics of the Earth and Planetary Interiors*, 86, 35–44.
- Ringwood, A.E., Green, D.H., 1966. An experimental investigation of the gabbro-eclogite transformation and some geophysical implications. *Tectonophysics*. **3**, 383-427.
- Ringwood, A.E., 1967. The pyroxene–garnet transformation in the Earth's mantle. *Earth Planet. Sci. Lett.* **2**, 35-44.
- Ringwood, A.E., 1975. *Composition and petrology of the earth's mantle*. McGraw-Hill.
- Ringwood, A. E., 1989. Significance of the terrestrial Mg/Si ratio. *Earth Planet. Sci. Lett.* 95, 1–7.
- Ross, N.L., Hazen, R.M., 1990. High pressure crystal chemistry of MgSiO₃ perovskite. *Physics and Chemistry of Minerals*, 17, 228-237.
- Saikia, A., Boffa Ballaran, T., Frost D.J., 2009. The effect of Fe and Al substitution on the compressibility of MgSiO₃ perovskite determined through single-crystal X-ray diffraction. *Phys Earth Planet Int*, 173, 153-161.
- Schilling, F.R., Sinogeikin, S.V., Bass, J.D., 2003 Single-crystal elastic properties of lawsonite and their variation with temperature. *Phys. Earth Planet. Int.* **136**, 107-118.
- Schmidt, M.W., Poli, S., 1998. Experimentally based water budgets for dehydrating slabs and consequences for arc magma generation. *Earth Planet. Sci. Lett.* **163**, 361-379.
- Shearer, P.M., 1996. Transition zone velocity gradients and the 520-km discontinuity, *J. Geophys. Res.*, 101, 3053-3066, 1996.
- Shearer, P.M., Flanagan, M.P., 1999. Seismic velocity and density jumps across the 410- and 660-kilometer discontinuities, *Science*, 285, 1545-1548.
- Shim, S.H., Duffy, T.S., 2000. Constraints on the P-V-T equation of state of MgSiO₃ perovskite, *Am. Mineral.*, 85(2), 354–363.

- Sinmyo, R., Hirose, K., Nishio-Hamane, D., Seto, Y., Fujino, K., Sata, N., Ohishi, Y., 2008. Partitioning of iron between perovskite/post-perovskite and ferropericlase in the lower mantle, *J. Geophys. Res.*, *113*, B11204, doi:10.1029/2008JB005730.
- Sinogeikin, S.V., Schilling, F.R., Bass, J.D., 2000a. Single crystal elasticity of lawsonite. *Am. Mineral.* **85**, 1834-1837.
- Sinogeikin, S.V., Bass, J.D., 2000b. Single-crystal elasticity of pyrope and MgO to 20 GPa by Brillouin scattering in the diamond anvil cell. *Phys. Earth Planet. Inter.* **120**, 43-62.
- Sinogeikin, S.V., Bass, J.D., 2002. Elasticity of pyrope and majorite-pyrope solid solutions to high temperatures. *Earth Planet. Sci. Lett.* *203*: 549-555.
- Sinogeikin, S.V., Lakshtanov, D.L., Nicholas, J.D., Bass, J.D., 2004. Sound velocity measurements on laser-heated MgO and Al₂O₃. *Phys. Earth Planet. Interiors* **143-144**, 575-586.
- Sinogeikin, S.V., Zhang, J., Bass, J.D., 2004. Elasticity of single crystal and polycrystalline MgSiO₃ perovskite by Brillouin spectroscopy. *Geophys. Res. Lett.* *31*, L06620, doi:10.1029/2004GL019559.
- Sleep, N.H., 1973. Teleseismic P-wave transmission through slabs. *Bull. Seism. Soc. Am.* **63**, 1349-1373.
- Sondergeld, P., Schranz, W., Troster, A., Armbruster, T., Giester, G., Kityk, A., Carpenter, M.A., 2005. Ordering and elasticity associated with low-temperature phase transitions in lawsonite. *Am. Mineral.* **90**, 448-456.
- Speziale, S., Zha, C.S., Duffy, T.S., Hemley, R.J., Mao, H.K., 2001. Quasi-hydrostatic compression of magnesium oxide to 52 GPa: implications for the pressure-volume-temperature equation of state, *J. Geophys. Res.-Sol. Ea.* *106*(B1), 515-528.
- Stixrude, L., Hemley, R.J., Fei, Y., Mao, H.K., 1992. Thermoelasticity of silicate perovskite and magnesiowustite and stratification of the earth's mantle, *Science*, *257*, 1099-1101.
- Stixrude, L., 1997. Structure and sharpness of phase transitions and mantle discontinuities. *J. Geophys. Res., Solid Earth* *102*, 14835-14852.
- Stixrude, L., Lithgow-Bertelloni, C., 2005. Thermodynamics of mantle minerals: I. Physical properties. *Geophys. J. Int.* **162**, 610-632.
- Stixrude, L., Jeanloz, R., 2007. Constraints on seismic models from other disciplines - Constraints from mineral physics on seismological models, in *Treatise on Geophysics, Volume 1: Seismology and the Structure of the Earth*, G. Schubert, ed., 775-803, Oxford: Elsevier Ltd., doi: 10.1016/B978-044452748-6/00026-2.
- Stixrude, L., Lithgow-Bertelloni, C., Kiefer, B., Fumagalli, P., 2007. Phase stability and shear softening in CaSiO₃ perovskite at high pressure, *Physical Review B*, *75*, 024108-1-10, 10.1103/PhysRevB.75.024108.
- Su, W.J., Woodward, R.L., Dziewonski, A.M., 1994. Degree-12 Model of Shear Velocity Heterogeneity in the Mantle. *Journal of Geophysical Research*, **99**(4), 4945-4980.
- Tonks, W.B., Melosh, H.J., 1993. Magma ocean formation due to giant impact. *J. Geophys. Res.* *98*, 5319-5333.

- Trampert, J., Deschamps, F., Resovsky, J., Yuen, D., 2004. Probabilistic tomography maps chemical heterogeneities throughout the lower mantle. *Science* **306**, 853-856.
- Tsujimori, T., Sisson, V. B., Liou, J.G., Harlow, G. E., Sorenson, S. S., 2006. Very-low-temperature record in subduction process: A review of worldwide lawsonite eclogites. *Lithos.* **92**(3-4), 609-624.
- Ulmer, P., Trommsdorff, V. 1995. Serpentine stability to mantle depths and subduction-related magmatism. *Science* **268**, 858-861.
- Vanpeteghem, C.B., Zhao, J., Angel, R.J., Ross, N.L., Bolfan-Casanova, N. 2006a. Crystal structure and equation of state of MgSiO₃ perovskite. *Geophys. Res. Lett.* 33(3): doi: 10.1029/2005GL024955. issn: 0094-8276.
- Vanpeteghem, C.B., Angel, R.J., Ross, N.L., Jacobsen, S.D., Dobson, D.P., Litasov, K.D., Ohtani, E., 2006b. Al, Fe substitution in the MgSiO₃ perovskite structure: A single-crystal X-ray diffraction study, *Phys Earth Planet In*, 155, 96-103.
- Wang, Y., Gasparik, T., Liebermann, R.C., 1993. Modulated microstructure in synthetic majorite. *Am. Mineral.* 78, 1165-1173.
- Wang, Y., Rivers, M., Sutton, S., Nishiyama, N., Uchida, T., Sanehira, T., 2009. The large-volume high pressure facility at GSECARS: A “Swiss-army-knife” approach to synchrotron-based experimental studies. *Phys. Earth Planet. Inter.* 174, 1-4, 270-281.
- Watson, E.B., Lupulescu, A., 1993. Aqueous fluid connectivity and chemical transport in clinopyroxene-rich rocks. *Earth Planet, Sci. Lett.* **117**, 279-294.
- Weidner, D. J., Wang, Y., 1998. Chemical and Clapeyron induced buoyancy at the 660 km discontinuity. *J. Geophys. Res* 103, 7431-7441.
- Weidner, D. J., Wang, Y., 2000. Phase transformations: Implications for mantle structure, in *Earth’s Deep Interior: Mineral Physics and Tomography From the Atomic to the Global Scale*, *Geophys. Monogr. Ser.*, vol. 117, edited by S.-I. Karato, A. M. Forte, R. C. Liebermann, G. Masters, and L. Stixrude, pp. 215 – 235, AGU, Washington, D. C.
- White, R.S., McKenzie, D., O’Nions, R.K., 1992. Oceanic crustal thickness from seismic measurements and rare earth inversions. *J. Geophys. Res.* **97**, 19683-19915.
- Xu, W., Lithgow-Bertolini, C., Stixrude, L., Ritsema, J., 2008. The effect of bulk composition and temperature on mantle seismic structure. *Earth Planet Sci. Lett.* 275, 70–79.
- Zha, C.S., Mao, H.K., Hemley, R.J., 2000. Elasticity of MgO and a primary pressure scale to 55 GPa. *Proceedings of National Academy of Sciences of the United States of America*, Vol. 97, No. 25, p13494-13499.
- Zhang, J., Weidner, D.J., 1999. Thermal equation of state of aluminum-enriched silicate perovskite. *Science*, 284, 782–784.

Appendix 1

Elastic properties of minerals

Seismological investigations provide the only direct insight into the properties of the Earth's interior, especially for depths greater than a few hundreds of kilometers and have the ability to isolate its properties with high resolution, below one kilometer in the upper mantle and tens of kilometers in the lower mantle. For understanding the interior of our planet, it is required to convert this information into parameters such as mineralogical assemblage and chemical composition. However, values that describe the elastic properties of minerals at relevant conditions, of high pressure and high temperature, are required in this purpose. Elastic properties describe the instantaneous but temporary volume and shape changes that occur when stresses are applied to a material. Elastic properties are fundamental because they determine the velocities of the seismic waves and the change in density occurring when minerals are under high pressures. Different types of seismic waves are generated when earthquakes occur. The primary (P) compressional waves vibrate material parallel to the direction in which the wave propagates and the secondary (S) shear waves vibrate material perpendicular to the propagation direction. Shear waves have the properties of not propagating through fluids and travel slower than P waves.

The material properties of a medium determine how stress and strain are related. There is a linear relation to define an elastic constant tensor c_{ijkl} by:

$$\sigma_{ij} = \sum c_{ijkl} \varepsilon_{kl} \quad (1.1.1)$$

with σ the stress tensor and ε the strain tensor.

These symmetries of c are used to write stresses, strains and elastic constants in a compressed notation, with the stresses and strains labeled by:

$$1 = 11, 2 = 22, 3 = 33, 4 = 23, 5 = 31 \text{ and } 6 = 12$$

In this study, the focus is on polycrystalline samples with random orientations. As an isotropic system, the number of independent elastic constants reduces to two in Hooke's law:

$$\sigma_{ij} = \lambda \delta_{ij} \sum_k \varepsilon_{kk} + 2G \varepsilon_{ij} \quad (1.1.2)$$

where δ_{ij} is equal to 1 if $i=j$ and to zero if $i \neq j$, $\sum_k \varepsilon_{kk} = \Delta V / V$ is the trace of the strain tensor, and λ and G are the two independent *Lame constants*, defined by :

$$G = c_{44} \text{ (the shear modulus)} \quad (1.1.3)$$

and

$$\lambda = c_{12} = c_{11} - 2c_{44} \quad (1.1.4)$$

The change in volume, ΔV , results from the atoms getting closer with increasing pressure, hence compressibility. The pressure-volume relation describes the isothermal incompressibility, K_T , also called bulk modulus. K_T is obtained by measuring the volume or density of a sample at several known pressures:

$$K_T = -V(dP / dV)_T = \rho(dP / d\rho)_T \quad (1.1.5)$$

where K_T is in GPa, ρ is the density expressed in g.cm^{-3} and T is the temperature in K .

The bulk modulus is required to define the density and pressure distribution in the Earth because it gives the variation of density of minerals as a function of pressure. This elastic modulus is also directly related to the seismic velocities:

$$K_S = \rho(V_p^2 - \frac{4}{3}V_s^2) \quad (1.1.6)$$

where K_S is the adiabatic bulk modulus expressed in GPa and V_p and V_s are the seismic wave velocities in km.s^{-1} .

Another essential elastic modulus required for the interpretation of the seismic data is the shear modulus G . This property is a measure the rigidity of a material and fluids do not have any, explaining why the shear elastic wave cannot propagate in through them. Similarly to the bulk modulus, the shear modulus is related to the seismic velocities:

$$G = \rho V_s^2 \quad (1.1.7)$$

$$V_s = \sqrt{\frac{G}{\rho}} \quad (1.1.8)$$

$$V_p = \sqrt{\frac{K_s + \frac{4}{3}G}{\rho}} \quad (1.1.9)$$

Poisson's ratio ν is a dimensionless combination of elastic moduli and is used with this other moduli to completely define the elastic properties of a body:

$$\nu = \frac{\lambda}{2(\lambda + G)} \quad (1.1.10)$$

and

$$\nu = \frac{3(K/G) - 2}{2(3K/G + 1)} \quad (1.1.11)$$

Poisson's ratio is use in geophysics because it can be expressed as a function of V_p / V_s :

$$\nu = \frac{(V_p / V_s)^2 - 2}{2[(V_p / V_s)^2 - 1]} \quad (1.1.12)$$

The bulk modulus K of a single-phase aggregate of anisotropic crystals is the same as the bulk modulus of the individual crystals. But there are no exact solutions to calculate the effective shear moduli of an aggregate from single crystal elastic constants. The average value lies between two bounds. A lower bound is calculated assuming that the stress is uniform in the aggregate and that the strain is the total sum of all the strains of the individual grains in series (*Reuss* bound), and the upper bound calculated assuming that the strain is uniform and that the stress is supported by the individual grain in parallel (*Voigt* bound). The arithmetic average of the two bounds is often used (*Voigt-Reuss-Hill average*).

The difference between the bulk modulus at constant temperature (isothermal) and the bulk modulus at constant entropy (adiabatic) is not trivial since the elastic moduli measured in the laboratory by ultrasonic methods are adiabatic, as well as the one derived from the seismic velocities. But the elastic moduli relevant to geodynamic processes on the scale of millions of years are isothermal (Poirier, 1991).

$$K_T = \left(\frac{dP}{d\varepsilon}\right)_T \text{ (isothermal bulk modulus)} \quad (1.1.13)$$

$$K_T = \left(\frac{dP}{d\varepsilon}\right)_S \text{ (adiabatic bulk modulus)} \quad (1.1.14)$$

with S the entropy.

***P-V-T* equation of state calculations**

Variation of pressure at constant volume (V) is formulated with the isothermal compression component $P(V, T_0)$ along $T_0 = 300\text{K}$ and the thermal pressure term $\Delta P_{th}(V, T)$ as

$$P(V, T) = P(V, T_0) + P_{th}(V, T) \quad (2.5.1)$$

$P(V, T_0)$ is often determined from the third-order Birch-Murnaghan equation of state (e.g. Birch, 1952):

$$P(V, T_0) = 3K_{T_0}(1 + 2f)^{5/2} f \left[1 + \frac{3(K'_{T_0} - 4)f}{2} \right] \quad (2.5.2)$$

where

$$f = \frac{[(V/V_0)^{-2/3} - 1]}{2} \quad (2.5.3)$$

and K_{T_0} and K'_{T_0} are the isothermal bulk modulus at zero pressure and 300K and its pressure derivative, respectively. The thermal pressure $\Delta P_{th}(V, T)$ can be evaluated by the Mie-Grüneisen equation with the Debye model:

$$\Delta P_{th}(V, T) = \left(\frac{\gamma}{V}\right) \Delta E_{th} \quad (2.5.4)$$

$$\Delta E_{th} = E_{th}(V, T) - E_{th}(V, T_0) \quad (2.5.5)$$

$$E_{th} = 9nN_A k_B T \left(\frac{\theta}{T}\right)^{-3} \int_0^{\theta/T} \frac{\chi^3}{e^\chi - 1} d\chi \quad (2.5.6)$$

where γ and θ are the Grüneisen parameter and the Debye temperature, respectively, and the constants n , N_A , and k_B are the number of atoms in the formula unit ($n = 2$), the Avogadro's number ($6.022 \times 10^{23} \text{ mol}^{-1}$), and the Boltzmann's constant (1.381×10^{-23}

JK⁻¹), respectively.

The experimentally determined V_P and V_S lead to the adiabatic bulk modulus K_S and shear modulus G with the density (ρ) determined by X-ray diffraction measurements using the relation:

$$K_S = (V_P^2 - \frac{4}{3}V_S^2)\rho \quad (2.5.7)$$

$$G = V_S^2\rho \quad (2.5.8)$$

The K_S can be converted to an isothermal bulk modulus (K_T) using the thermodynamic relation:

$$K_S = (1 + \alpha\gamma T)K_T \quad (2.5.9)$$

where α is the thermal expansion coefficient. The thermal expansion coefficient with varying volume is expressed with γ and constant volume specific heat (C_v) as

$$\alpha = \frac{\gamma\rho C_v}{K_T} \quad (2.5.10)$$

The C_v value can be evaluated with the Debye's function:

$$C_v = 9nN_A k_B \left(\frac{\theta}{T}\right)^{-3} \int_0^{\theta/T} \frac{\chi^4 e^\chi}{(e^\chi - 1)^2} d\chi \quad (2.5.11)$$

Then equations (2.5.9) and (2.5.10) lead to the equation:

$$K_S = K_T + \gamma^2\rho C_v T \quad (2.5.12)$$

Here was adopted a unified formulation for K_T , G , and γ suggested by Stixrude and Lithgow-Bertelloni (2005). Stixrude and Lithgow-Bertelloni (2005) proposed a thermodynamically consistent formulation for pressure, K_T , G , and γ , which are formulated by the derivative of finite strain. The K_T and G are evaluated with the third-order finite strain equations as

$$K_T = K_{T0}(1 + 2f)^{5/2} \left[1 + (3K'_{T0} - 5)f + \frac{27}{2}(K'_{T0} - 4)f^2 \right] + (\gamma + 1 - q)\gamma\rho\Delta E_{th} - \gamma^2\rho\Delta(C_v T) \quad (2.5.13)$$

$$G = (1 + 2f)^{5/2} \left[G_0 + (3K_{T_0}G'_0 - 5G_0)f + (6K_{T_0}G'_0 - 24K_{T_0} - 14G_0 + \frac{9}{2}K_{T_0}K'_{T_0})f^2 \right] - \eta_s \rho \Delta E_{th}$$

(2.5.14)

where $\Delta(C_v T)$ is the change in C_v with varying temperature at constant volume:

$$\Delta(C_v T) = TC_v(V, T) - T_0 C_v(V, T_0) \quad (2.5.15)$$

η_s is the shear strain derivative of γ , and the volume dependence of the γ , q , and s are represented as

$$\gamma = \frac{1}{6} \frac{v_0^2}{v^2} (2f + 1) [a_{ii}^{(1)} + a_{iikk}^{(2)} f] \quad (2.5.16)$$

$$\gamma q = \frac{1}{9} \left[18\gamma^2 - 6\gamma - \frac{1}{2} \frac{v_0^2}{v^2} (2f + 1)^2 a_{iikk}^{(2)} \right] \quad (2.5.17)$$

$$\eta_s = -\gamma - \frac{1}{2} \frac{v_0^2}{v^2} (2f + 1)^2 a_s^{(2)} \quad (2.5.18)$$

$$a_{ii}^{(1)} = 6\gamma_0 \quad (2.5.19)$$

$$a_{iikk}^{(2)} = -12\gamma_0 + 36\gamma_0^2 - 18\gamma_0 q_0 \quad (2.5.20)$$

$$a_s^{(2)} = -2\gamma_0 - 2\eta_{s0} \quad (2.5.21)$$

where v is the frequency, which is assumed to follow a Taylor series expansion in the finite strain:

$$v^2 = v_0^2 \left[1 + a_{ii}^{(1)} f + \frac{1}{2} a_{iikk}^{(2)} f^2 \right] \quad (2.5.22)$$

Debye temperature θ is also represented as:

$$\theta = \theta_0 \left[1 + a_{ii}^{(1)} f + \frac{1}{2} a_{iikk}^{(2)} f^2 \right]^{1/2} \quad (2.5.23)$$

Then one can evaluate K_{T_0} , K'_{T_0} , G_0 , G'_0 , γ and η_s with equations (2.5.11) to (2.5.23) from the experimentally observed K_s , G and unit-cell volume data with varying q_0 .

The parameters involved in the fitting equations at $V/V_0 = 1$ are defined by experimentally well-established data. The Debye temperature at $V/V_0 = 1$ is fixed. γ_0 is calculated using the thermodynamic relation:

$$\gamma_0 = \frac{\alpha_0 K_{S0}}{\rho_0 C_{p0}} \quad (2.5.24)$$

The K_{T0} value is obtained from the equation (2.5.9). The parameters K'_{T0} , G_0 , G'_0 and η_{S0} are fitted to the experimentally observed K_S , G and unit-cell volume with varying q_0 using the equations (2.5.11) to (2.5.23).

Appendix 2

Data collection

Once the setup connected as shown on the **Figure 2.1**, the first step is to plug the amplifier power supply. From this point every contact with the metallic connectors should be avoided, and **do not forget to ground yourself!!!** Then MHz system could be switched on, RF signal and pulse generators, and the oscilloscope.

After few minutes warming up the oscilloscope will show a signal from the reflection of the connected cube. If it does not appear, a time scale (X-axis) of the oscilloscope needs to be changed in order to see the whole area and to find a signal. Time scale and time position, shown on the monitor, can be changed pushing the button “Time base” on “setup” panel of oscilloscope.

In order to proceed to sound velocity measurements, the anvil, buffer rod and sample should be mechanically bonded and some pressure is required. Usually around 1 GPa, the intensity of the anvil echo will decrease and new echoes will appear on the oscilloscope later after the anvil echo. Several echoes from the buffer rod and the sample are observed.

For the travel time measurements only the first echoes from the buffer rod and the sample are used. In order to perform data collection one should note the starting point (in

seconds) of both echoes. It can be done using the two cursors on the oscilloscope. Increase the time scale to 1ns/div and put one of the cursors (button “Marker” on “Setup” panel, choose the desired cursor from the right side) at the very beginning of the sinusoidal echoes.

To collect interferometry data, both signals should overlap. This is achieved by increasing the pulse width on the pulse generator: set $B = T + 700$ ns or more to make the signals overlapping for at least 100 ns. The width of the pulse should be estimated previously for each run since the length of the sample is never the same. Values of the width of the pulse are operating by “up” and “down” green arrows to increase and decrease; and “left” and “right” arrows to move the position of the cursors.

One needs then to run manually through the range of frequencies (10 to 50 MHz for the shear waves and 30 to 70 MHz for the compressional waves) on the RF signal generator to find the optimal range for measurement; that is, where the intensity of the signal is high enough. When checking this, one must pay attention to the sample’s echo since usually it is less intense than the echo from the buffer rod.

Before starting the data collection it is also good to check the number of averages required to get a clean sinusoidal signal. First magnify the scale to 1 ns/div and then use the button “Acquisition” on the “Setup” panel of the oscilloscope. More averages (max 512) increase the data collection time, but improve the quality of the data.

Data collection is operating by a program “Acquisition-6062A.exe” on the computer; developed by K. Klasinski (Bayerisches Geoinstitut). Once the program is open it is not possible to operate manually on any component of the system any more. For interferometry data gathering it does not matter which frequency you set up at the beginning, so press “OK” to set the frequency.

To start data collection, go to the tab “Settings” and one needs to input the following information (**Figure 2.1**):

- Output file name.
- Mark “Sine fit” (not the “Save waveform”).
- Range of frequencies: usually 10 to 50 MHz for the shear waves and 30 to 70 MHz for the compressional waves.
- The step of changing frequency: usually 0.2 MHz to get a good resolution.

WARNING: Do not use 0.1 MHz step because the system cannot manage with odd numbers as first digit.

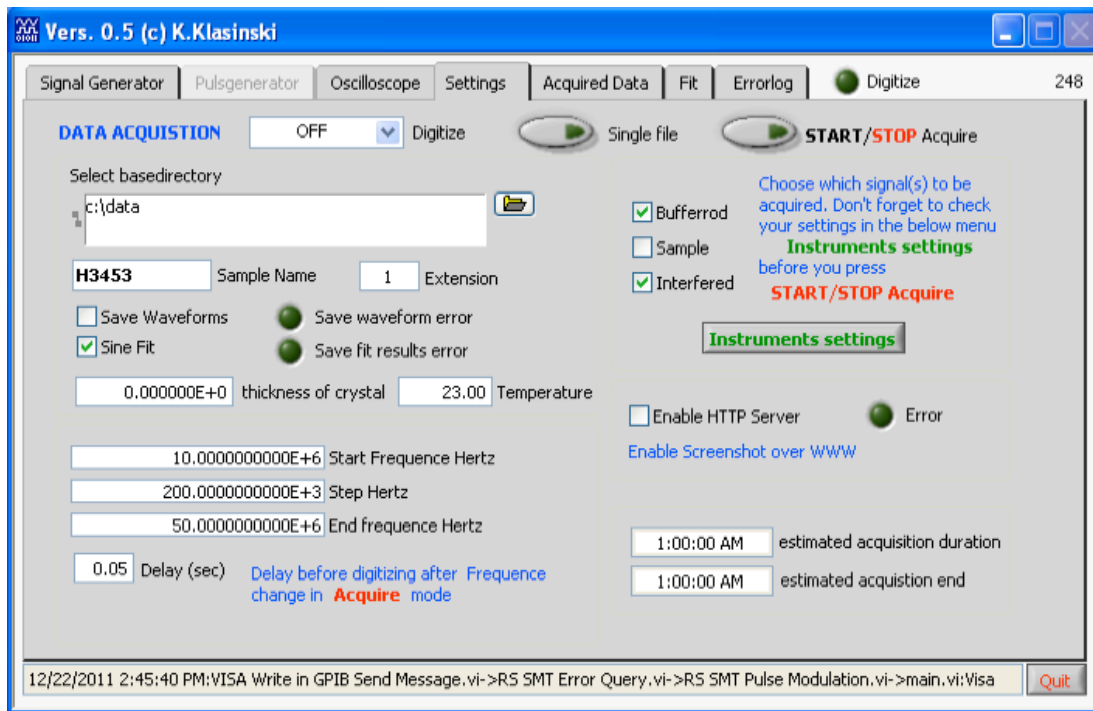


Figure 2.1

Enter the panel “Instrument settings” (**Figure 2.2** and **Figure 2.3**) and give the start point for the following measurements:

- “Bufferrod” echo, which should be measured after approximately 5-10 ns after the signal appears, because the pulse is never really square and the maximum of the intensity of the signal is reached only some time after it starts. The pulse width for this measurement (normally about 100 ns) and the oscilloscope resolution (10 ns/div), which is selected in order to see nice sinusoidal signal, and at least several period of it. The vertical scope resolution should be set at the maximum (1 mV/div) as far as the signal is not too intense and the whole sinusoid is on the screen.

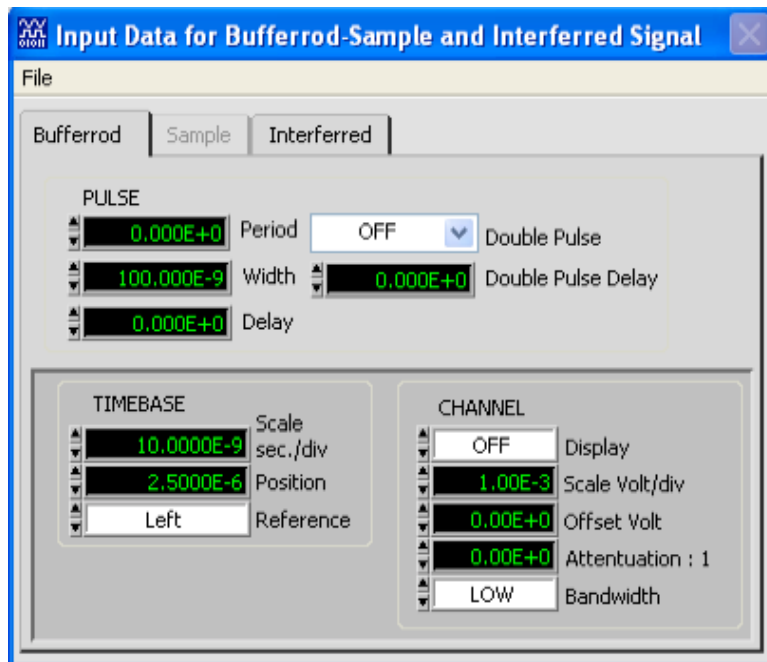


Figure 2.2

- “Interferred” data should be also collected after about 5-10 ns after the sample echo appears on the screen of the oscilloscope, at the same resolution (10 ns/div), but with a wider pulse (about 500 ns, depending on the travel time) where both signals are overlapping.

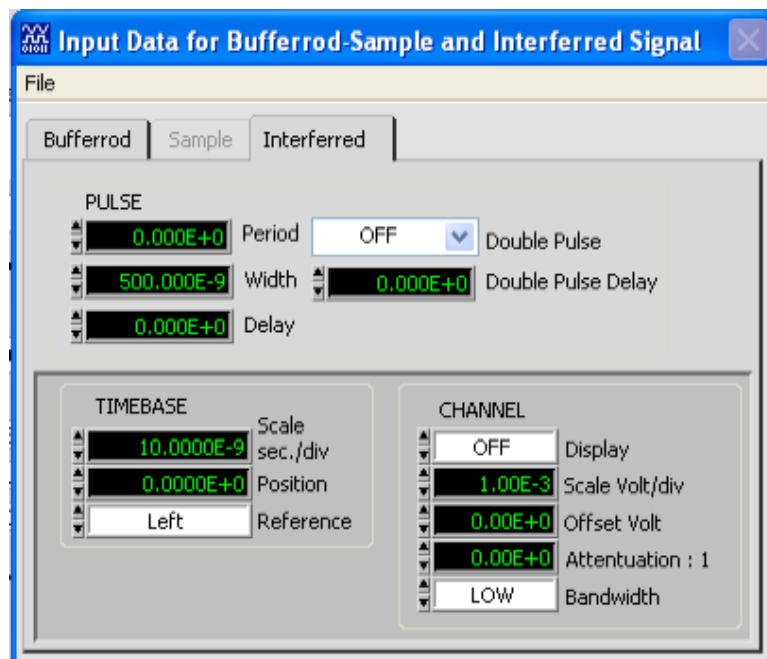


Figure 2.3

- To start the data acquisition, press the button “Single file” and finally “START/STOP Acquire” (**Figure 2.1**).

The buffer rod signal is collected in order to find the variation of actual acoustic intensity coming into the sample at different frequencies. Further the interference data will be demodulated using this buffer rod data, called envelop.

Data reduction

V_P and V_S velocities are related to the sample length (L) and the measured round-trip travel time (t) by: $V = 2L / t$. At ambient pressure, the length can be measured with a micrometer, because the samples are sufficiently thick (i.e. >0.5 mm).

The travel time is extracted from the initial data using the software “Analysis”, also developed by K. Klasinski (Bayerisches Geoinstitut). When the software starts, choose the main tab “Travel-time calculations” and then the secondary tab “Load Fitted Results” (**Figure 2.4**) and load the appropriate files from the file icons and load them by pressing the button “Load File(s)”.

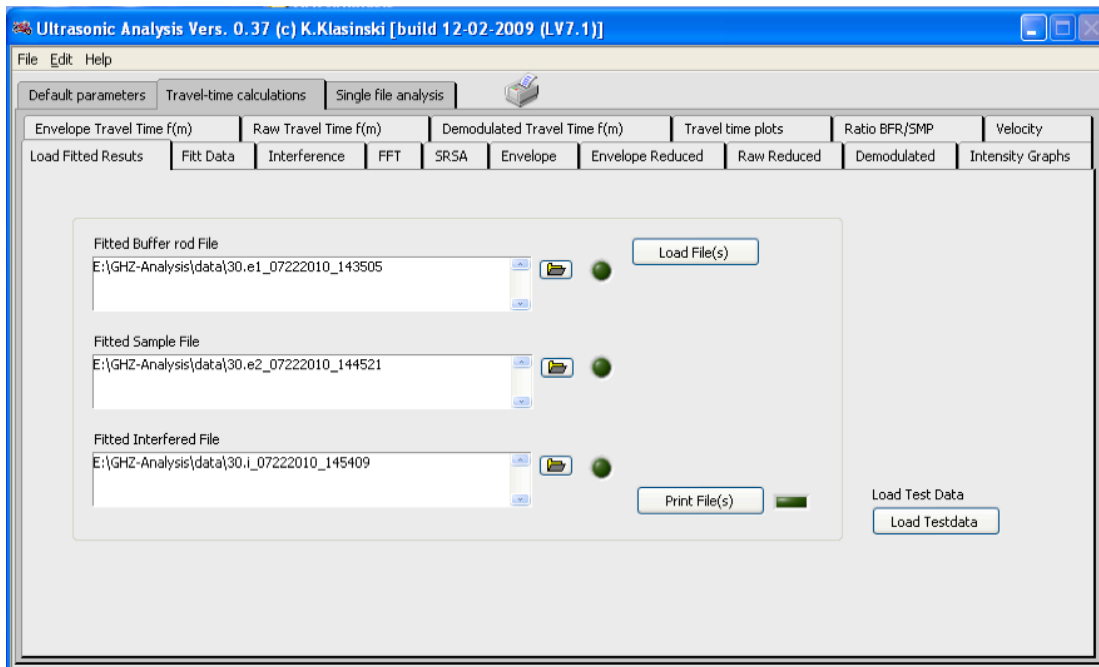


Figure 2.4

After loading files you will see interference pattern by choosing the tab “Interference” (Figure 2.5). One can then proceed:

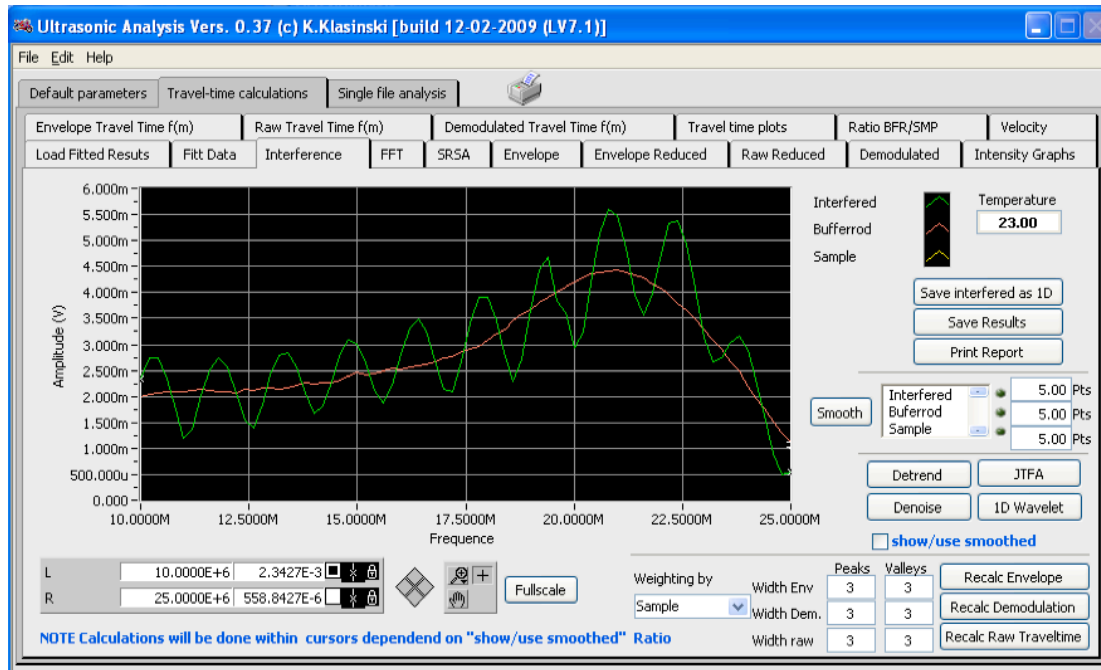


Figure 2.5

- Choose using vertical cursors the frequency range you want to use for further calculations
- Smooth the pattern if necessary: input number of points for smoothing, press button “Smooth” and check “Show/use smoothed”.
- Then press the button “Recalc Demodulation” and choose the tab “Demodulation Travel Time f(m)” to see the resulting travel time calculations (Figure 2.6). It appears in the small window called “mean-d” on the right; below it the “deviation-d” shown.

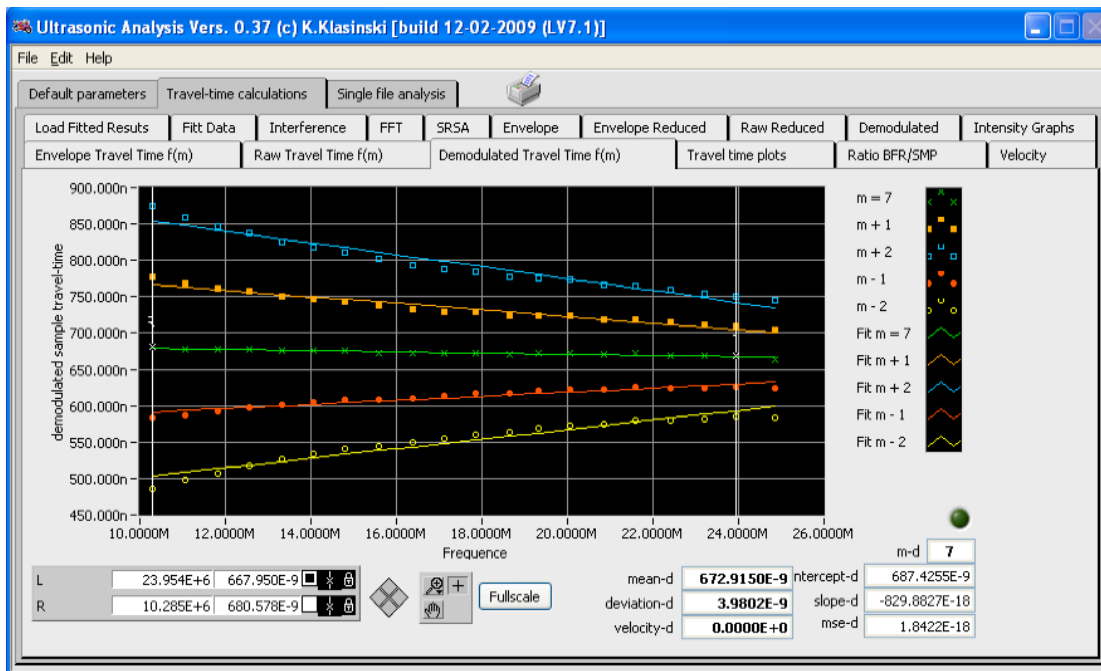


Figure 2.6

- Choose the tab “Velocity” and enter the sample thickness, and press the button “calculate” to obtain the final sound wave velocity (Figure 2.7).

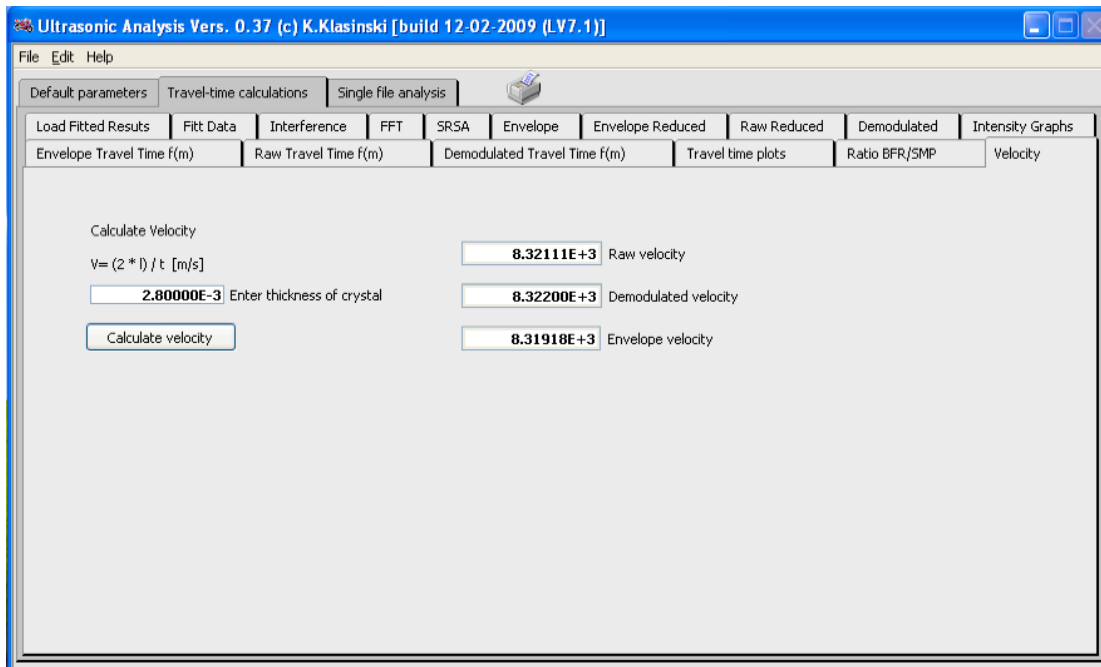


Figure 2.7

Appendix 3

Data collection

Follow those instructions to start data collection. On the signal generator:

- Select “waveform sequence” (bottom left) (red on the **Figure 3.1**).

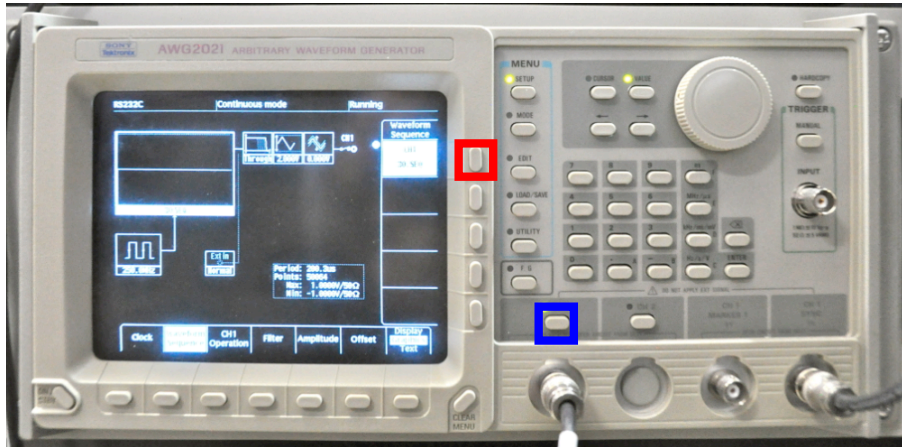


Figure 3.1

- Push the button “CH1” (right hand side of the control panel) (blue on the **Figure 3.1**).
- Select the waveform sequence by turning the wheel (blue arrow on the right hand side of the control panel **Figure 3.2**).

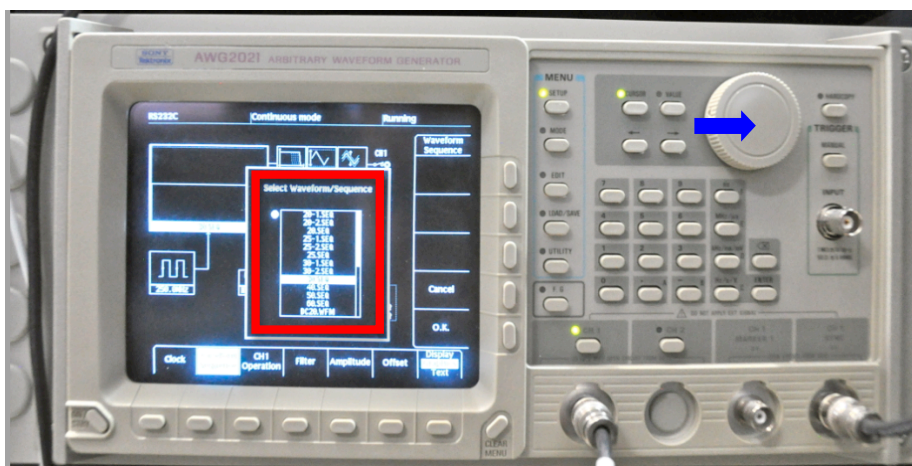


Figure 3.2

- Press “O.K.” (bottom right) (**Figure 3.2**).

Then on the oscilloscope:

- Refresh the display using “Run/Top” button on the top right of the command panel (red on the **Figure 3.3**).

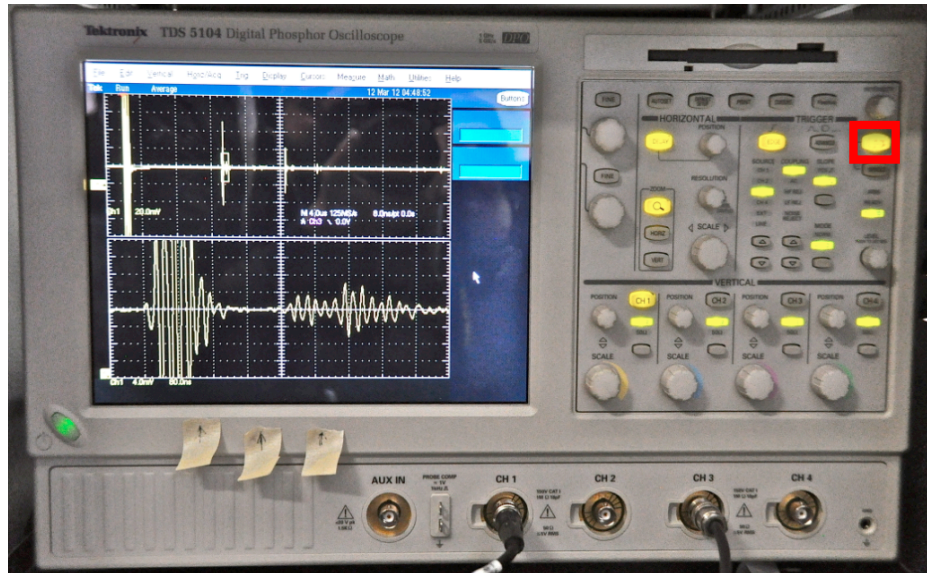


Figure 3.3

Save the file “File” – “Export...” (Figure 3.4).

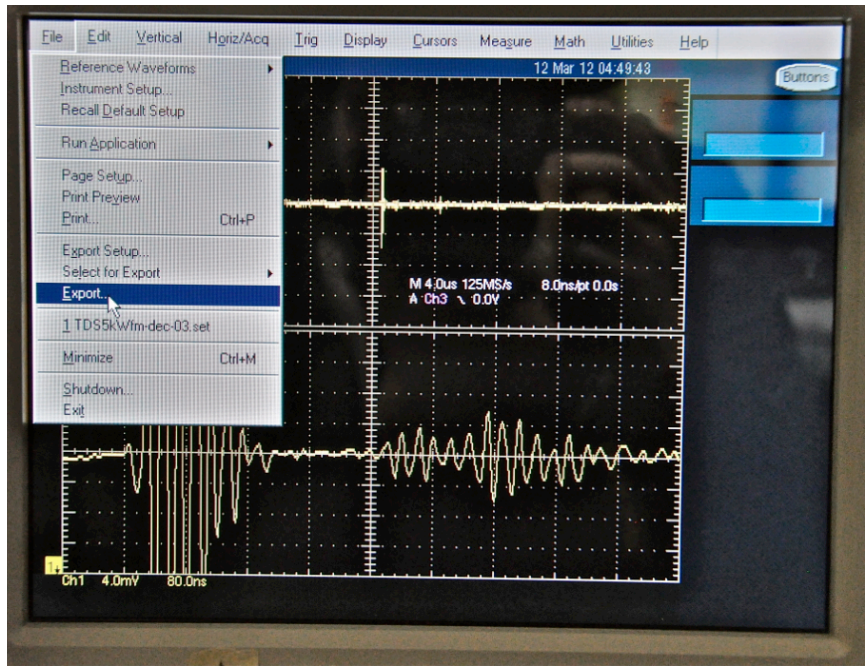


Figure 3.4

- In the “Export” window chose your directory file, the name of the file and the extension in “Save as type”, select “Waveform CSV files (*.csv)”, and select “Save” (**Figure 3.5**).

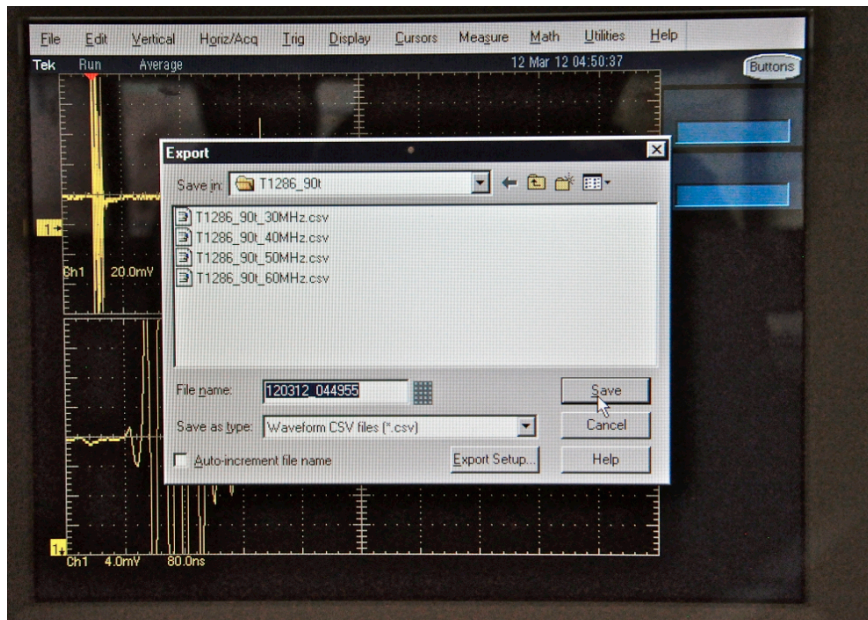


Figure 3.5

Data treatment

The travel time is directly obtained using *PEO-TDS-540* software developed by B. Li at SUNY, Stony Brook University, US (Li et al. 2002). Follow this procedure:

- Open *APS-TDS-540* software.
- Choose the data file to treat in the tab “File” and then “Open APS” (**Figure 3.6**).

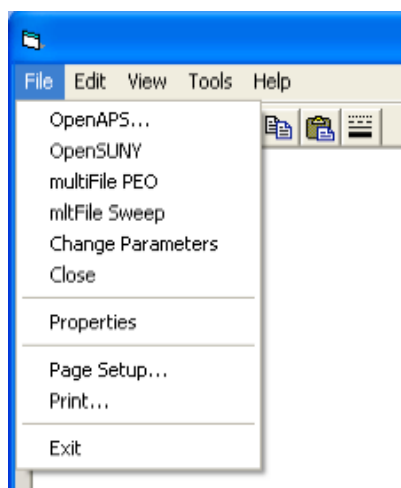


Figure 3.6

- To clean the signal and work on the compressional or shear wave echoes, one needs to define the right frequency (carrier frequencies are: 30 MHz for the S-wave and 50 MHz for the P-wave) and input it in the text box right below “Frequency”. Then define the number of cycle (usually between 2 and 5) and input it in the text box below “Cycles”. Finally press the button “Convolve” (**Figure 3.7**).

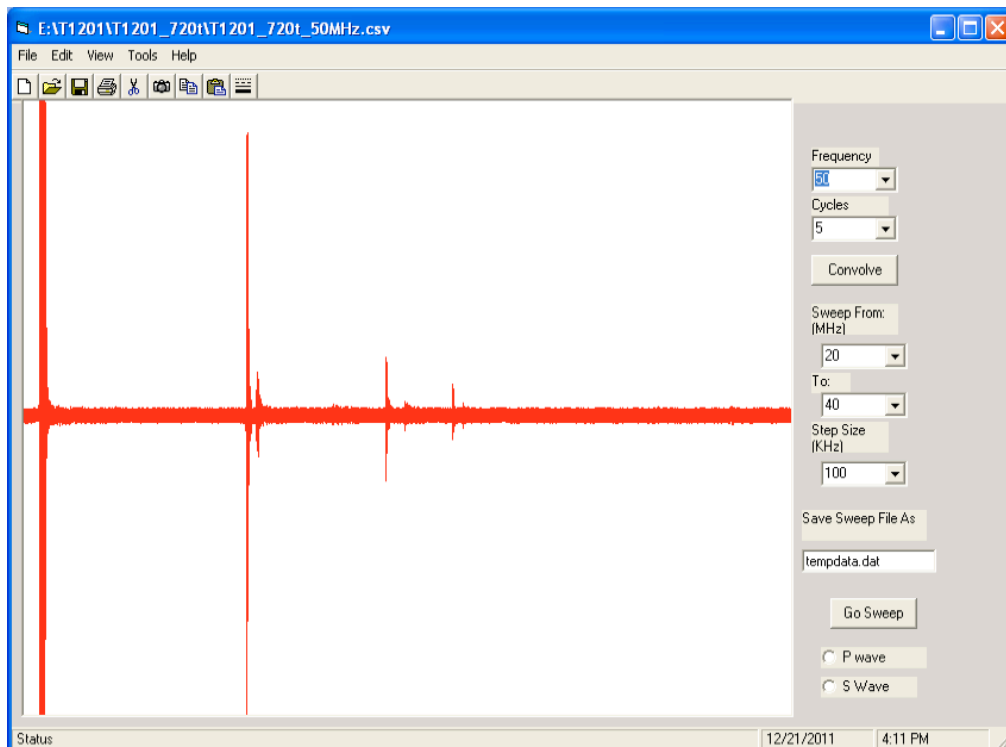


Figure 3.7

- Create a new file with a new name (for example: XXX_50MHz_5cycles).
- A new window is opening and the convolved signal is displayed. Press the right button of the mouse on the first echo of the buffer rod to place it in the center of the screen, you can then “Zoom in” and “Zoom out” (**Figure 3.8**).

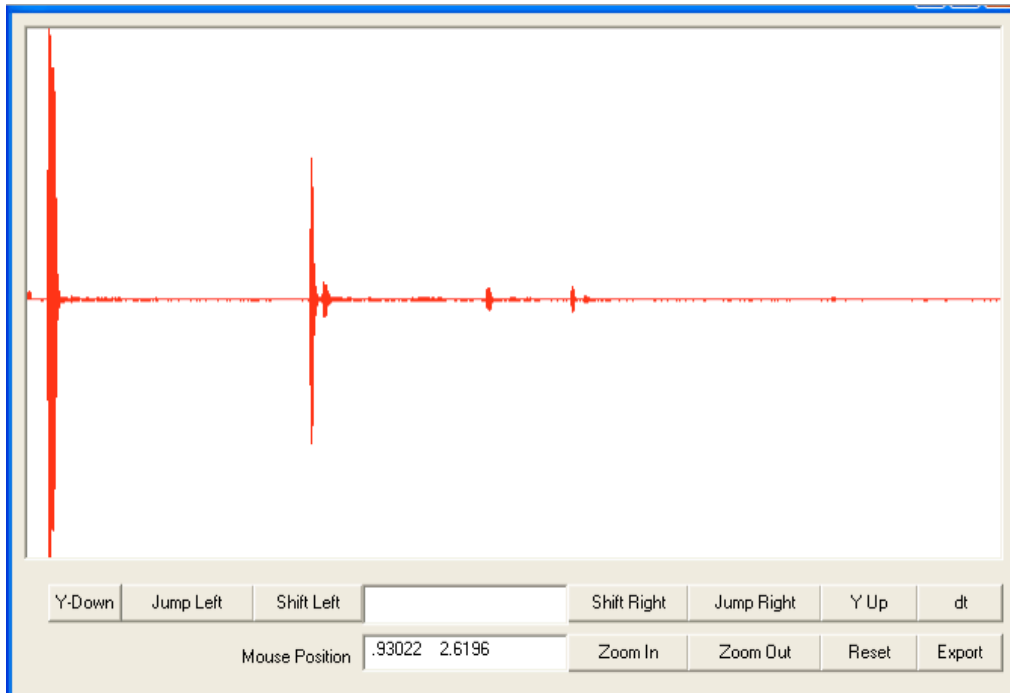


Figure 3.8

- Using “Jump left” and “Jump right” adjust the created copy to make the sample echo perfectly overlapping the buffer rod echo. “Shift left” and “Shift right” are useful for the fine adjustment (**Figure 3.9**).

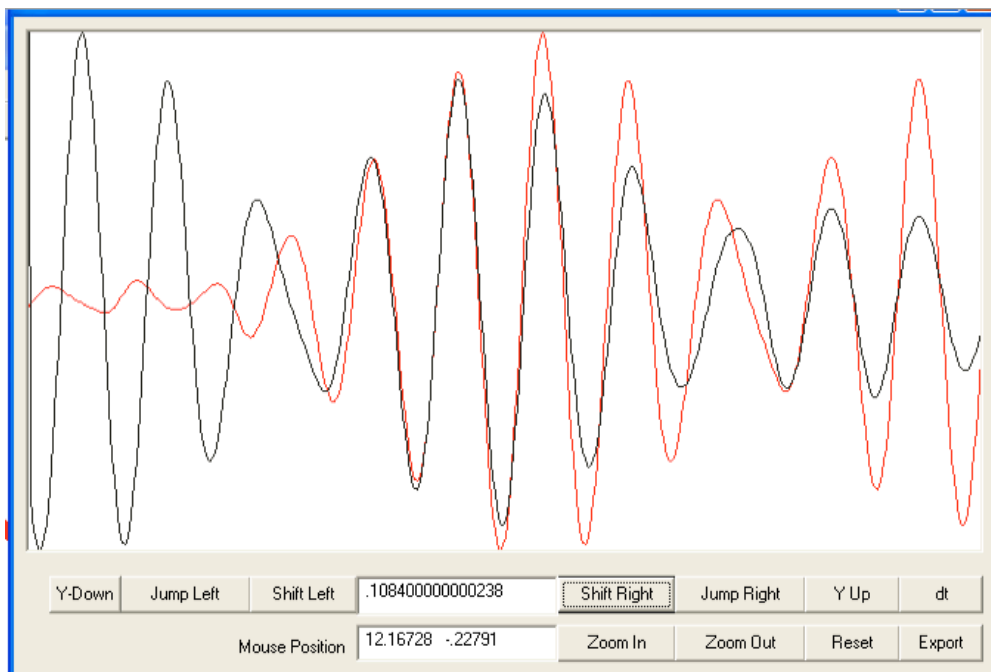


Figure 3.9

- Finally the two ways travel time is displayed, in μs , between the buttons “Shift left” and “Shift right” with a precision of 0.2 ns, resulting from the oscilloscope accuracy.
- The velocity is then calculated from this value (divided by 2, to get the travel time for one way) and the thickness of the sample.

ERKLÄRUNG

Hiermit erkläre ich, dass ich die vorliegende Arbeit selbständig verfasst und keine anderen als die von mir angegebenen Quellen und Hilfsmittel verwendet habe. Ferner erkläre ich, dass ich nicht anderweitig mit oder ohne Erfolg versucht habe, eine Dissertation einzureichen. Ich habe keine gleichartige Doktorprüfung an einer anderen Hochschule endgültig nicht bestanden.

Julien Chantel

Bayreuth, Oktober 2012.